Rita SZIJÁRTÓ

Condensation of steam in horizontal pipes: model development and validation

ETH - 22550

DISS. NO. ETH - 22550

Condensation of steam in horizontal pipes - model development and validation

A thesis submitted to attain the degree of
DOCTOR OF SCIENCES of ETH ZURICH

Presented by:

Rita SZIJÁRTÓ

Physicist (MSc),
Budapest University of Technology and Economics
Born on 21.10.1987
Citizen of Hungary

Accepted on the recommendation of:

Prof. Dr. Horst-Michael PRASSER
Prof. Dr. Stephan LEYER
Prof. Dr. Rafael MACIÁN-JUAN

2015

In science, it is not speed that is the most important.
It is the dedication, the commitment, the interest
and the will to know something and to understand it
– these are the things that come first.

WIGNER *Jenő*

Abstract

Condensation models were introduced and developed particularly for the application in the emergency cooling system of a Gen-III+ boiling water reactor. The emergency cooling system consists of slightly inclined horizontal pipes, which are immersed in a cold water tank. The pipes are connected to the reactor pressure vessel, and they are responsible for a fast depressurization of the reactor core in case of accident; furthermore, for the continuous cooling. During an accident scenario hot steam enters the pipes at the top of the reactor pressure vessel and condenses on the colder walls, then flows downwards, where the outlet of the pipe is connected to the vessel above the core level.

The condensation in horizontal pipes was investigated with both one-dimensional system codes (RELAP5) and three-dimensional computational fluid dynamics codes (ANSYS FLUENT). The performance of the RELAP5 code was not sufficient for transient condensation processes; therefore, a mechanistic model was developed and implemented. The model calculated the heat transfer coefficient in a cross section of the flow field considering local parameters in the pipe. The model assumed a stratified flow pattern in the pipe with a laminar liquid film on the upper part of the cross section and an axial turbulent flow at the bottom of the pipe.

The modified RELAP5 code was used to calculate the Invert Edward Pipe experiment, which consisted of a closed, slightly inclined horizontal pipe, resting in a cold water tank. The fast pressurization of the pipe results in a highly transient condensation process on the pipe walls. The simulation predicted well the pressure, void fraction and temperature data for different initial conditions and different locations in the condensation pipe during the transient condensation process. Furthermore, the COSMEA facility, a single tube experiment for flow morphology and heat transfer studies, was simulated with the modified RELAP5 code. The calculations reproduced the experimental temperature and condensation rate results for different initial pressure and mass flow rates.

Condensation phenomenon was analyzed using the volume of fluid multiphase method in

the computational fluid dynamics code. The volume of fluid method solves a unique set of continuity equations in the domain and models the two phases by tracking the interface between them. Four models were developed and implemented into the FLUENT solver for modeling phase change processes.

The first technique introduced a mass and energy transfer at the interface, if the temperature of the corresponding cell was different from the saturation value. The equations, through many iterations, achieved the correct boundary conditions at the interface. The second method relied on the surface renewal theory. The theory assumed that the eddies, forming on the liquid surface, are responsible for the transfer of the latent heat to the bulk liquid. Therefore, the condensation rate depends on the turbulent velocity and length scale. The third model solved the heat flux balance equation at the interface; hence, the resolution of the thermal boundary layer in the linear region was necessary. The fourth technique was derived from the phase field theory, which is a mathematical approach to calculate interface related problems.

The four models were tested on the LAOKOON facility, which analyzed direct contact condensation in a horizontal duct. The sensitivity study showed that the numerical iteration technique and the phase field model fitted the best for the experimental results. The COSMEA facility was simulated with the numerical iteration and the phase field models. The simulations captured the developing geometry of the gas-liquid interface in the horizontal pipe and the temperature distribution in the liquid film.

The computational fluid dynamics calculations were used to justify the assumptions of the heat transfer coefficient calculation implemented into the RELAP5 code. The laminar regime of the liquid film was verified at the upper part of the pipe cross section. The distribution of the heat transfer coefficient on the wall calculated with the volume of fluid multiphase method followed the smooth distribution demonstrated with the mechanistic model.

Zusammenfassung

In dieser Arbeit werden Kondensationsmodelle für die Anwendung in Notkondensatorsystemen von Gen-III+ Siedewasserreaktoren vorgestellt und entwickelt. Der Notkondensator ist ein passives Sicherheitssystem, das aus leicht gegen die Horizontale geneigten, in einem Kühlbecken liegenden U-Rohren besteht. In einer Notsituation strömt Dampf aus dem Reaktordruckbehälter in die Rohre, kondensiert an den kalten Wänden und fliesst in den Reaktor zurück. Dadurch wird der die Nachzerfallswärme aus dem Reaktor an das Kühlbecken abgeführt, ohne dass ein zusätzlicher Kühlmittelverlust auftritt.
Die Kondensation von Wasserdampf wurde mit dem eindimensionalen Thermohydraulikprogramm (RELAP5) und der Methode der dreidimensionalen numerischen Strömungsmechanik (ANSYS FLUENT) modelliert.
RELAP5 konnte den Kondensationsvorgang unter stark transienten Bedingungen eines als Testfall verwendeten Experiments nicht reproduzieren. Daher wurde ein verbessertes mechanistisches Modell entwickelt und in RELAP5 implementiert. Unter Berücksichtigung von lokalen Parametern berechnet dieses Modell einen Wärmeübergangskoeffizienten entsprechend der im jeweiligen Strömungsquerschnitt vorliegenden Kondensatverteilung. Hierzu wird eine stratifizierte Strömung angenommen, bei der ein laminarer Flüssigkeitsfilm im oberen Teil des Querschnitts und ein Kondensatgerinne am Boden des Rohres vorliegen. Die Nachrechnung des Testfalls dem modifizierten RELAP5 Code bestätigte eine wesentliche Verbesserung gegenüber dem ursprünglichen Modell. Dabei handelt es sich um das sogenannte Inverse Edward-Pipe-Experiment, bei dem ein evakuiertes, leicht geneigtes, von kaltem Wasser umgebenes Rohr plötzlich mit einem unter Druck stehenden Dampfkessel verbunden wird. An der Innenwand des Rohrs wird dabei ein hochgradig transienter Kondensationsvorgang ausgelöst. Die Simulation lieferte eine gute Übereinstimmung des Druckverlaufs sowie des Gasgehalts und der Temperatur an verschiedenen Positionen des Rohrs für unterschiedliche Startbedingungen. Als zweiter Testfall wurden Experimente an der Rossendorfer Anlage COSMEA hinzugezogen, bei der es sich um ein Einzelrohr mit

Kühlmantel handelt, das mit Thermoelementen und einem Röntgentomographen ausgestattet ist. Die Berechnungen mit dem modifizierten RELAP5 Code zeigen ebenfalls eine gute Übereinstimmung mit experimentellen Temperaturdaten und Kondensationsraten.
Im zweiten Teil der Arbeit wurde das Kondensationsphänomen dreidimensional behandelt. Die Dynamik der Phasengrenze wurde mit Hilfe der Volume-of-Fluid (VOF)-Methode simuliert. Sie beschreibt die zwei Phasen als Kontinuum, wobei der Volumenanteil die lokal gültigen Stoffwerte bestimmt. Durch Lösung der Transportgleichung für den Volumenanteils wird die Gestalt und Ausdehnung der Zwischenphasengrenzfläche ermittelt. Für den Phasenübergang wurden vier Modelle entwickelt und in den Solver des kommerziellen CFD-Codes von FLUENT integriert.
Das erste Modell beschreibt den Energie und den Massentransport an der Grenzfläche als Funktion von der Abweichung der Temperatur der betreffenden Zelle von der Sättigungstemperatur. Über einen Relaxationsansatz werden iterativ korrekte Randbedingungen an der Phasengrenzfläche erreicht. Das zweite Modell basiert auf der Surface Renewal Theory, die davon ausgeht, dass die turbulente Strömung der Flüssigphase für den Wärmetransport an die Phasengrenzfläche verantwortlich ist. Dadurch definiert die Theorie eine Kondensationsrate, die vom Massstab der turbulenten Strukturen abhängig ist. Das dritte Modell löst die Wärmeleitungsgleichung an der Grenzfläche. Hierzu muss die thermische Grenzschicht im linearen Bereich aufgelöst werden. Das vierte Modell leitet sich von der Phasenfeldmethode ab, einem thermodynamischen Ansatz für Phasenübergänge oberflächenbezogene an einer freien Oberfläche.
Die vier Modelle wurden anhand von Daten überprüft, die an der Versuchsanlage LAKOON gewonnen wurden. Dabei handelt es sich um Kondensationsexperimente an einer freien Oberfläche in einem horizontalen Kanal. Eine Sensitivitätsanalyse hat den Beweis erbracht, dass der iterative Relaxationsansatz und die Phasenfeldmethode die experimentellen Resultaten am besten wiedergeben. Kondensationsexperimente in einer Rohrleitung, der Rossendorfer COSMEA Anlage, wurden ebenfalls mit diesen beiden Methoden nachgerechnet. Es gelang die beobachteten Strömungsmuster im Rohr sowie die Temperaturverteilung im Fluid und an der Wand in den Grenzen der Genauigkeit der Messung zu reproduzieren. Die Ansätze zur Berechnung der Wärmeübergangskoeffizienten, die in RELAP5 implementiert wurden, konnten mittels dreidimensionaler Simulationen mit dem getesteten CFD-Modell bestätigt werden. Die Annahme eines laminaren Kondensatfilms im oberen Teil des Rohrquerschnitts wurde verifiziert. Die mit der VOF-Methode berechnete Verteilung des Wärmeübergangskoeffizienten über den Umfang der Rohrleitung ist in guter Übereinstimmung mit dem vereinfachten mechanistischen Modell.

Összefoglalás

A jelen doktori dolgozat témája kondenzációs modellek fejlesztése, elsősorban a harmadik generációs forralóvizes reaktor passzív üzemzavari hűtőrendszerének vizsgálatára. Az üzemzavari hűtőrendszer a vízszintessel kis szöget bezáró szárakkal rendelkező, U-alakú csövekből áll, melyek hideg vizes hőcserélő medencébe merülnek. A csövek a reaktortartályhoz csatlakoznak két ponton, így üzemzavar esetén a tartályban keletkezett vígőz a kondenzációs csövekbe áramlik. A gőz lecsapódik a hőcserélők falán, majd a keletkezett víz visszaáramlik a tartályba, így biztosítva folyamatosan a zónában keletkező remanens hő elvonását.

A folyamat modellezését két megközelítésben, egydimenziós rendszerkód segítségével, valamint háromdimenziós CFD kód segítségével végeztem el. A RELAP5 rendszerkód szolgált a kondenzációs hőátadás számolására vízszintes csövek esetén. A kód alkalmatlannak bizonyult tranziens kondenzációs folyamatok számítására, ezért mechanisztikus modellt fejlesztettem és ültettem be a RELAP5 programba. A modell kiszámítja a kondenzációs hőátadási tényezőt a cső egy keresztmetszetében, figyelembe véve a lokális áramlási paramétereket. A modell három áramlási zónát különböztet meg: az első a lamináris film a cső felső részén, ahol a gőz lecsapódik a cső falára, a második a cső alján áramló tengelyirányú turbulens víz, míg a cső közepén helyezkedik el a szintén tengelyirányban áramló vízgőz.

A módosított RELAP5 program tesztelése az Invert Edwards Pipe (INVEP) kísérleti berendezés számításával történt. Az INVEP berendezés egyik végén zárt, a vízszinteshez képest kis szögben elhelyezkedő hőátadó csőből állt, mely egy hideg vizes tartályba merült. A cső másik vége egy nagynyomású, vízgőzzel töltött tartályhoz csatlakozott. A kísérlet során erős tranziens jelleget mutató kondenzáció ment végbe. A módosított RELAP5 program helyesen számította a lokális nyomást, a hőmérsékletet és a térfogati gőztartalmat a tranziens lezajlása alatt, különböző kezdeti feltételek mellett. A kód, ezek mellett, szintén helyesen számította a mért hőmérsékleteket és a kondenzáció mértékét a COSMEA berendezésen. A

COSMEA berendezés egy vízszintes csőből áll, melyet hőátadás és áramlástani kísérletek elvégzésére terveztek kondenzációs folyamatok mérésére.
A kondenzáció modellezése, az egydimenziós technika mellett háromdimenziós CFD kóddal is történt. A volume-of-fluid (VOF) többfázisú áramlási technikát alkalmaztam az ANSYS FLUENT program keretében. A VOF módszer a két fázis közötti határfelület követésén alapul. A módszer a két fázis közös megmaradási egyenletrendszerével dolgozik, mely a gőztartalom megmaradási egyenletével egészül ki. Az adott cella anyagi paraméterei a gőztartalom helyi értékén alapulnak. A dolgozat keretében négy kondenzációs modellt fejlesztettem, melyek segítségével fázisátalakulás számítható a VOF többfázisú technikával.
Az első modell a numerikus iterációs technika, mely tömeg- és hőátadást számol a határfelületi cellákban, amennyiben az adott cella hőmérséklete nem egyenlő a víz adott nyomásnak megfelelő forráspontjával. A második technika alapja, hogy a kondenzáció során leadott hő elvezetésének sebességét a víz turbulenciája határozza meg, így a kondenzáció mértéke a víz turbulenciájától függ. A harmadik modell a hőfluxus kontinuitási egyenletre épül a két fázis közötti felületen. Az egyenlet a hőmérséklet gradiensétől függ, ezért a lineáris termikus határréteg nagy pontosságú numerikus modellezése szükséges a számítások során. A negyedik technika a fázismező technikán alapul, mely egy matematikai módszer felületekkel kapcsolatos problémák megoldására.
A négy modell tesztelése a LAOKOON kísérleti berendezés számításával történt. A LAOKOON berendezés felületi kondenzáció mérésére alkalmas, melyben víz és gőz rétegesen áramlik egy vízszintes vezetékben. A vizsgálat kimutatta, hogy a numerikus iterációs technika és a fázismező modell adta a legjobb közelítést a kísérleti eredményekkel való összehasonlítás után. A COSMEA berendezés számítása e két modellel történt, melyek sikeresen visszaadták a csőben kialakuló áramlási képet, valamint a hőátadási tényező- és a hőmérséklet-eloszlást a cső belső falán.
A CFD számítások alkalmasak arra, hogy a RELAP5 kódhoz hozzáadott mechanisztikus hőátadási tényező számításakor figyelembe vett feltételezéseket és szempontokat igazolják. A mechanisztikus modell által feltételezett áramlási kép, a cső felső részén található áramlás lamináris, valamint a tengelyirányú áramlás turbulens jellege bizonyított. A hőátadási tényező falfelületi eloszlása a mechanisztikus modell valamint a CFD számítás alapján szintén azonos jelleget mutat.

Contents

Acknowledgements

I thank my family, my mom, my sister and brother, my dad, and of course, my grandma for being there for me, for listening to me, and for their support during these years. I thank Yaroslav for being with me at the difficult and the successful moments, and for listening to my endless presentations. And I thank him for the great photo on the cover of this book.
I thank the whole LRS laboratory at PSI, for welcoming me and guiding me through the first year. I am thankful for the friends I found there, for the Stars Coffee Club, and for the discussions we had about scientific and non-scientific problems. I am especially thankful to Jordi Freixa, who was my supervisor at the beginning of my PhD studies. I appreciate the discussions about the RELAP5 code, his revision of my papers and my thesis. I further thank Carl Adamsson, Tae-Wan Kim and Konstantin Nikitin, I am happy I was working together with you. I thank Philippe Jacquemoud for his friendship and, of course, for the IT support. I am grateful to Riccardo Puragliesi, for both work related and unrelated discussions.
I thank the LTH laboratory, first of all the Modeling and Simulation Group, where I spent the second half of my studies. I thank Bojan Ničeno for his supervision. I thank Arnoldo Badillo for explaining the phase field theory, and for the discussions we had about phase change. I thank Yohei Sato for helping me with Fluent. I thank Davide Papini and Robert Zboray for being my friends and my colleagues.
I would like to thank the team of the Merlin cluster, especially Valeri Markushin, for the support and maintenance of the cluster I used for my calculations.
I thank my thesis advisor, Prof. Dr. Horst-Michael Prasser, for mentoring me through my PhD studies. I would like to thank the members of my committee, Prof. Dr. Stephan Leyer and Prof. Dr. Rafael Macián-Juan, for reviewing my thesis.
I would like to thank AREVA for the financial support of my PhD project.
The list can never be complete, and I cannot thank you enough for being there at the right time and right place.

Villigen, 27 / 02 / 2015 R. Sz.

List of Figures

List of Tables

List of Symbols

Roman Symbols

$\dot{m}$	Rate of phase transition per unit volume	kg/m^3s
$DISS$	Energy dissipation function	W/m^3
$\vec{n}$	Normal vector	
$\vec{s}$	Unit vector in the orthogonal direction of the tangential plane	
A	Cross section $[m^2]$, interfacial area density $[1/m]$	
a	Thermal diffusivity	m^2/s
c	Magnitude of the velocity	m/s
C_p	Specific heat	J/kgK
D	Diffusion coefficient	
D_h	Hydraulic diameter	m
E	Energy	J
g	Gravitational constant	$9.81 m/s^2$
h	Enthalpy	J/kg
h_{lv}	Latent heat	J/kg
k	Turbulence kinetic energy	J/kg
L_t	Turbulent length scale	m
M	Mobility coefficient (phase field theory)	
N	Normalization factor	
P	Pressure	Pa
p	Periphery	m

Q	Volumetric heat transfer rate	W/m^3
q''	Heat flux	W/m^2
R	Radius	m
r	Radial variable [m], relaxation factor [$1/s$]	
S	Source term	
T	Temperature	K
t	Time variable	s
U	Specific internal energy	J/kg
u, v, w	Velocity components	m/s
u^*	Friction velocity	m/s
V	Volume	m^3
V_t	Turbulent velocity scale	m/s
W	Mass flow rate	kg/m^3
w	Characteristic interface thickness	m
X	Static vapor quality	
x, y, z	Distance variables	m
X_m	Mass quality	
X_n	Non-condensable mass quality	
Gr	Grashof number	
Nu	Nusselt number	
Pr	Prandtl number [Pr= $\mu C_p/\lambda$]	
Pr_t	Turbulent Prandtl number [$\mathrm{Pr}_t = \epsilon_m/\epsilon_h$]	
Ra	Rayleigh number [Ra = Gr·Sc]	
Re	Reynolds number [Re= WD_h/μ]	
Re_t	Turbulent Reynolds number [$\mathrm{Re}_t = \rho k/\mu\omega$]	
Sc	Schmidt number	
Sh	Sherwood number	

Greek Symbols

α	Heat transfer coefficient	W/m^2K
β	Temperature coefficient	$1/K$
δ	Film thickness	m
ϵ	Void fraction, Turbulent dissipation rate $[J/kgs]$	
ϵ_h	Heat eddy diffusivity	m^2/s
ϵ_m	Momentum eddy diffusivity	m^2/s
Γ	Mass flow rate per unit area	kg/m^2s
$\hat{\mu}$	Transformation potential (phase field theory)	
κ	Von Karman's constant	
λ	Thermal conductivity	W/mK
μ	Dynamic viscosity	kg/ms
Ω	System volume	m^3
ω	Specific dissipation rate	1/s
ϕ	Angular coordinate	
Φ_{strat}	Stratification angle	rad
ϕ_{vv}	Lockhart-Martinelli parameter for vapor	
ρ	Density	kg/m^3
σ	Surface tension	N/m
τ	Shear stress $[N/m^2]$, relaxation time (phase field theory)	
θ	Pipe inclination angle	rad
υ	Kinematic viscosity	m^2/s
φ	Additional scalar field (smearing function)	

Superscripts

$+$	Non-dimensional parameter
$bottom$	Bottom part of the pipe cross section
up	Upper part of the pipe cross section
B	Bulk

W	Wall

Subscripts

2Φ	Two-phase
δ	Film surface
in	Inside of the wall/primary side
mom	Momentum
out	Outside of the wall/secondary side
b	Boiling, bottom
c	Condensation
f	Liquid film
g	Gas phase
h	Heat
i	Interface
l	Liquid phase
m	Mass, Mixture
p	Partial pressure
s	Saturation
t	Turbulent
v	Vapor phase
w	Wall
TPF	Two-phase friction

Introduction

Condensation is an important phenomenon in many engineering applications. Phase change processes are efficient ways of heat removal, as the latent heat of condensation and boiling provides high heat transfer coefficients. The calculation of the heat transfer in phase change processes is crucial for designing heat exchangers.

The currently constructed and designed nuclear power plants satisfy higher safety standards due to the intense use of passive safety systems. Passive safety systems operate without external power supply or operator intervention, only relying on physical phenomena, such as natural circulation and gravity driven flows. New heat exchanger designs are applied for emergency core cooling and heat removal from the containment. While classical heat exchangers are optimized for high plant efficiency, the passive components like emergency condensers and containment cooling condensers have to be optimized for a wider range of operation parameters during the progression of an accident.

In the nuclear industry one-dimensional system codes are prevailing to simulate entire nuclear power plants and to analyze the reliability of the safety systems. However, three-dimensional techniques, such as computational fluid dynamics, gain more attention particularly for studies of complex multiphase phenomena. The two approaches are not interchangeable, the use and the development of both simultaneously helps to improve the simulation possibilities for power plants and big components.

Widely used representatives of one-dimensional simulation tools are the codes RELAP5 and TRACE, developed by the U.S.NRC. These codes are able to capture most of the phenomena occurring in the power plant; however, it is part of the safety philosophy to permanently question and improve the performance of these tools.

The computational fluid dynamics codes provide an efficient and powerful way to simulate single components in the power plant. These codes solve the continuity equations of the fluid in a three-dimensional domain using finite volume methods. The consideration of the three dimensions helps to better understand the flow behavior and heat transfer processes. However, modeling of two phase flows, in particular with phase change, is leading to computationally intense calculations. Therefore, the simulation of phase change heat

transfer remains a challenge in computational fluid dynamics.

In this thesis condensation models are introduced and evaluated and the application of these models to the emergency cooling system is discussed [1]. The emergency condenser of the KERENA reactor, serving as a passive device for depressurization and decay heat removal, is equipped with a bundle of horizontally oriented or slightly inclined tubes, which are immersed in a cold water tank. The pipes are connected to the reactor pressure vessel. During an accident scenario hot steam enters the pipes at the top of the reactor pressure vessel and condenses on the colder walls, then flows downwards, where the outlet of the pipe is connected to the vessel above the core level.

The condensation in horizontal pipes was investigated with both one-dimensional system codes (RELAP5 and TRACE) and three-dimensional computational fluid dynamics codes (ANSYS FLUENT). The performance of the RELAP5 code was not sufficient to reproduce the experimental data for fast transient condensation processes; therefore, a mechanistic model was developed to calculate the heat transfer coefficient in a cross section of the flow field, considering local parameters in the pipe. The model was implemented into the RELAP5 and the modified code was validated against two experimental facilities.

Computational fluid dynamics calculations were done on condensation, using the volume of fluid multiphase method in the FLUENT code. The volume of fluid method solves a set of continuity equations and simulates the two phases by tracking the interface between them. The method is highly efficient for multiphase flows with well defined interfaces; however, the FLUENT code does not have a phase change model implemented for the volume of fluid multiphase method. Therefore, four models were developed and implemented into the FLUENT solver for simulating phase change processes. A sensitivity study of the parameters and the validation of the models were done by simulating an experiment on direct contact condensation. Furthermore, the computational fluid dynamics calculations were used to justify the assumptions of the heat transfer coefficient correlation, which was implemented into the RELAP5 code.

It was demonstrated that both the one-dimensional and three-dimensional approaches are suitable to simulate the condensation in horizontal pipes. If the flow field is in a one-dimensional duct, the system code approach is preferable due to the high demand of computational resources of the three-dimensional calculation. However, to estimate the heat transfer coefficient, the cross sectional flow pattern, which is an information of an other dimension, is important even in one-dimensional calculations. The three-dimensional CFD calculations provide insights to the details of the velocity and temperature distribution, whenever the flow field is two or three-dimensional. The applied models contain less empirical parameters, they are more robust; moreover, they do not depend on the initial geometry as these models calculate the condensation rate on the cell level. The developed models for the FLUENT code are suitable not only for condensation, but for boiling phenomenon as well, and they do not depend on the calculated geometry. Whenever the flow is three-dimensional, the computational fluid dynamics code, with

the implemented phase change models, provide a tool for a better understanding of the processes.

The thesis is organized in six chapters. Chapter 1 introduces the KERENA reactor concept and the emergency condenser system, which motivated the project. The introduction to the RELAP5 code, the FLUENT code and a literature review for both methods is provided. The first chapter ends with a review of the simulated experimental facilities. Chapter 2 shows the model development for the heat transfer coefficient correlation for condensation in horizontal pipes. The models for the computational dynamics codes are described in Chapter 3. The theory of the models and the implementation details are presented. Chapter 4 contains the results for the RELAP5 calculations; whereas, Chapter 5 presents the results for the FLUENT calculations. All chapters have a conclusion section, which helps the understanding of the achievements of the given chapter. Finally, an overview and conclusion of the entire work is provided in the last chapter of the thesis.

1 Literature review

The current PhD project aimed at analyzing condensation in horizontal pipes. Two simulation approaches were applied: one-dimensional system codes and computational fluid dynamics. This chapter summarizes the literature review, which preceded the development and implementation of condensation models for both techniques.

Section 1.1 highlights the motivation for the PhD project, providing details about the emergency core cooling system of the KERENA reactor. Section 1.2 gives insights to the thermal-hydraulic modeling with one-dimensional system codes. The RELAP5 code, which was chosen to calculate the heat transfer in horizontal pipe condensation, is introduced, focusing on the heat transfer calculation. The heat transfer calculation of the TRACE code, which was, too, applied for condensation calculation, is summarized. The literature review of the next section provides details about the state-of-the-art for condensation modeling in one-dimensional codes.

The RELAP5 code was chosen as a main tool of this thesis because it is used by the developer of the KERENA reactor AREVA. The company possesses an own version of RELAP which was upgraded by boiling water reactor models (sRELAP). Furthermore, the analyses were extended to TRACE, because it is a widespread successor of RELAP. In Switzerland, input decks of all operated nuclear power plants are available for TRACE.

Section 1.3 follows a similar outline to Section 1.2, introducing the FLUENT flow equations, the volume of fluid multiphase method and summarizing the literature on phase change modeling with computational fluid dynamics. Section 1.4 describes the three experimental facilities, which were used for code validation.

1.1 The KERENA reactor concept and the emergency core cooling system

The key features of nuclear reactor development classify the nuclear reactors in four generations (Fig. 1.1) [2]. Each generation represents a technical improvement compared to the previously constructed power plants.

The first generation of reactors were developed between 1950-1970, and they were the prototype and power reactors which introduced the nuclear energy to public use and power generation. The first reactor, which produced electricity for the public energy supply, was built in Obninsk, Russia (AM-1, *Atom Mimy* or *peaceful atom*). The reactor was connected to the grid on 27 June, 1954, and it operated for 48 years. The first commercial power plant in the USA started to operate in 1957 in Shippingport, and it was a pressurized water reactor. The developers experimented with several cooling and moderator materials, such as gas cooled (Magnox, UK), with an intent on using natural uranium fuel. These reactors operated for 20-40 years, the last operating first generation reactor, the Wylfa Magnox reactor in Great-Britain, will retire in December 2015.

The economical and safe concepts from the Gen-I reactor family were developed further, and the improved reactor designs were grouped as Gen-II reactors. The majority of these plants started to operate between 1970-1990 with light water moderator and enriched uranium fuel. These reactors allowed the serial construction and the development of the today's fleet of nuclear power plants. Owing to the intense lifetime-extension projects (see *e.g.* [3]), most of the Gen-II reactors are still on the grid today, and will be shut down between 2015-2030.

Generation-III/III+ reactors are advanced water cooled reactors, resulted from the evolution of the Gen-II concepts. They feature standardized design, advanced fuel technology, longer lifetime and higher availability. An increased safety standard is achieved by passive safety systems and by the implementation of measures and systems to limit the consequences of a severe accident to the plant site. The Gen-III/III+ reactors are the currently built and available commercial power plants.

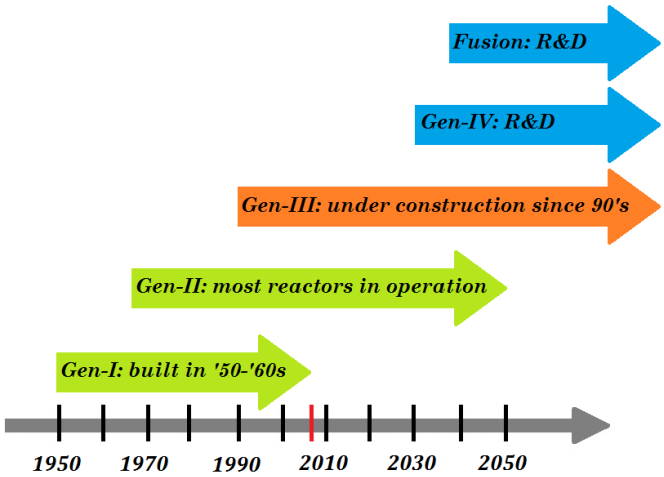

Figure 1.1: Evolution of reactor generations

The Gen-IV reactors are the future nuclear power plants, which have fundamentally different design [4]. The concepts aim at sustainable energy generation, enhanced safety, improved economics and some of them feature closed fuel circle. Six reactor designs are currently under research and development, leading by the Generation IV International Forum (GIF) [5].

Another direction of research and development, the commercial fusion reactors will not operate until 2050. The ITER design, currently under construction in Cadarache, France, intents on demonstrating the feasibility of fusion technology for peaceful purposes [6].

The KERENA (SWR-1000) boiling water reactor, developed by AREVA, is a Gen-III+ nuclear reactor design [1]. The KERENA reactor acquires the advantages of a Gen-III+ reactor concept, as it is economically efficient due to the simple operational and configuration design and the passive safety control. The power generation of the power plant is 1250 MWe and has a lifetime of 60 years. The main feature of the reactor concept is the extensive use of passive safety systems, which reduces the costs and increases the safety level of the plant.

KERENA features a combination of three redundant active safety systems with one passive system, which consists of four independent redundant strands (Fig. 1.2). Three of them are sufficient to bring the reactor in a safe state after an accident, as well as each strand of the active safety system. This approach is unique among all GEN-III concepts on the market today.

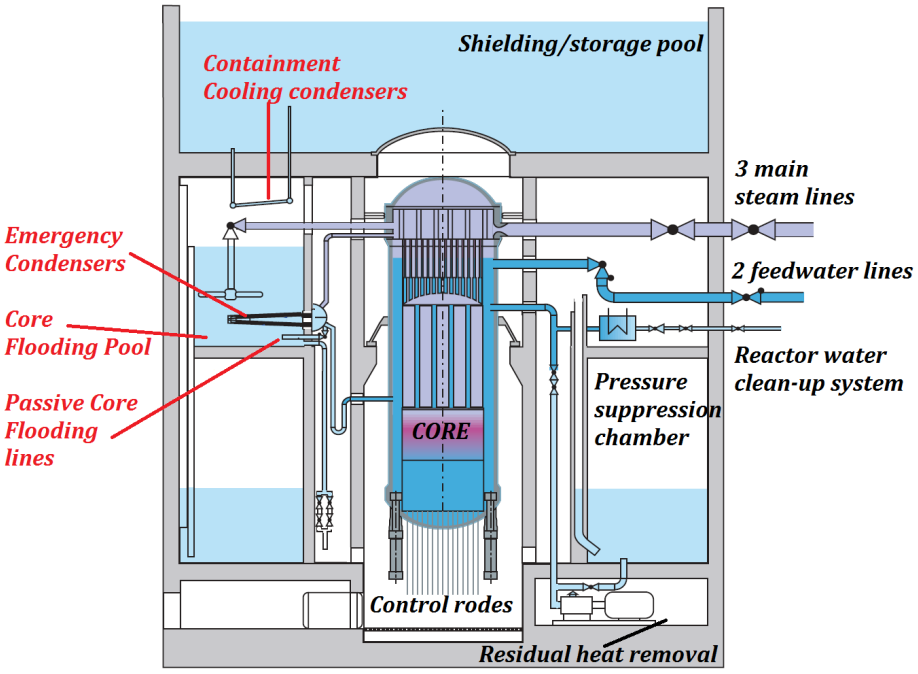

Figure 1.2: The KERENA containment with the passive safety systems [1]

Passive safety systems are driven by basic laws of physics; thus, they operate without external electric power and active control system. They are designed such that the power plant is brought to a stable state during accident automatically. The KERENA has independent passive safety systems:

- emergency condensers: depressurization and passive heat removal from the reactor pressure vessel if the water level drops;

- containment cooling condensers: passive heat removal from the containment by condensation on the external surface of inclined horizontal pipes. The heat is transferred to the storage pool, which serves as shielding a repository for activated reactor internals during refueling and maintenance and it is located above the primary containment;
- core flooding pool: the pool is connected to the reactor pressure vessel by flooding lines, which have self-actuating check valves. After the depressurization of the reactor pressure vessel, the cooling water from the flooding pool flows into the reactor driven by gravity. The pool also acts as a heat sink for the emergency condensers; furthermore, the condensed water from the containment cooling condensers flows into the pool;
- passive pressure pulse transmitters: the pressure level drop in the reactor pressure vessel causes an increased pressure on the secondary side of the passive pressure pulse transmitters, initiating safety related switching operations (reactor scram, automatic depressurization, containment isolation).

The emergency condensers are responsible for the depressurization and cooling of the reactor pressure vessel in an accident scenario (Fig. 1.3). The condensers are activated by a water level drop in the reactor pressure vessel. The condenser system consists of a U-tube pipe system, which are in slightly inclined horizontal orientation. The tubes are connected to the pressure vessel at two locations, and they operate on the principle of communicating vessels. The water level drop in the reactor pressure vessel causes a water level drop in the emergency condensers, and steam enters the horizontal U-tubes. The pipes are immersed in a core flooding pool; hence, the steam condenses on the colder pipe walls, as heat is transferred to the flooding pool. The condensate flows back to the reactor pressure vessel due to the inclined position of the condensers.

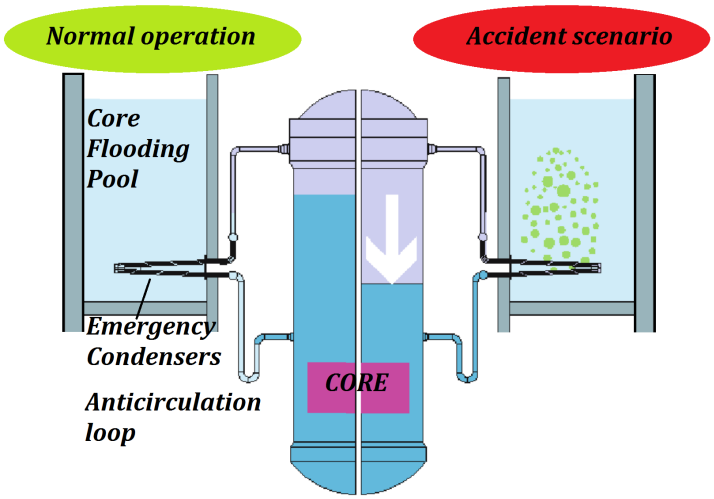

Figure 1.3: The operation scenarios of the emergency core cooling system of the KERENA reactor

The Integral Test Facility Karlstein (INKA) was built to test the passive safety systems of the KERENA reactor. The emergency condenser, the containment cooling condenser, the

passive core flooding and the passive pressure pulse transmitter systems were built in full high and level scale, the volume scaling was 1:24 to the KERENA containment [7]. Full-scale single component tests were done on the facility, and the pre-test calculations were done with the RELAP5 system code in the Paul Scherrer Institute [8],[9]. The comparison of the post-test calculations and experimental results showed that RELAP5 correctly captured the important phenomena in the emergency condensers; furthermore, it could reproduce the heat transfer from the emergency core cooling system to the containment pool [8]. Further proposals were made for test specification, based on integral pre-test calculations of the INKA Experiments [9].

The current PhD project continues the efforts on simulating the emergency condenser of the KERENA reactor concept in the project together with AREVA and HZDR research center. The analysis goes into the details of condensation modeling with both one-dimensional system codes and three-dimensional computational fluid dynamics. The following sections introduce the codes used in this thesis, and the experimental facilities which provided measurement results to validate the developed condensation models.

1.2 Thermal-hydraulic modeling with one-dimensional system codes

One-dimensional thermal-hydraulic system codes are used in nuclear industry to calculate the efficiency of the reactor cooling system during normal operation and transient scenarios. These codes can simulate the parts of a nuclear reactor, *e.g.* the pipe system, downcomer, pressurizer, turbines. The tools were developed mainly for water-cooled reactors and they can calculate the state of the two-phase mixtures of water and steam in all relevant phenomena for nuclear reactor safety. The state of the art of the one-dimensional thermal-hydraulic system codes is the two-fluid, six-equation model. The mass, momentum and energy equations are coupled and solved with a set of constitutive laws describing the interaction of the phases with each other and with the walls. The velocities of the fluids are directed according to the orientation of the calculation cell, which information is given by the user in the input deck. This is different from CFD codes, where the direction of the local velocity vector is a result of the momentum equation.

The development of system codes runs parallel in different countries. The RELAP5 [10] and TRACE [11] codes are developed by the U.S.NRC, the CATHARE code is developed in France [12], the ATHLET in Germany [13], and the APROS in Finnland [14]. In this thesis, the RELAP5 code was used as a main tool, and the results were compared to TRACE calculations as well. Accordingly, this section introduces the RELAP5 code, focusing on the general description of the flow field calculation and the heat transfer phenomena between the liquid and vapor phases [10]. The phase change models of both RELAP5 and TRACE are introduced. Section 1.2.3 provides the literature review on modeling condensation with one-dimensional codes.

1.2.1 The RELAP5/mod3.3 code

The first version of the RELAP codes was published in 1966, under the name RELAPSE [15]. The RELAP name (Reactor Excursion and Leak Analysis Program) appeared in 1968 with the RELAP2 code. The homogeneous equilibrium model was used, which assumes an equal velocity, temperature and pressure field for the two phases (see *e.g.* [16]). The RELAP5 code, which was released in 1982, contained a two-fluid, non-equilibrium, six-equation model. The RELAP5/mod3.3 was released in 2001 as the latest modification [15].

The RELAP5/mod3.3 is coded in a modular top-down structure using FORTRAN 77. Separate subroutines are responsible for the models and subtasks in the code. The coding structure supports the straightforward replacement of old models by changing the corresponding subroutine [17].

The flow field equations in RELAP5

The RELAP5 code uses the one-dimensional two-fluid approach for simulating the steam–water mixture. The six-equation model determines the energy and velocity field for both phases balancing mass, momentum and energy. The conservation equations are coupled by a large system of constitutive laws describing the energy and momentum exchange between the two phases and the walls. An instantaneous void fraction indicates the presence of the vapor in the corresponding location. This approach is also called as an interpenetrating media approach [18].

The code allows the presence of non-condensable gases in the vapor phase and soluble components in the liquid phase (*e.g.* boron). These substances obtain the same velocity and temperature as the phase they are embedded in.

The interpenetrating approach generally does not model the stucture of the interfaces or its surface. The local interfacial area concentration is the area for mass, momentum and energy transfer between the phases. The flow equations are solved by time and volume averaged flow parameters, consequently the topology of the phases is lost. The phenomena, which depend on the local flow pattern or transverse gradients, are calculated by empirical correlations.

The state variables in the RELAP5 code are the pressure (P), the internal energies (U_g and U_l), the phasic velocities (v_g and v_l), and the void fraction (ϵ). The non-condensable gas quality (X_n) is a dependent variable as well, when non-condensable gas is present. The time (t) and the distance (x) are the two independent variables. In the thesis, subscripts indicate the gas (g) and liquid (l) phases, and the interface (i) and the wall (w), saturation conditions (s), condensation (c) or boiling (b). The gas is distinguished from the vapor (v) in the thesis, whereas the gas expression allows the presence of non-condensable in the phase, and the vapor assumes pure vapor of the corresponding liquid (mainly water and steam). The superscripts are dedicated to the fluid regions at the wall (W) and the bulk (B). The material properties are the density (ρ), enthalpy (h, details in Table 1.1), latent heat of

phase change (h_{lv}), dissipation terms (*DISS*). The mass sources are indicated by the sign Γ, whereas the S sign shows other source terms. The geometry of the node is represented by the node cross section area (A) in the equations. The heat exchange rate between the phases, or fluid and surfaces is indicted by Q, with the corresponding subscripts.

Two continuity (Eq. 1.1, Eq. 1.2), momentum (Eq. 1.3, Eq. 1.4) and energy (Eq. 1.5, Eq. 1.6) equations are defined for the two phases:

$$\frac{\partial}{\partial t}\left(\epsilon_g \rho_g\right) + \frac{1}{A}\frac{\partial}{\partial x}\left(\epsilon_g \rho_g v_g A\right) = \Gamma_g, \tag{1.1}$$

$$\frac{\partial}{\partial t}\left(\epsilon_l \rho_l\right) + \frac{1}{A}\frac{\partial}{\partial x}\left(\epsilon_l \rho_l v_l A\right) = \Gamma_l, \tag{1.2}$$

$$\epsilon_g \rho_g A\frac{\partial v_g}{\partial t} + \frac{1}{2}\epsilon_g \rho A\frac{\partial v_g^2}{\partial x} = -\epsilon_g A\frac{\partial P}{\partial x} + \Gamma_g A(v_{gi} - v_g) + S_{mom,g}, \tag{1.3}$$

$$\epsilon_l \rho_l A\frac{\partial v_l}{\partial t} + \frac{1}{2}\epsilon_l \rho A\frac{\partial v_l^2}{\partial x} = -\epsilon_l A\frac{\partial P}{\partial x} + \Gamma_l A(v_{li} - v_l) + S_{mom,l}, \tag{1.4}$$

$$\begin{aligned}\frac{\partial}{\partial t}\left(\epsilon_g \rho_g U_g\right) + \frac{1}{A}\frac{\partial}{\partial x}\left(\epsilon_g \rho_g U_g v_g A\right) = -P\frac{\partial \epsilon_g}{\partial t} - \frac{P}{A}\frac{\partial}{\partial x}(\epsilon_g v_g A) \\ + Q_{wg} + Q_{ig} + \Gamma_{ig} h_g^* + \Gamma_w h_g' - Q_{gl} + DISS_g,\end{aligned} \tag{1.5}$$

$$\begin{aligned}\frac{\partial}{\partial t}\left(\epsilon_l \rho_l U_l\right) + \frac{1}{A}\frac{\partial}{\partial x}\left(\epsilon_l \rho_l U_l v_l A\right) = -P\frac{\partial \epsilon_l}{\partial t} - \frac{P}{A}\frac{\partial}{\partial x}(\epsilon_l v_l A) \\ + Q_{wl} + Q_{il} - \Gamma_{ig} h_l^* - \Gamma_w h_l' + Q_{gl} + DISS_l.\end{aligned} \tag{1.6}$$

The right hand side of the equations are the mass, momentum and energy sources, respectively. The force terms of the momentum equations (Eq. 1.3, Eq. 1.4) are the pressure gradient, the momentum transfer due to interface mass transfer and additional term (S_{mom}), which include body force, wall friction, interface frictional drag and force due to virtual mass. For more details on the momentum source see the RELAP5 manual [15].

The derivation of the one-dimensional equation system can be found in the literature (*e.g.* [19], [16]). The system equations are solved using a semi-implicit finite-difference technique [15].

The closure equation for the mass continuity does not allow mass source or sink; therefore, the sum of the liquid and gas generation has to be zero (Eq. 1.7):

$$\Gamma_l + \Gamma_g = 0. \tag{1.7}$$

The RELAP5 code defines two types of mass transfer: Γ_{ig} is the mass transfer at the gas–liquid interface in the bulk fluid, whereas Γ_w is a mass transfer at the gas–liquid interface in

the boundary layer close to the wall (Eq. 1.8) [15]. The Γ_w term results from the wall heat transfer computation:

$$\Gamma_g = \Gamma_{ig} + \Gamma_w. \tag{1.8}$$

The heat transfer terms in the energy equations include the interface (Q_i) and the wall (Q_w) heat exchange. The heat transfer at the interface between the gas and liquid (Q_{gl}) is calculated if non-condensable gas is present. The energy dissipation function ($DISS[W/m^3]$) is the sum of wall friction and pump effects.

The proper choice of the specific enthalpies ensure that the interface temperature remains at saturation temperature (Table 1.1). The choice depends on whether condensation or boiling is calculated. The disappearing phase has an enthalpy of the corresponding temperature, the appearing phase has the enthalpy of the saturation temperature.

Table 1.1: Specific enthalpies for boiling and condensation in RELAP5

	Boiling and isothermal	Condensation
h_g^*	$h_g(T_s)$[1]	$h_g(T_g)$
h_l^*	$h_l(T_l)$	$h_l(T_s)$
h_g'	$h_g(T_s)$	$h_g(T_g)$
h_l'	$h_l(T_l)$	$h_l(T_s)$

* Enthalpy associated with bulk interface mass transfer
′ Enthalpy associated with boundary layer interface mass transfer
[1] The 's' subscript means saturation.

Mass and energy transfer in the energy conservation equation

The RELAP5 code considers the boiling and condensation phenomena by introducing sources in the energy and the mass equations. The code allows superheated and subcooled states for both phases. The subcooling of either phase contributes to condensation; similarly, the superheating contributes to boiling. The phase change processes assume that the phases cool down or heat up to the saturation temperature of the corresponding partial pressure of the steam, where mass and energy transfer occurs. This boundary condition is achieved by using the enthalpies of Table 1.1.

RELAP5 distinguishes between two types of heat transfer processes in the energy equations (Eq. 1.5, Eq. 1.6). The wall heat transfer (Q_w) provides energy directly to the liquid or vapor phase, and phase change can occur without temperature difference between the two phases. The total wall heat transfer is the sum of the gas–wall and liquid–wall heat transfer (Eq. 1.9):

$$Q_w = Q_{wg} + Q_{wl}. \tag{1.9}$$

The second type of heat transfer occurs at the interface between the two phases, if the vapor and liquid temperatures differ. The energy exchange (Q_i) between the two phases in the bulk fluid (Q_i^B) and in the boundary layer close to the wall (Q_i^W) are considered (Eq. 1.10

and Eq. 1.11). The mass and energy transfer rates are determined from the heat balance at the interface between the two phases:

$$Q_{ig} = Q_{ig}^{B} + Q_{ig}^{W}, \tag{1.10}$$

$$Q_{il} = Q_{il}^{B} + Q_{il}^{W}. \tag{1.11}$$

The bulk interface heat transfer happens at the saturation temperature (T_s), and it is calculated by the corresponding heat transfer coefficient (α) and phase temperature (Eq. 1.12-1.13):

$$Q_{ig}^{B} = \alpha_{ig}\left(T_s - T_g\right), \tag{1.12}$$

$$Q_{il}^{B} = \alpha_{il}\left(T_s - T_l\right). \tag{1.13}$$

The sum of the energy equations (Eq. 1.5-1.6) is the mixture energy equation. The interface heat transfer terms are equal to zero (Eq. 1.14) because mass and energy storage is not allowed:

$$Q_{ig}^{B} + Q_{il}^{B} + Q_{ig}^{W} + Q_{il}^{W} + \Gamma_{ig}\left(h_g^* - h_l^*\right) + \Gamma_w\left(h_g' - h_l'\right) = 0. \tag{1.14}$$

This equation represents the total interface energy transfer. The first two terms are the bulk heat transfer terms, the second two are the wall heat transfer terms, whereas the fifth term is the interface latent heat in the bulk, the last term is the interface latent heat near the wall.

Equation 1.14 can be separated into two parts, as both energy exchange terms of the bulk interface and the boundary layer interface sum up to zero independently (Eq. 1.15 and Eq. 1.16, substituting Eq. 1.12-1.13):

$$\alpha_{ig}\left(T_s - T_g\right) + \alpha_{il}\left(T_s - T_l\right) + \Gamma_{ig}\left(h_g^* - h_l^*\right) = 0, \tag{1.15}$$

$$Q_{ig}^{W} + Q_{il}^{W} + \Gamma_w\left(h_g' - h_l'\right) = 0. \tag{1.16}$$

The appearing phase has saturation enthalpy; therefore, in Eq. 1.16 the gas–wall interface heat transfer is zero ($Q_{ig}^{W} = 0$) for condensation. Similarly, the liquid–wall interface heat transfer is zero ($Q_{il}^{W} = 0$) for boiling. The interface energy transfer terms (Eq. 1.17-1.18) are calculated by substituting this expressions and Eq. 1.12-1.13 into Eq. 1.10-1.11. The ϕ factor is equal to -1 for condensation and 1 for boiling:

$$Q_{ig} = \alpha_{ig}\left(T_s - T_g\right) - \frac{1-\phi}{2}\Gamma_w\left(h_g' - h_l'\right), \tag{1.17}$$

$$Q_{il} = \alpha_{il}\left(T_s - T_l\right) - \frac{1+\phi}{2}\Gamma_w\left(h_g' - h_l'\right). \tag{1.18}$$

The interface vaporization or condensation rate in the bulk (Eq. 1.19) is calculated from

rearranging Equation 1.15:

$$\Gamma_{ig} = -\frac{\alpha_{ig}\left(T_s - T_g\right) + \alpha_{il}\left(T_s - T_l\right)}{h_g^* - h_l^*}. \tag{1.19}$$

Equation 1.19 is substituted into Eq. 1.8, obtaining the total mass transfer in the continuity equation (Eq. 1.20):

$$\Gamma_g = -\frac{\alpha_{ig}\left(T_s - T_g\right) + \alpha_{il}\left(T_s - T_l\right)}{h_g^* - h_l^*} + \Gamma_w. \tag{1.20}$$

The mass transfer term near the wall has a condensation mass transfer and a boiling (flushing) mass transfer part (Eq. 1.21):

$$\Gamma_w = \Gamma_c + \Gamma_b. \tag{1.21}$$

The energy equations are reformulated (Eq. 1.22-1.23) by substituting Eq. 1.10-1.11, Eq. 1.21 and using the following expressions: $Q_b = -Q_{il}^W$ and $Q_c = -Q_{ig}^W$; consequently:

$$\begin{aligned}\frac{\partial}{\partial t}\left(\epsilon_g \rho_g U_g\right) + \frac{1}{A}\frac{\partial}{\partial x}\left(\epsilon_g \rho_g U_g v_g A\right) = -P\frac{\partial \epsilon_g}{\partial t} - \frac{P}{A}\frac{\partial}{\partial x}(\epsilon_g v_g A) \\ + Q_{wg} + Q_{ig}^B - Q_c + \Gamma_{ig} h_g^* + \Gamma_b h_g' + \Gamma_c h_g' - Q_{gl} + DISS_g,\end{aligned} \tag{1.22}$$

$$\begin{aligned}\frac{\partial}{\partial t}\left(\epsilon_l \rho_l U_l\right) + \frac{1}{A}\frac{\partial}{\partial x}\left(\epsilon_l \rho_l U_l v_l A\right) = -P\frac{\partial \epsilon_l}{\partial t} - \frac{P}{A}\frac{\partial}{\partial x}(\epsilon_l v_l A) \\ + Q_{wl} + Q_{il}^B - Q_b - \Gamma_{ig} h_l^* - \Gamma_b h_l' - \Gamma_c h_l' + Q_{gl} + DISS_l.\end{aligned} \tag{1.23}$$

Figure 1.4 illustrates the heat transfer process and the sources of the energy equation.

The wall heat transfer correlation package of RELAP5 determines the mass transfer sources. The heat fluxes (q''_g and q''_l) cause energy transfer from the wall (Eq. 1.24-1.25). The flux is calculated by the area of wall heat transfer (A) and the volume of the node (V):

$$Q_{wg} = \frac{1}{V} q''_g A, \tag{1.24}$$

$$Q_{wl} = \frac{1}{V} q''_l A. \tag{1.25}$$

The condensation and boiling mass transfer near the wall is calculated by the heat flux and the factor (m), which is determined by the heat transfer correlation package (Eq. 1.26-1.27):

$$\Gamma_c = m_g \cdot q''_g, \tag{1.26}$$

$$\Gamma_b = m_l \cdot q''_l. \tag{1.27}$$

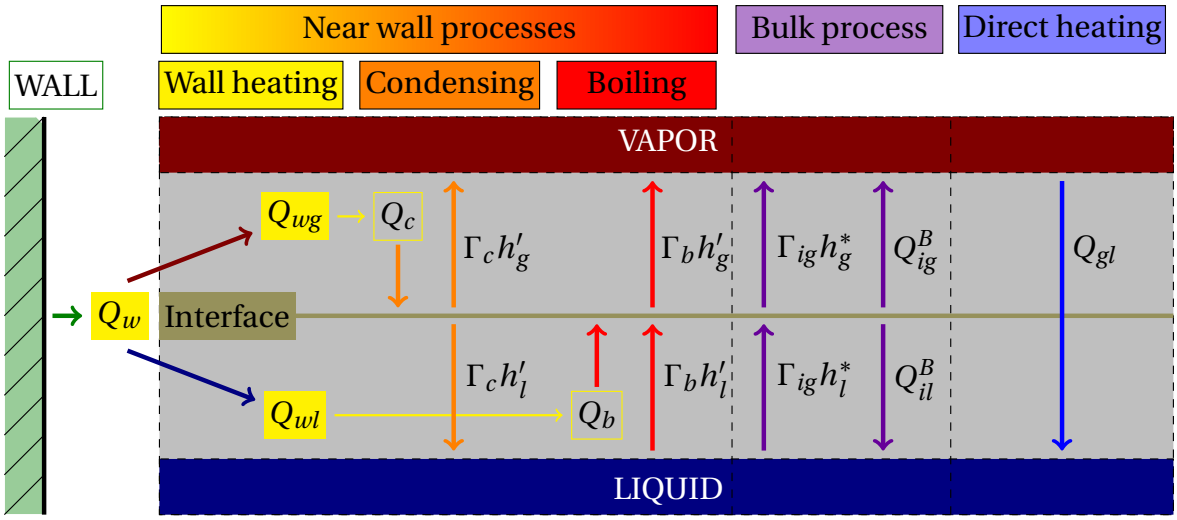

Figure 1.4: Sources in the energy equations: the energy transfer from the wall (Q_w) is divided into wall–gas (Q_{wg}) and wall–liquid (Q_{wl}) energy transfer. RELAP5 assumes that part of this heat goes directly to the liquid–gas interface close to the wall, causing mass transfer between the phases. Boiling (Q_b) and condensation (Q_c) are considered independently. The energy and mass transfer far from the wall in the bulk fluid (Q^B), and a direct heating (Q_{gl}) of the interface between the non-condensable gas and liquid are calculated.

The energy transfer of boiling and condensation is equal to the latent heat of phase change (Eq. 1.28). The energy is transferred directly to the liquid–vapor interface, resulting in mass transfer between the phases:

$$Q_{b,c} = \Gamma_{b,c}\left(h'_g - h'_l\right). \tag{1.28}$$

Condensation heat transfer model in RELAP5

The energy equations (Eq. 1.22-1.23) introduce three types of mass transfer processes between the gas and the liquid phase. The bulk energy and mass transfer is a result of direct contact between the phases, when the gas or the liquid phase is subcooled or superheated. Condensation or boiling can occur near the wall when heat flux is present at the wall (*e.g.* the wall temperature differs from the saturation temperature) (Fig. 1.4). This section focuses on the wall heat transfer models in RELAP5 [10].

The wall heat transfer coefficient is calculated when a convective boundary condition is set at the wall. The general expression for the total heat flux from the wall includes the heat transfer to the gas and liquid (Eq. 1.29):

$$q''_{total} = \alpha^g_g\left(T_w - T_g\right) + \alpha^g_s\left(T_w - T_s(P_t)\right) + \alpha^g_p\left(T_w - T_s(P_p)\right) + \alpha^l_l\left(T_w - T_l\right) + \alpha^l_s\left(T_w - T_s(P_t)\right). \tag{1.29}$$

The equation considers five heat transfer mechanisms depending on the reference temperature of the fluid. The heat flux depends on the temperature difference between the wall and the reference temperature. Usually only one of the heat transfer coefficients is not zero:

- convective heat transfer to non-condensable–steam mixture (α_g^g), the reference temperature is the gas temperature (T_g);
- heat transfer to the gas (α_s^g), the reference temperature is the saturation temperature of the total pressure $T_s(P_t)$;
- heat transfer to the gas (α_p^g), the reference temperature is the saturation temperature of the steam partial pressure ($T_s(P_p)$);
- heat transfer to the liquid (α_l^l), the reference temperature is the liquid temperature (T_l);
- heat transfer to the liquid (α_s^l) the reference temperature is the saturation temperature of the total pressure ($T_s(P_t)$).

The wall heat transfer mode depends on the wall temperature, the void fraction and the non-condensable gas quality (X_n). Condensation heat transfer occurs when the wall temperature is below the saturation temperature of the steam partial pressure, the void fraction is higher than 10%, and the gas phase contains steam. Below 10% void fraction condensation is still possible due to the interfacial mass transfer. Boiling occurs when the wall temperature is higher than the saturation temperature of the total pressure, and liquid is present in the calculation node.

All other scenarios result in convection heat transfer, which is calculated by the Dittus-Boelter correlation [20]. Figure 1.5 shows the selection mechanism for the heat transfer calculation in RELAP5.

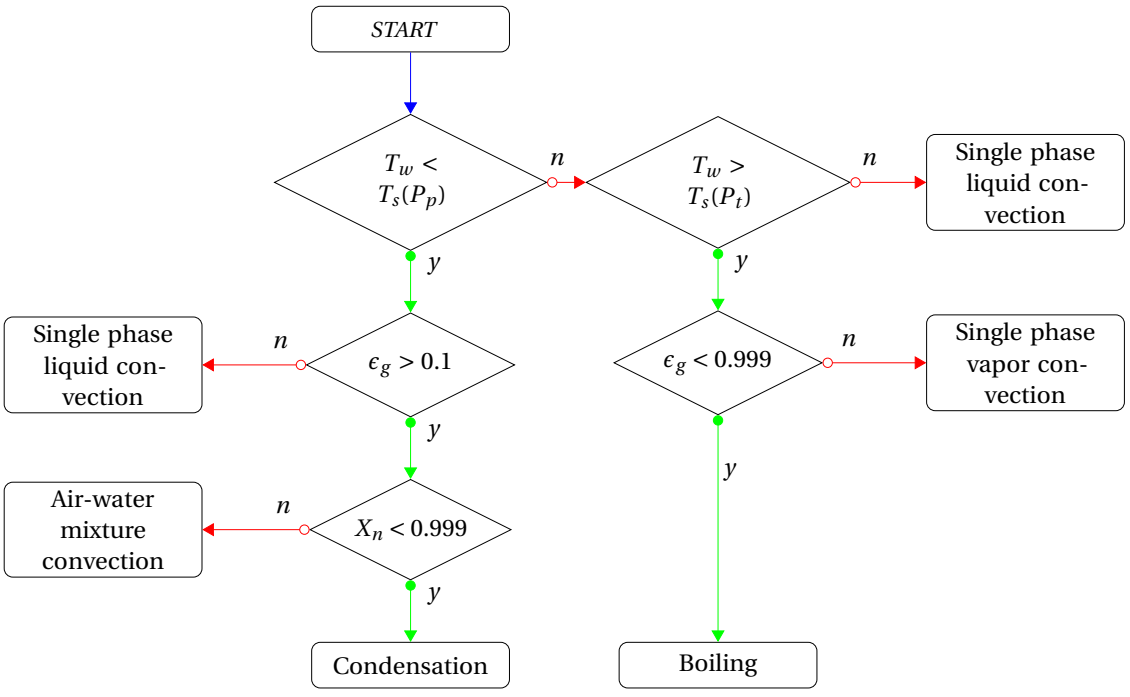

Figure 1.5: Selection process of the wall heat transfer mode in RELAP5

The CONDEN subroutine is called, if the flow conditions fulfill the requirements of wall condensation heat transfer. The total heat flux equation (Eq. 1.29) is reduced to one component, in which α_c corresponds to α_p^g and the saturation temperature corresponds to the saturation temperature at the steam partial pressure in the bulk (Eq. 1.30):

$$q''_{total} = \alpha_c \left(T_w - T_s\right). \tag{1.30}$$

The RELAP5 code calculates the wall heat flux to the liquid (Eq. 1.31):

$$q''_l = \alpha_c \left(T_w - T_l\right). \tag{1.31}$$

The heat flux to the gas is calculated as a difference between the total and the liquid heat flux (Eq. 1.32). This value is used to calculate the mass transfer near the wall (Eq. 1.26):

$$q''_g = q''_{total} - q''_l. \tag{1.32}$$

The CONDEN subroutine calculates the condensation heat transfer coefficient (Eq. 1.30). The applied correlation depends on the pipe inclination angle (θ) and the non-condensable gas quality (Fig. 1.6). The correlations are valid for fully developed flow regimes.

The heat transfer coefficient for horizontal pipes is calculated by the Chato correlation [21]. The maximum value of the turbulent Shah [22] and laminar Nusselt correlations [23] is applied for vertical or inclined pipes. The Colburn-Hougen correlation [24] is a default method to calculate the non-condensable gas effect, the Nusselt UCB model is an alternative model [25], which is based on the U. C. Berkeley single tube condensation studies [26].

The condensation models are used if the void fraction is higher than 30%. A smooth transition to the Dittus-Boelter single phase correlation is ensured by a void fraction ramp between the void fraction values of 10% and 30%.

Dittus Boelter correlation

The Dittus-Boelter correlation for single phase turbulent flow convection calculates the Nusselt number (Eq. 1.33) as a function of the Reynolds number and the Prandtl number. Constants $C = 0.023$ and $n = 0.4$ are coded in RELAP5:

$$\mathrm{Nu} = C \cdot \mathrm{Re}^{0.8} \mathrm{Pr}^n. \tag{1.33}$$

For the single phase laminar flow regime, the correlation of Sellars, Tribu and Klein [27] is used, which neglects the effect of the variable fluid properties on the heat transfer coefficient. It uses a constant value: Nu= 4.36.

Nusselt correlation

The Nusselt correlation (Eq. 1.34) is used for film condensation on vertical surfaces [23]. It

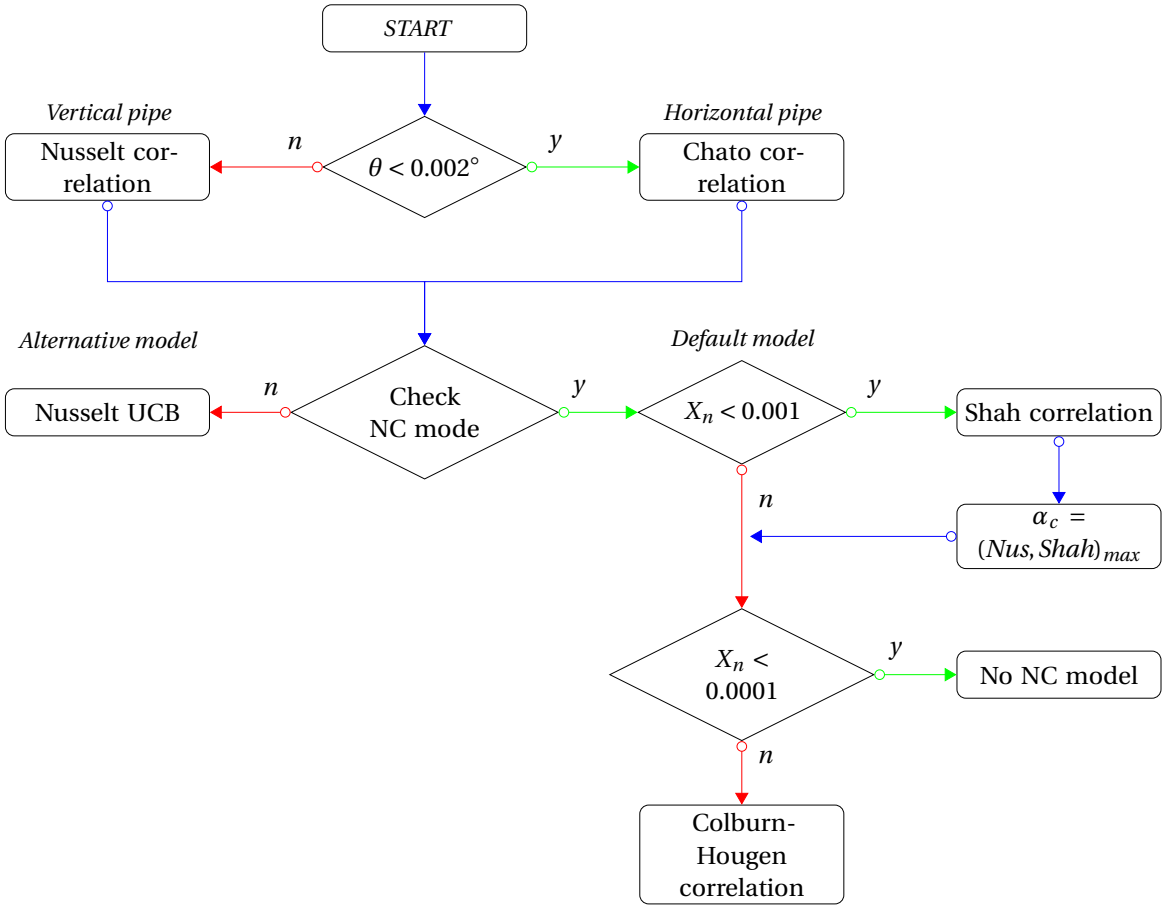

Figure 1.6: Flowchart of the CONDEN subroutine, including the condensation correlations for non-condensable (NC)–steam mixture. UCB stands for the experimental setup, where the correlation was derived [26].

contains the thermal conductivity (λ) and the film thickness (δ):

$$\alpha_{Nu} = \frac{\lambda_l}{\delta}. \tag{1.34}$$

The film thickness (Eq. 1.35) is calculated from the dynamic viscosity (μ), the mass flow rate of the liquid, the density and the gravitational acceleration (g):

$$\delta = \left(\frac{3\mu_l \Gamma_l}{g\rho_l \Delta\rho} \right)^{\frac{1}{3}}. \tag{1.35}$$

Shah correlation

The Shah correlation [22] is used for turbulent film condensation (Eq. 1.36):

$$\alpha_{Sh} = \alpha_{sf} \left(1 + \frac{3.8}{Z^{0.95}} \right). \tag{1.36}$$

The parameters define the followings:

- $Z = \left(\frac{1}{X} - 1\right)^{0.8} (P/P_{critical})^{0.4}$;
- X is the static vapor quality, *i.e.* the ratio of the mass of steam and non-condensable gas mixture divided by the total mass;
- $\alpha_{sf} = \alpha_1 (1 - X)^{0.8}$: superficial heat transfer coefficient;
- $\alpha_1 = 0.023 \frac{\lambda_l}{D_h} \mathrm{Re}^{0.8} \mathrm{Pr}^n$: Dittus-Boelter coefficient, assuming that all fluid is liquid, and using the hydraulic diameter (D_h).

Chato correlation

For condensation in horizontal pipes, the RELAP5 code uses the Chato correlation (Eq. 1.37). The correlation is based on the classical Nusselt formula. A constant multiplicative factor (F) is used to correct the original correlation with the effect of the thicker water flume at the bottom of the tube. The correlation assumes a film condensation on the tube wall; the condensate collects at the bottom part of the tube due to the gravitational force. In the code the constant value $F = 0.296$ is coded. The Chato correlation neglects the local flow pattern and void fraction:

$$\alpha_{Ch} = F \cdot \frac{g \rho_l \Delta\rho h_{lv} \lambda_l^3}{D_h \mu_l (T_s - T_w)}. \tag{1.37}$$

Colburn-Hougen correlation

The non-condensable gas effect is calculated by the Colburn-Hougen method [24]. The correlation was developed for the RELAP5/mod2 code, and it is based on the work of Colburn and Hougen. The correlation uses an iterative process to calculate the liquid–gas interface temperature, if non-condensable gas is present in the gas phase. The model is based on the energy conservation principle. The heat flux due to condensation can be calculated by the gas–steam (Γ_m) mass flux and the latent heat of condensation (h_{lv}) (Eq. 1.38), where the density is the saturated vapor density:

$$q_g'' = h_{lv} \cdot \Gamma_m \rho_g \ln \frac{1 - P_{vi}/P}{1 - P_{vb}/P}. \tag{1.38}$$

The mass transfer coefficient is calculated by empirical correlations. For turbulent vapor flow, the Gilliand correlation (Eq.1.39); for natural convection, the Churchill-Chu correlation (Eq.1.41); and for laminar flow the Rohsenow-Choi correlation (Eq.1.40) is used [10]:

$$\mathrm{Sh} = 0.023 \mathrm{Re}_g^{0.83} \mathrm{Sc}^{0.44}, \tag{1.39}$$

$$\mathrm{Sh} = 4.0, \tag{1.40}$$

$$\mathrm{Nu} = \left(0.825 + \frac{0.387\mathrm{Ra}^{1/6}}{\left[1 + \left(\frac{0.492}{\mathrm{Sc}}\right)^{9/16}\right]^{8/27}} \right)^2 . \tag{1.41}$$

The following expressions were used:

- Sherwood number (mass transfer Nusselt number): Sh= $\Gamma_m D_h / D_n$,
- Schmidt number: Sc= $\mu_v / \rho_v D_v$,
- D_h is the hydraulic diameter, D_n and D_v is the non-condensable and vapor mass diffusivity.
- Nusselt number (Nu),
- Rayleigh number: Ra= $\mathrm{Gr_{LD}}$·Sc,
- Grashof number: Gr= $\frac{\left(\rho_m^B\right)^2 g |\rho_m^W - \rho_m^B| L^3}{\left(\mu_m^W\right)^2 \rho_m^W}$,
- where m stands for the non-condensable gas–steam mixture, W stands for the wall, B for the bulk region.

The mass diffusivity of a non-condensable gas is calculated from the equation of Fuller, Scettler and Giddings [10].

The heat flux from the liquid film to the wall (Eq. 1.42) is equal to the condensation heat flux at the liquid interface:

$$q_l'' = \alpha_c \left(T_{vi} - T_w\right). \tag{1.42}$$

An iteration process finds the proper heat transfer coefficient value by satisfying the energy balance principle.

The above introduced heat transfer mechanism is a state of the art method for system codes. Other system codes, as well, use the same set of conservation equations; however, the applied correlations for heat transfer processes differ. The next section summarizes the heat transfer coefficient correlations for the TRACE code, which was also used in this thesis.

1.2.2 Condensation heat transfer model in TRACE

The U.S.NRC decided in the mid 1990's to develop a thermal hydraulic system code called TRACE (TRAC/RELAP Advanced Computational Engine) which includes the capabilities of the previously maintained codes (RELAP5, RAMONA, TRAC-P and TRAC-B) [11]. TRACE is the latest design of advanced, best estimate reactor system codes of the U.S.NRC.

The wall heat transfer correlations of the TRACE code differ from the RELAP5 models. The TRACE code assumes film condensation process if the void fraction is higher than 80%, and the wall temperature is lower than the saturation temperature of the gas (Fig. 1.7).

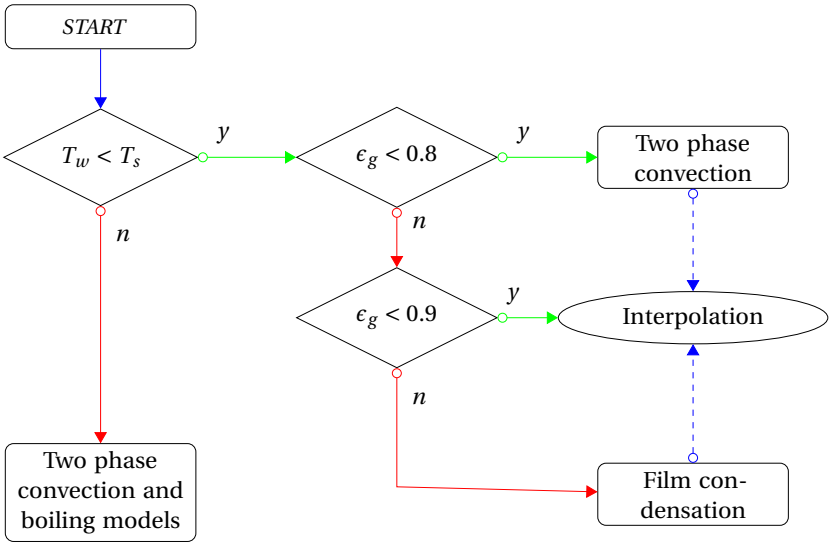

Figure 1.7: Flowchart of the wall heat transfer calculation in TRACE

The liquid–wall heat transfer coefficient (α_{wl}) is calculated from the Nusselt number at the wall, the thermal conductivity of the liquid (λ) and the liquid film thickness (δ) (Eq. 1.43):

$$\alpha_{wl} = \frac{\lambda_l}{\delta} \cdot \mathrm{Nu}_{wl}. \tag{1.43}$$

The film thickness is used as a characteristic length; therefore, the model can be applied over a wide range of Reynolds numbers. The wall–liquid Nusselt number is calculated by a power-law weighting of laminar and turbulent Nusselt numbers (Eq. 1.44), and the film thickness is calculated from the void fraction (ϵ) and the hydraulic diameter (D_h) of the pipe (Eq. 1.45):

$$\mathrm{Nu}_{wl} = \left(\mathrm{Nu}_{lam}^2 + \mathrm{Nu}_{turb}^2\right)^{1/2}, \tag{1.44}$$

$$\delta = \frac{D_h}{2}\left(1 - \sqrt{\epsilon}\right). \tag{1.45}$$

TRACE uses correlations for laminar, turbulent flows and for non-condensable cases. The maximum value of the turbulent, laminar and natural convection heat transfer coefficients is the single phase convection heat transfer at the wall. The following part describes the TRACE heat transfer models.

Two phase convection models

The two phase convection model uses a single phase heat transfer correlation with a multiplier, which accounts for the two-phase effect. TRACE defines a two-phase Reynolds number (Eq. 1.46), which is used to evaluate the Nusselt number for turbulent forced convection in tubes:

$$\mathrm{Re}_{2\Phi} = \frac{G_l D_h}{(1-\epsilon)\mu_l} = \frac{\rho_l v_l D_h}{\mu_l}. \tag{1.46}$$

The single phase laminar convection model (Eq. 1.47) is used for laminar flow regimes, if

bubbly and slug flow is present [27]. Fully developed flow is assumed with a constant heat flux boundary condition. The effect of variable fluid properties and the entrance length effects are neglected:

$$\mathrm{Nu} = 4.36. \tag{1.47}$$

For annular flow regimes, the characteristic length in the Nusselt number calculation is the thickness of the annular film.

Interpolation between the two-phase convection and condensation models

The interpolation (Eq. 1.48) of the two-phase convection ($\alpha_{2\Phi}$) and the condensation heat transfer coefficient (α_c) is used between the void fraction values 0.8 and 0.9:

$$\alpha_{wl} = \alpha_c \frac{\epsilon - 0.8}{0.9 - 0.8} + \alpha_{2\Phi}\left(1 - \frac{\epsilon - 0.8}{0.9 - 0.8}\right). \tag{1.48}$$

Gnielinski correlation

The Gnielinski correlation [28] is applied (Eq.1.49) for turbulent convection heat transfer. The Gnielinski correlation differs from the Dittus-Boelter only in the transition region (1000 <Re < 3000). The correlation is valid for the transition between laminar and turbulent flow regimes as well:

$$\mathrm{Nu}_{turb} = \frac{(f/2)(\mathrm{Re} - 1000)\mathrm{Pr}}{1 + 12.7(f/2)^{1/2}\left(\mathrm{Pr}^{2/8} - 1\right)}. \tag{1.49}$$

The friction factor is: $f = [1.58\ln(\mathrm{Re}) - 3.28]^{-2}$.

Natural convection heat transfer correlation

A maximum value of the laminar (Eq. 1.50) and the turbulent (Eq. 1.51) Nusselt numbers is used for natural convection:

$$\mathrm{Nu}_{N,lam} = 0.1 \cdot (\mathrm{Gr}_l \cdot \mathrm{Pr}_l)^{1/8}, \tag{1.50}$$

$$\mathrm{Nu}_{N,turb} = 0.59 \cdot (\mathrm{Gr}_l \cdot \mathrm{Pr}_l)^{1/4}. \tag{1.51}$$

Kuhn, Schrock and Peterson correlation

The Nusselt number is unity (see the laminar forced convection above), if smooth laminar film condensation is present. The film Reynolds number is calculated, and if it is higher than 20, a laminar–wavy falling film correlation will be used. Thus, the empirical correlation of Kuhn, Schrock and Peterson [29] was implemented into the TRACE code (Eq.1.52):

$$\mathrm{Nu}_{lam} = 2\left(1 + 1.83 \times 10^{-4} \cdot \mathrm{Re}_l\right). \tag{1.52}$$

Turbulent film condensation correlation

For the turbulent wall heat transfer model of TRACE, the modification of the Gnielinski correlation (Eq.1.53) was chosen. The correlation is based on the observation that the hydraulic diameter for the thin liquid film is four times of the film thickness:

$$\mathrm{Nu}_{turb} \approx \frac{1}{4}\mathrm{Nu}_{Gn}. \tag{1.53}$$

Non-condensable gas effect

The presence of non-condensable gases significantly reduce the condensation heat transfer. The non-condensable gas accumulates at the liquid vapor interface. The partial pressure of the steam reduces because the increasing non-condensable fraction; consequently, the driving potential for the heat transfer through the liquid film decreases. The model for film condensation in the presence of non-condensable gases applies the mass transfer conductance approach [29]. This approach is similar to the Colburn-Hougen method, which was described in the previous section. The Nusselt and the Sherwood numbers are calculated using the Gnielinski correlation. For more details, see the TRACE manual [11].

1.2.3 Literature review on condensation in one-dimensional modeling

Condensation heat transfer is an efficient heat removal process; therefore, it is widely used not only in nuclear industry, but in air conditioning systems, refrigeration industry and electric power industry. This section reviews the calculation methods for condensation, with a focus on one-dimensional techniques and horizontal pipes.

Shah [30] summarized the empirical condensation heat transfer correlations used for vertical and horizontal pipes. His evaluation states that the Chato correlation is the most reliable tool for horizontal pipes. The general correlation of Shah [22] is optimized for refrigeration systems, and it is aiming to calculate the heat transfer coefficient for both vertical and horizontal systems. Dalkilic and Wongwises [31] concluded that most of the proposed models to compute the heat transfer coefficient for two-phase flows in smooth horizontal tubes are based on the modification of the Dittus-Boelter single-phase forced convection correlation; therefore, they are clearly empirical correlations.

The characteristic of the condensation heat transfer in horizontal pipes is highly dependent on the local flow pattern and the interaction of the vapor and liquid phases [31]. The flow pattern occurs according to the inclination and the geometry of the tube, flow rates of the phases, and physical properties of the fluids. The local void fraction and flow patterns are important in heat transfer prediction [32]. The heat transfer depends on the flow regime and on the relative importance of inertial and gravitational forces on the liquid film [33].

The two main flow patterns occurring in horizontal pipes are the annular flow and the stratified flow regimes (Fig. 1.8). Two-phase annular flow occurs widely in film heating and

cooling processes, particularly in power generation. Stratified flow occurs in a horizontal tube at low vapor velocities. The dominance of either annular of stratified slow regimes was confirmed by experiments in a single tube by Schaffrath *et al.* [34] and Li *et al.* [35] for the pipes in the emergency core cooling system of the KERENA. The slug and wavy flows can be characterized as stratified flows, as they have a stratified flow nature [36].

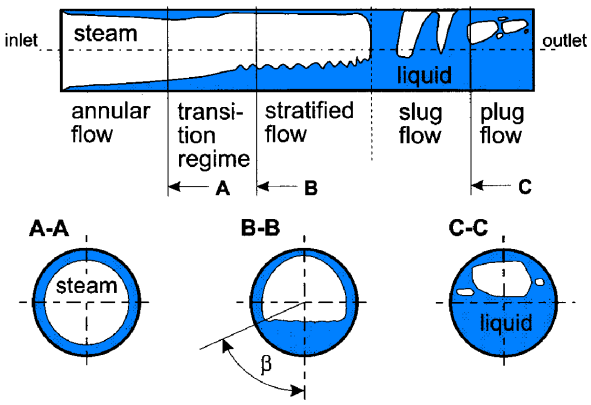

Figure 1.8: Developing flow patterns during condensation in a horizontal tube [37]

The annular flow regime is usually treated as an axial turbulent flow with uniform film thickness. The dominant heat transfer process is the convective heat transfer between the wall and the flow [38], [39].

The stratified flow regime can be divided into three parts. Vapor core exists in the middle of the tube cross section, whereas the stratification angle (β) divides the liquid phase into two well distinguished sections. Steam condenses on the tube wall, presenting a thin liquid film at the upper part of the tube. The film drains toward the bottom due to the gravity, where the condensate accumulates forming an axial flume.

The heat transfer of the axial flume is usually neglected, the experimental work of Chato justified this assumption [40]. However, Dobson and Chato [41] concluded that at high mass velocities and low qualities, when waves can occur at the liquid–vapor interface, the bottom part heat transfer coefficient has a contribution.

Heat transfer through the thin film is usually calculated by the classical Nusselt theory for film condensation [33]. The accumulated liquid at the bottom of the pipe reduces the heat transfer surface in a cross section of the pipe. Correlations consider this effect by using a multiplication factor in the Nusselt correlation. The multiplication factor is either constant [40], [42] or void fraction dependent [43], [44].

Chato (1960) [40] investigated analytically the heat transfer phenomenon inside horizontal and slightly inclined condensation tubes. He analyzed the condensate film on the upper part by two independent methods; the solution of both methods do not differ significantly from the simplest approximation developed by Nusselt. Chato concluded that the temperature variation of the wall along the cross section and the subcooling of the liquid phase are

insignificant effects. The Chato correlation, which is used in the RELAP5 code, neglects the varying stratification angle, and uses an average value along the tube. The correlation is valid if the outlet and the inlet void fractions have similar values.

Choi *et al.* [45] analyzed direct contact condensation heat transfer for stratified flow regimes with the RELAP5 code. They concluded that the results fit well to the co-current database, but not to the counter-current database. They suggested to improve the condensation heat transfer by considering the liquid film thickness [46].

The German ATHLET code considers six flow patterns in the condensation heat transfer correlation [37]. The empirical flow regime map of Tandon identifies the transition between the flow regimes. Semi-empirical correlations are applied to calculate the heat transfer coefficient. The stratified flow regime calculation uses a void fraction dependent correlation [43]. The condensation model was optimized to calculate the heat transfer coefficient of the emergency core cooling system of the KERENA reactor [47].

El Hajal *et al.* [48] and Thome *et al.* [49] used three simplified flow regimes to describe the flow in horizontal pipe condensation. The flow patterns are annular flow with uniform film thickness, stratified–wavy flow with various stratified angle, and stratified flow with flat liquid surface. Turbulent convection heat transfer is used for annular flow. The modified Nusselt theory is used for the stratified flow regime.

Apart from empirical correlations, analytical studies also exist for condensation heat transfer. Chitti *et al.* [38] described a fully analytical model for annular condensation. Kwon [39] used turbulent eddy viscosity model with liquid droplets in the vapor phase. Sarma *et al.* [50] used homogeneous model approach to estimate the shear velocity. Stevanovic and Studovic [51] developed a simple one-dimensional three-fluid model to simulate annular flow in vertical pipes and stratified flow in horizontal pipes.

Lips and Meyer [52] designed experiments for condensation of R134a in a 8.38 mm inner diameter tube with inclined orientation. They proposed a new mechanistic model for stratified flow regime. The model considers the capillary effect in thin tubes, which results in a non-flat liquid–vapor surface. The falling film is calculated by the Nusselt theory; the equation is based on the analytical solution calculated by Fieg and Roetzel [53]. The liquid pool shape of the bottom axial flow is calculated by the capillary and gravitational forces. The flume is divided into trapezoidal control volumes; and the local heat transfer coefficient is calculated for each control volume.

The literature review showed that the condensation heat transfer coefficient is calculated by empirical correlations in thermal-hydraulic system codes. The empirical models suffer from a lack of generality, which makes the use of these correlations questionable for new developments in nuclear power plants. Analytical models exist to calculate the condensation heat transfer for horizontal pipes.

1.3 Multiphase modeling with computational fluid dynamics codes

The second approach for simulating condensation was three-dimensional computational fluid dynamics (CFD). This section introduces the main characteristics of the CFD codes.

Computational fluid dynamics is a numerical technique to solve the partial differential equations of fluid mechanics by transforming them into algebraic equations. The mathematical equations of the fluid state are discretized on a mesh, which contains finite-size cells. The chosen set of equations and models are solved for a transient simulation by an integration over time and for obtaining steady-state solutions iteratively, according to the boundary and initial conditions.

The ANSYS FLUENT was used to calculate the flow field in this thesis. The FLUENT code [54] is a numerical solver to calculate flow fields for compressible and incompressible flows, turbulent or laminar flows, steady-state or transient situations. Four methods are available to calculate multiphase flows. The discrete phase model calculates the Lagrangian trajectories for particles, droplets or bubbles, coupling with the continuous phase. The Eulerian model solves the set of momentum and continuity equations under the assumption that both phases represent independent fluids with separate, interpenetrating flow fields, which are coupled by a model for interfacial friction and mass conservation. The mixture model treats the phases as interpenetrating media as well, but solving only one momentum equation for the mixture. The relative velocity between the phases and the mixture velocity can be modeled by an algebraic relation. The volume of fluid (VOF) method is an interface tracking method.

The VOF method is applicable for flows with a gas-liquid interface that can be fully resolved on the scale of the applied discretisation grid. It provides fast calculations and intrinsic mass conservation. A single set of conservation equations is solved along with a volume fraction equation, which tracks the interface.

The nature of the phase change phenomenon analyzed in this thesis, *i.e.* the condensation in horizontal geometries, is highly stratified. Therefore, the interface tracking algorithm is suitable to calculate the flow field. The VOF method available in FLUENT is designed for adiabatic flows. Extensions are needed to reflect the phase transition at the interface, as well as the occurring heat fluxes, while the sudden change of fluid parameters is covered by the standard VOF model.

This section presents the FLUENT software and the VOF method [55]. The physical models and solver techniques, relevant for the thesis, will be introduced as well. The literature review, presenting the state of the art in multiphase modeling with CFD codes, is in Section 1.3.2.

1.3.1 The flow equations of the FLUENT volume of fluid model

FLUENT solves the conservation equations for mass, momentum and energy. Turbulent transport equations are solved, if the flow is turbulent. The VOF method is based on a single set of conservation equations for the continuous fluid. An additional transport equation of the volume fraction tracks the interface between the phases.

The general form of the continuity equation (Eq. 1.54) is valid for both compressible and incompressible flows. The velocity vector ($\vec{v}$) has two or three components, depending whether dealing with a two or three-dimensional problem. The source term (S_m) can be added by user defined functions in FLUENT (details in Section 3.4):

$$\frac{\partial \rho}{\partial t} + \nabla \left(\rho \vec{v}\right) = S_m. \tag{1.54}$$

The momentum conservation equation (Eq. 1.55) contains the gradient of the static pressure (p), the gravitational body force ($\vec{g}$) and an external source ($\vec{F}$):

$$\frac{\partial}{\partial t}\left(\rho \vec{v}\right) + \nabla \left(\rho \vec{v}\vec{v}\right) = -\nabla p + \nabla \left(\mu \left(\nabla \vec{v} + \nabla \vec{v}^T\right)\right) + \rho \vec{g} + \vec{F}. \tag{1.55}$$

The energy equation (Eq. 1.56) contains the conduction heat transfer (the $\lambda_e = \lambda + \lambda_t$ effective thermal conductivity is defined by the turbulence model), and other, user defined volumetric heat sources (S_h):

$$\frac{\partial}{\partial t}\left(\rho E\right) + \nabla \left(\vec{v}\left(\rho E + p\right)\right) = \nabla \left(\lambda_e \nabla T\right) + S_h. \tag{1.56}$$

The FLUENT code has two-equation turbulence models, which allow the determination of turbulent length and time scale. The $k-\epsilon$ semi-empirical model solves transport equations for the turbulent kinetic energy (k) and its dissipation rate (ϵ) [54].

In this thesis, the $k-\omega$ empirical model [56] was used. The transport equations account for the kinetic energy (Eq. 1.57) and the specific dissipation rate (ω) (Eq. 1.58), which is a ratio of ϵ and k. The source terms are the generation term due to mean velocity gradients (G), the turbulent dissipation (Y), and additional sources (S). The diffusion term contains the effective diffusivity (Γ) for k and ω:

$$\frac{\partial}{\partial t}\left(\rho k\right) + \nabla \left(\rho k \vec{v}\right) = \nabla \left(\Gamma_k \nabla k\right) + G_k - Y_k + S_k, \tag{1.57}$$

$$\frac{\partial}{\partial t}\left(\rho \omega\right) + \nabla \left(\rho \omega \vec{v}\right) = \nabla \left(\Gamma_\omega \nabla \omega\right) + G_\omega - Y_\omega + S_\omega. \tag{1.58}$$

The effective diffusivity (Eq. 1.59) accounts for the turbulent viscosity (Eq. 1.60):

$$\Gamma_i = \mu + \frac{\mu_t}{\mathrm{Pr}_t^i} \qquad \text{for} \quad i = k, \omega, \tag{1.59}$$

$$\mu_t = a^* \frac{\rho k}{\omega}. \tag{1.60}$$

The coefficient in the turbulent viscosity equation (a^*) is responsible for the low Reynolds number correction (Eq. 1.61), which has a value of one for high Reynolds numbers. The turbulent Reynolds number is defined as Eq. 1.62:

$$a^* = \frac{0.024 + \mathrm{Re}_t/6}{1 + \mathrm{Re}_t/6}, \tag{1.61}$$

$$\mathrm{Re}_t = \frac{\rho k}{\mu \omega}. \tag{1.62}$$

The high velocity gradients at the interface between the phases generate high turbulence in the two-equation turbulence models. Therefore, the damping of the turbulence is needed, which is implemented in the $k-\omega$ model of FLUENT. The turbulence damping model is analog to the damping next to a solid wall, and it is applied on both sides of the interface by adding a source term to the ω transport equation (Eq. 1.63). The equation contains the interfacial area density (A), the cell dimension normal to the interface (Δn), a destruction term ($\beta = 0.075$) and a damping factor (B):

$$S_i = A_i \Delta n \beta \rho_i \left(\frac{6 B \mu_i}{\beta \rho_i \Delta n^2} \right)^2. \tag{1.63}$$

The interfacial area density is calculated from the volume fraction gradient (Eq. 1.64):

$$A_i = 2 \epsilon_i \left| \nabla \epsilon_i \right|. \tag{1.64}$$

The damping factor has a default value of 10. The damping term is calculated for both phases and it is a source of the mixture level ω–equation. For further information on the $k-\omega$ model see the FLUENT manual [54].

The VOF method [57] introduces a volume fraction equation. The model assumes that the phases are not interpenetrating, and that the flow field is stratified, *i.e.* an interface between the phases is clearly defined. The new variable is the volume fraction (ϵ) in the center of the node for all the phases. The number of phases (n) is defined by the user. The void fraction is equal to one, if the corresponding phase (generally q or p) occupies the node, and it is equal to zero if it is not present in the node. The non-zero (or one) value of the volume fraction indicates the presence of the interface in the cell. The mass transfer from one phase to an other is indicated in the subscript of the mass source (*e.g.* $\dot{m}_{pq}$). An additional source term is introduced for the user defined mass sources ($S_{\epsilon q}$). The solution of the volume fraction continuity equation provides the information about the location of the interface (Eq. 1.65):

$$\frac{\partial}{\partial t} \left(\epsilon_q \rho_q \right) + \nabla \left(\epsilon_q \rho_q \vec{v}_q \right) = S_{\epsilon q} + \sum_{p=1}^{n} \left(\dot{m}_{pq} - \dot{m}_{qp} \right). \tag{1.65}$$

The sum of the volume fraction for all of the phases is one (Eq. 1.66):

$$\sum_{q=1}^{n} \epsilon_q = 1. \tag{1.66}$$

If the two phases are gas and liquid, the phases are defined as follows: $n = 2$, $q = g$, $p = l$.

The material properties are a volume fraction weighted average of the phase properties (Eq. 1.67). One momentum equation (Eq. 1.55) and one energy equation (Eq. 1.56) are solved, which contain information about the phases through the material properties:

$$\rho = \epsilon_g \rho_g + \epsilon_l \rho_l. \tag{1.67}$$

The energy (E) and the temperature (T) are mass-averaged variables (Eq. 1.68). The energy of each phase is based on the specific heat of the phase and the shared temperature:

$$E = \frac{\epsilon_g \rho_g E_g + \epsilon_l \rho_l E_l}{\epsilon_g \rho_g + \epsilon_l \rho_l}. \tag{1.68}$$

Built-on phase change model is not available for the VOF multiphase model, *i.e.* the source terms are zero by default. The source terms in the energy (S_h) and the volume fraction equations ($\dot{m}$) can be modified by user defined functions (details in Section 3.4).

1.3.2 Calculation of the phase-change heat and mass transfer - a review

Computational fluid dynamics codes are valuable tools for the analyses of multiple phase flows, as they provide details about the three dimensional flow field and transport phenomena. The direct numerical solution of the transport equations of two-phase flows with phase change are computationally expensive, and, therefore, only possible in few selected cases of academic value. The investigation of the interfacial phenomena remains a challenge in CFD calculations, as our knowledge is not established about the interface turbulent effects, and the available resources limit the resolution at the interface. Consequently, assumptions have to be made to achieve realizable models.

Moreover, already the simulation of adiabatic two-phase flows introduces difficulties. The VOF method can not simulate two-phase flows with high velocity differences between the phases. Bartosiewicz *et al.* [58] highlighted this issue in a simulation of slug formation in an air–water channel. Lan *et al.* [59] showed that a fine resolution of the interface is critical for modeling thin liquid films. The boundary and initial conditions are crucial in two-phase flow modeling [60] [61]. If phase transition occurs between the two phases, additional complications rise.

Phase transition can be grouped to homogeneous and heterogeneous processes. Should the condensation or boiling occur at the interface between the phases or on a solid surface, we talk about heterogeneous transition. For homogeneous phase change, which happens in strongly superheated or subcooled medium spontaneously, the CFD calculation requires

nucleation and droplet growth models [62], [63].

Heterogeneous phase change is important in many industrial applications, when the involved surface or interface has either lower (condensation) or higher (boiling) temperature than the saturation temperature at the corresponding pressure.

Condensation occurs on surfaces or at an already existing interface. The geometry gas-liquid interface depends on whether the surface is wettable (film condensation) or not (drop-wise condensation). Direct contact condensation occurs, if the vapor is in contact with it's subcooled liquid.

The mass transfer between the phases, *i.e.* the boiling, condensation or solidification processes introduce additional sources in the continuity equations. The phase transition related heat source (Q) is calculated (Eq. 1.69) from the phase change mass transfer ($\dot{m}$) multiplied by the latent heat (h_{lv}):

$$Q = \dot{m} h_{lv}. \tag{1.69}$$

Condensation or boiling is calculated by identifying the phase mass transfer, which is a result of a simulation of the mass transfer.

The limited computational resources motivate a simulation technique, which reduces the number of equations. Dehbi *et al.* [64], [65] used the FLUENT code and the single phase approach to investigate wall condensation in a presence of non-condensable gases. Negative source terms in the conservation equations accounted for the mass, momentum and energy losses from the gas phase, while the growing liquid film was not simulated.

Štrubelj *et al.* [66] used a two-fluid method to calculate direct contact condensation with the NEPTUNE_CFD code. They assumed that the steam is at saturation condition; therefore, the energy equation of the vapor phase was not solved. They calculated the interface mass flow rate ($\dot{m}$) depending on the heat transfer coefficient (α_{np}) and the temperature difference between the liquid (T_l) and the saturation (T_s) temperatures at the interface (Eq. 1.70):

$$\dot{m} = \frac{\alpha_{np}(T_s - T_l)}{h_{lv}}. \tag{1.70}$$

The liquid heat transfer coefficient (Eq. 1.71) is calculated from the Nusselt number (Nu_l in Eq. 1.72), which is a function of the Prandtl number (Pr) and the turbulent Reynolds number (Re_t). The correlation is based on the renewal theory and the Hughes–Duffey correlation [67]:

$$\alpha_{np} = \frac{\lambda_l \mathrm{Nu}_l}{h_{lv}}, \tag{1.71}$$

$$\mathrm{Nu}_l = \frac{2}{\sqrt{\pi}} \mathrm{Re}_t \mathrm{Pr}^{1/2}. \tag{1.72}$$

The turbulent Reynolds number (Eq. 1.73) contains the length scale ($L_t = C_\mu k_l^{1/4}/\epsilon_l$), the friction velocity ($u^* = C_\mu^{1/4} k_l^{1/2}$, $C_\mu = 0.09$), where k_l is the turbulent kinetic energy, ϵ_l is the

turbulent dissipation and v is the kinematic viscosity:

$$\mathrm{Re}_t = \frac{L_t u^*}{v_l}. \tag{1.73}$$

The surface renewal theory predicts the condensation mass transfer from the liquid turbulent properties and the renewal period of the eddies [68]. The theory suggests that turbulent eddies transport bulk liquid, which has lower temperature, to the surface, and remove saturated condensate from the interface. The temperature gradient at the interface thus increases, which enhances the condensation compared to laminar heat conduction. The renewal period controls the contact time between the bulk liquid and the saturated vapor; consequently, this is the driving force for the condensation mass transfer. The renewal theory calculates the effect of the reduced interfacial shear and the eddy diffusivity distribution on heat and mass transfer by directly deriving them from the momentum transfer.

The derived heat transfer coefficient depends on the applied length and velocity scale. An example is the Hughes Duffey correlation [67], which uses a turbulent eddy based surface renewal theory and the Kolmogorov turbulent length theory to predict the condensation heat transfer coefficient at the vapor–liquid interface:

$$\alpha_{HD} = \frac{2}{\sqrt{\pi}} \lambda_l \left(\frac{\mu_l C_{pl}}{\lambda_l} \right)^{1/2} \left(\frac{\epsilon}{v_l} \right)^{1/4}. \tag{1.74}$$

The Hughes-Duffey correlation was used to calculate direct contact condensation in the LAOKOON experiment, which is discussed in this thesis (Section 1.4.2) [69], [70], [71].

Ceuca and Macián-Juan implemented two surface renewal theory based correlations into the ANSYS CFX software, and calculated direct contact condensation [72]. Next to the Hughes-Duffey correlation, the Shen correlation was used:

$$\alpha_{Sh} = \frac{1.407}{\sqrt{\pi}} \lambda_l \left(\frac{\mu_l C_{pl}}{\lambda_l} \right)^{1/2} \left(\frac{C_\mu k^{1/2}}{\epsilon} \right)^{-1/3} \left(\frac{C_\mu^{1/2} (v_l \epsilon)^{1/4}}{v_l} \right)^{2/3}. \tag{1.75}$$

The Shen correlation considers large eddies, which transport the heat away from the interface. Therefore, the renewal period is longer, the removed heat is smaller in the Shen correlation. Ceuca and Macián-Juan achieved better results with the Shen model.

Lakehal and Labois [73] used very large eddy simulation within the ASCOMP TransAt code to derive a heat transfer coefficient correlation at the liquid vapor interface for direct contact condensation. They used surface divergence theory to define a correlation between the turbulence of the liquid and the heat and mass transfer at the interface based on the direct numerical simulation.

The surface divergence theory (Eq. 1.76) calculates the ratio between the transfer velocity (K) and the turbulent velocity scale (u_t):

$$\frac{K}{u_t} = C \cdot \mathrm{Pr}^n \cdot f\left[\mathrm{Re}_t\right] \mathrm{Re}_t^m. \tag{1.76}$$

The model constant C depends on liquid properties, the exponents (n and m) are governed by the surface condition and turbulence intensity. The surface divergence function (f) depends on whether small-eddy or large-eddy model were used (Eq. 1.77):

$$f\left[\mathrm{Re}_t\right] = \left[0.3\left(2.83\mathrm{Re}_t^{3/4} - 2.1\mathrm{Re}_t^{2/3}\right)\right]^{1/4}. \tag{1.77}$$

The correlation was validated for the level set interface tracking method [74] by modeling stratified steam–water flows [75].

Apart from the empirical or semi-empirical correlations, authors used analytical methods to calculate the mass transfer at the interface. Zhaohui *et al.* [76] calculated condensation induced water hammer phenomenon with the VOF method, the mass transfer rate (Eq. 1.78) was derived from the kinetic theory of gases [16]. The condensing rate is calculated from the relative molecular mass (M_r), the universal gas constant (R), the phasic absolute pressure (P) and temperature (T), and a condensing coefficient ($\sigma = 0.03 - 0.05$) for water:

$$\dot{m} = \left(\frac{M_r}{2\pi R}\right)^{1/2} \left[\frac{P_g}{T_g^{1/2}} - \frac{P_l}{T_l^{1/2}}\right] \frac{2\sigma}{2-\sigma}. \tag{1.78}$$

Liu *et al.* [77] implemented the Hertz-Knudsen gas kinetic model into the FLUENT code, which is also available in the FLUENT Eulerian multiphase method [54]. They used the VOF method to simulate laminar film condensation on parallel vertical walls. The phase change mass flow rate (Eq. 1.79) is proportional to the void fraction (ϵ_g), to the relative temperature difference between the interface and saturation temperature, the gas density (ρ_g) and a condensation coefficient (β) :

$$\dot{m} = \beta_c \epsilon_g \rho_g \frac{T_i - T_s}{T_s}. \tag{1.79}$$

The condensation coefficient depends on molecular constants (Eq. 1.80), as the molecular mass (M), the Sauter mean diameter (D_{sm}), the accommodation coefficient (a_c) and the universal gas constant (R) :

$$\beta_c = \frac{6}{D_{sm}} a_c \sqrt{\frac{M}{2\pi R T_s}} \frac{\rho_l h_{lv}}{\left(\rho_l - \rho_g\right)}. \tag{1.80}$$

The condensation coefficient was found by a trial-and-error procedure. Consequently, the so called Hertz-Knudsen kinetic theory model is equivalent to the iterative technique introduced by Lee [78].

The model of Lee imposes the boundary condition that the liquid vapor interface is at

saturation temperature. The mass transfer is introduced in the cell such that the boundary condition is reached through iteration. The iteration speed is governed by the relaxation time (r), which is equivalent to the condensation coefficient in the Hertz-Knudsen method (Eq. 1.80). Should the temperature of an interfacial cell differ from the saturation temperature, phase change is introduced (Eq. 1.81 and 1.82):

$$\dot{m} = -r\epsilon_l \rho_l \frac{T - T_s}{T_s} \qquad \text{if} \quad T \geq T_s \quad \text{and} \quad |\nabla \epsilon_l| > 0, \tag{1.81}$$

$$\dot{m} = -r\epsilon_g \rho_g \frac{T_s - T}{T_s} \qquad \text{if} \quad T < T_s \quad \text{and} \quad \left|\nabla \epsilon_g\right| > 0. \tag{1.82}$$

The relaxation factor has to be tuned for each simulation.

Welch and Wilson [79], too, assumed that the interface temperature is at the saturation temperature of the pressure of the liquid phase. They developed a numerical VOF method, which calculates the heat flux vectors ($\vec{q}$) on both sides of the interface, considering the jump term of the mass conservation equation (Eq. 1.83). The difference between the velocity and the velocity vector ($\vec{v}_s$), which points towards the normal vector of the interface ($\vec{n}$) is calculated from the heat flux at the interface:

$$\|\vec{v} - \vec{v}_s\| = \left(\frac{1}{\rho_l} - \frac{1}{\rho_g}\right) \frac{\|\vec{q}\|\,\vec{n}}{h_{lv}}. \tag{1.83}$$

The energy jump condition provides the mass transfer rate as function from the difference of both heat fluxes.

Sato and Ničeno [80] obtained the interfacial mass transfer rate ($\dot{M}$) directly from the heat flux balance equation (Eq. 1.84) with the in-house CFD code PSI-BOIL:

$$\dot{M} = \frac{q_l + q_g}{h_{lv}}. \tag{1.84}$$

The heat flux of the gas and liquid phase was calculated from the temperature gradient at the liquid and the vapor side (Eq. 1.85):

$$q_l = \lambda_l \left(\nabla T_l\right) \vec{n} \quad \text{and} \quad q_g = -\lambda_g \left(\nabla T_g\right) \vec{n}. \tag{1.85}$$

The volumetric mass transfer rate ($\dot{m}$) is resulted from multiplying the above expression with the interface area density (Eq. 1.86), *i.e.* the cell volume (V_{cell}) divided by the area of the liquid–vapor interface in the cell (S_{int}):

$$\dot{m} = \dot{M} \frac{S_{int}}{V_{cell}}. \tag{1.86}$$

Nichita [81] and Ganapathy *et al.* [82] implemented the above equations in the FLUENT VOF method, considering an equal temperature gradient on the gas and liquid side. The

interfacial area density was equal to the gradient of the void fraction (Eq. 1.87):

$$\dot{m} = \frac{\left(\lambda_l \epsilon_l + \lambda_g \epsilon_g\right)\left(\nabla T \nabla \epsilon_l\right)}{h_{lv}}. \tag{1.87}$$

Sun *et at.* [83] implemented a modification of the above heat balance equation into the FLUENT VOF method. They assumed that the vapor is at saturation temperature, and the heat transfer coefficient of the gas phase is zero (Eq. 1.88):

$$\dot{m} = \frac{2\lambda_l \left(\nabla \epsilon_l \cdot \nabla T\right)}{h_{lv}}. \tag{1.88}$$

Badillo developed a general model to investigate boiling mass transfer based on a phase field theory [84]. He applied the model for bubble growth under convective conditions, achieving good comparison with experiments [85]. More details on the approach are provided in Chapter 3.

Table 1.2 shows the reviewed papers, grouped into categories according to the applied phase transition model, the applied CFD software and multiphase method.

Table 1.2: Modeling strategies for phase change phenomena - literature review

1. Semi-empirical correlations				
a) surface renewal	CFX	two-fluid model	condensation	[71] [69]
	NEPTUNE_CFD	two-fluid model	condensation	[69] [66] [86]
	CFX	VOF	condensation	[72]
b) surface divergence (Eq. 1.76)	TransAT	level set	condensation	[75]
2. Gas kinetic theory				
a) Eq. 1.78	n.i.*	VOF	condensation	[76]
	OpenFOAM	VOF	boiling	[87]
	FLUENT	VOF	boiling	[88][89]
3. Numerical iteration technique				
a) Lee	FLUENT	VOF	condensation	[90][77] [91][92]
4. Heat flux balance				
a) As it is (Eq. 1.85)	PSI-BOIL		boiling	[80]
	n.i.	VOF	condensation	[93]
	OpenFOAM	VOF	boiling	[94][95]
b) equal T gradient (Eq. 1.87)	FLUENT	LS + VOF	boiling	[81]
	FLUENT	VOF	boiling	[82]
c) (Eq. 1.88)	FLUENT	VOF	boiling	[83]
5. Phase field model	PSI-BOIL		boiling	[85]

* : n.i. = no information

While the articles introduced in the review report convincing results for the investigated phenomena, all approaches have limitations. The method of obtaining the mass transfer from the heat flux balance requires a fine mesh at the interface, which resolves the thermal

boundary layer. The equal temperature gradient in the two phases is not realistic, as the jump condition has to be respected and the thermal conductivities of both phases differ. The VOF method has only one temperature field in the domain, consequently, the implementation of the two temperature gradients is not straightforward.

The kinetic theory based models lack the resolution of the interfacial region, and the condensing coefficient used in these equations is arbitrary. The assumptions of the kinetic theory are not applicable on the scale of the VOF method. The numerical iteration technique provides good results through many iterations. Nonetheless, the optimal relaxation factor changes for each simulation; as too high value will cause convergence difficulties, too low values will not achieve convergence reaching saturation temperature at the interface.

The empirical techniques rely on the turbulent properties at the interface, which is difficult to resolve. Furthermore, the initial condition, *i.e.* the steam energy equation is not solved because the steam stays at saturation temperature, cannot be provided in the VOF method, as only one energy equation is solved for the two phases.

The conclusions of the literature review is used later in this thesis to develop the modeling strategy for condensation in horizontal pipes for the FLUENT VOF method (Chapter 3).

1.4 Experimental facilities used for code validation

The validation of the condensation heat transfer models for both RELAP5 and FLUENT is provided in this thesis. This section introduces the experimental facilities, which were used for code validation.

Section 1.4.1 describes the Invert Edward Pipe Experiment (INVEP), which was built to analyse a highly transient condensation process in an inclined horizontal pipe [96]. The experiment was simulated with the RELAP5 code.

The LAOKOON facility was chosen to validate the CFD models, as the two-dimensional steady flow field and the direct contact condensation makes the experiment suitable for sensitivity studies (Section 1.4.2).

The COSMEA (condensation test rig for flow morphology and heat transfer studies) experiment is introduced in Section 1.4.3. The experiment analyzed the geometry and heat transfer of the gas–liquid interface during condensation in a slightly inclined horizontal pipe. The facility was designed such that the pipe diameter and the flow conditions corresponded to the conditions in the emergency core cooling system of the KERENA reactor (Section 1.1). The experiment was simulated with both RELAP5 and FLUENT.

The results on the one-dimensional and three-dimensional investigation of the experimental facilities are presented in the later chapters (Chapter 4 and Chapter 5).

1.4.1 The Invert Edward Pipe Experiment

Böttger *et al.* [96] did transient condensation experiments to test novel local void probes that are combined with a micro-thermocouple. The provided data are suitable for model validation of thermal hydraulic codes as well. During the experiment hot steam entered the nearly horizontal pipe with a closed end, which lied in a basin of cold water, therefore the vapor condensed rapidly on the cold pipe wall. The well-known Edward's pipe experiment consisted of a very rapid depressurization of a hot pressurized water inventory in a pipe [97]. Because the experiments of Böttger *et al.* followed a reverse scenario, *i.e.* an empty pipe was suddenly pressurized, it was humorously called INVEP by the authors [98].

The experimental setup (Fig. 1.9) contained a condensation pipe, which was immersed into a cooling water tank (6300 × 1000 × 400 mm). The heat exchanger pipe had an inclination of −1.56°, a length of 5.675 m, and an inner diameter of 44.3 mm. The pipe was made of stainless steel and the wall thickness was 2 mm. The cooling tank was big enough to keep the water temperature nearly constant during the experiment (about 300 K). The pipe inlet was connected to a steam dome of a pressurizer, filled with high pressure saturated water–steam mixture. The rear side of the pipe was closed.

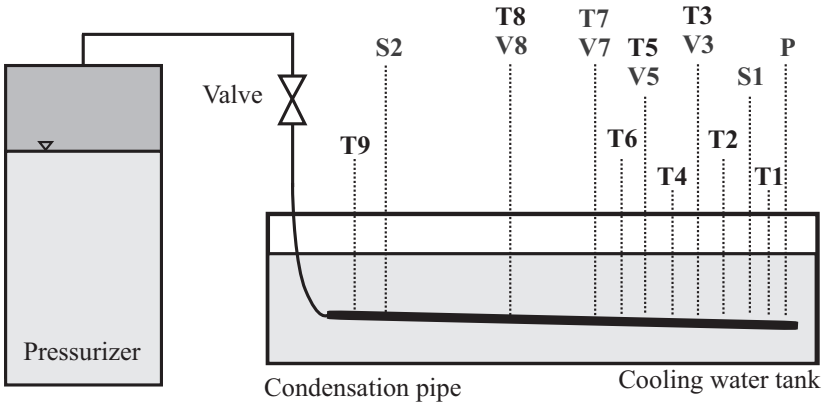

Figure 1.9: The INVEP experimental setup

The pipe was equipped with local void probes and micro-thermocouples. Twelve locations inside the tube contained temperature, void fraction or pressure measurements (Fig. 1.9 and Table 1.3).

With the impedance measurement probes (VT3, VT5, VT7 and VT8), the liquid phase was detected by sampling the electrical current from the electrode wire of the needle-shaped probe, which was the shroud of a micro-thermocouple of 0.25 mm diameter. Consequently, the temperature and the void fraction were measured at the same location. Additionally, two normal void probes (S1, S2) without thermocouple and three traditional thermocouples (T1, T2 and T9) were used. The sensitive tip of each probe was in the center of the condensation pipe cross section. Pressure transducers measured the pressure in the pressurizer and at the closed end of the condensation pipe. The probes recorded the data with 500 Hz frequency.

Table 1.3: Locations of the instrumentation inside the INVEP condensation pipe

name	parameter	position [mm]	name	parameter	position** [mm]
P^*_{pi}	pressure	85	P_{pr}	pressure	3355
$T1$	temp	140	$S1$	void	620
$T2$	temp	1100	$T3$, $V3$	temp, void	1580
$T4$	temp	2060	$T5$, $V5$	temp, void	2535
$T6$	temp	3015	$T7$, $V7$	temp, void	3490
$T9$	temp	5550	$T8$, $V8$	temp, void	4655
			$S2$	void	5525

* P_{pi}: pressure in the pipe, P_{pr}: pressure in the pressurizer
** the position is the distance from the closed end of the pipe

Twenty-four experiments were done with different initial pressures in the pressurizer and in the pipe (Table 1.4). An initial equilibrium of the temperatures in the pipe and the cooling tank was established before the start of each test. The experiment started with opening the valve between the pressurizer and the pipe; after steam entered the pipe. The rapid steam ingress caused a pressure increase and produced an abrupt condensation. The measurement stopped when the pipe was filled with liquid.

Table 1.4: Initial condition of the INVEP experiments

P_{pi} / P_{pr} (bars)	10	30	50	70
0*	A07	B07	C11	D07
1	A05	B05	C10	D06
3	–	B03	C08	D05
5	–	–	C05	D04
7	–	–	–	D03
10	–	–	C07	D02

* The zero bar means that the pipe was evacuated, having 95% technical vacuum.

In this thesis, the simulation of the INVEP experimental setup with the RELAP5 and TRACE one-dimensional system codes is presented. The results of the code validation for transient condensation process are discussed in Chapter 4.

1.4.2 The LAOKOON test facility

Goldbrunner *et al.* [99] built an experimental setup at the Technische Universität München to measure direct contact condensation on a subcooled water surface. Figure 1.10 shows the experimental setup. The laser beam was used to measure the nitrogen profile from Raman emission.

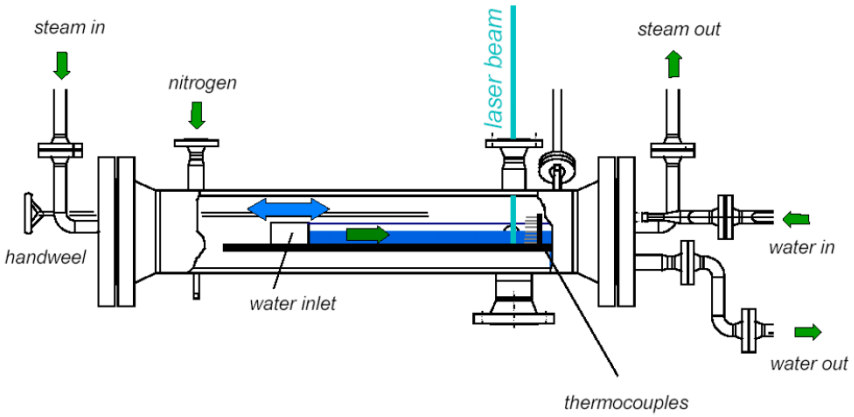

Figure 1.10: The LAOKOON experimental setup [99]

The rectangular open channel had two separate inlets for the liquid and for the vapor phase. The precise inlet and outlet conditions ensured the horizontal liquid surface in the channel. A thermocouple line, consisting of 12 thermocouples, measured the temperature along a vertical line. Experiments were done with and without non-condensable gas in the vapor phase. In the current CFD simulations the focus is on the condensation of pure steam. The experimental setup provided data about the water and steam flow rates at the feed cross section, the inlet water temperature, the temperature distribution along the thermocouple line, the pressure level in the channel, and the water height (Table 1.5).

Table 1.5: Parameters of the LAOKOON experiment

Inlet velocity of water [m/s]	0.28
Inlet velocity of steam [m/s]	3.20
Pressure [bar]	6.97
Inlet water temperature [K]	300.2
Saturation temperature [K]	437.93
Mean water temperature at the probe [K]	324.43
Height of the water level [mm]	31
Steam velocity at the measurement station [m/s]	1.94
Water Reynolds number	28'082
Steam Reynolds number at the inlet	51'051

Measurements confirmed that the flow in the duct was two-dimensional, with negligible influence of the walls [70]. The condensation caused a significant breaking of the steam velocity; however, the acceleration of the liquid phase was negligible due to the high density ratio. The latent heat of the condensation heated up the initially subcooled water. The condensation rate was limited by the heat transfer from the free surface to the bulk water flow.

Table 1.6 shows the temperature data along the thermocouple line at the measurement line.

The LAOKOON experimental setup was used to validate CFD codes for direct contact condensation in the past. The phenomenon occurs in pressurized thermal shock scenarios in nuclear power plants, when the emergency core cooling system injects cold water into the cold leg, and the saturated steam condenses on the subcooled water surface [100]. The LAOKOON experiments were calculated by the NEPTUNE_CFD and the CFX-5 codes in the European ECORA project [69]. The project was followed by the NURESIM project [70], where the experiment was simulated by the ANSYS CFX software [71]. The results from these studies are presented in Chapter 5.

Table 1.6: Temperature data of the thermocouple line - LAOKOON experiment

y (m)	T (K)
0.004	310.94
0.008	310.48
0.012	311.31
0.016	313.14
0.02	316.42
0.024	322.26
0.026	331.79
0.028	354.73
0.03	411.97
0.031	435.67
0.034	434.77
0.036	435.74

1.4.3 The COSMEA facility

Geißler *et al.* [101] did experiments in the TOPFLOW facility (Helmholtz-Zentrum Dresden-Rossendorf) to measure steady state condensation heat transfer in an inclined pipe. The facility aimed to study condensation as a single effect, corresponding to the conditions of the KERENA reactor emergency cooling system. The geometry of the pipe, and the fluid conditions were taken from the KERENA emergency condenser studies.

The experimental setup consisted of an annular pipe system (Fig. 1.11). At the primary side inlet, water–steam mixture entered at saturation condition of the corresponding pressure. The steam condensed on the colder walls, and flowed downwards due to the inclined position of the pipe. The outlet was connected to a separation tank. The secondary side ensured the cooling of the condensation pipe wall by circulating cold water.

The experimental setup was equipped with thermocouples, flow meters and pressure transducers on both sides (Table 1.7). An X-ray tomography system recorded the steam–water distribution at five positions in the primary side. The images were recorded in 3.3 minutes; therefore, fluctuations, slug, plug formations were averaged out. The height of

the water flume at the bottom of the pipe was derived from the tomography images, the achieved resolution was not able to detect the water film thickness at the upper part of the pipe.

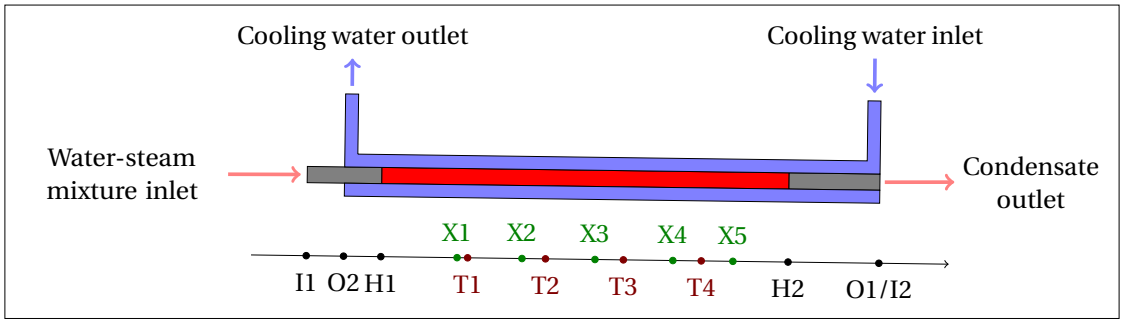

Figure 1.11: Scheme of the COSMEA experiment with the measurement points

The secondary side consisted of 15 thermocouples and four swirl generators to ensure the turbulent cooling of the pipe wall. The pressure and the mass flow of the secondary side was measured and controlled by the thermocouples such, that the temperature and the pressure of the secondary side was constant.

Table 1.7: Measurement points in the COSMEA facility

name	Description	Position	Side
I1	Steam–water mixture inlet (P, $\dot{m}$, T meas.)	−460 mm	Primary
O2	Cooling water outlet (T meas.)	−230 mm	Secondary
H1	Begin of un-isolated part	0mm	Primary
X1	X-ray tomography	470 mm	Primary
T1	Temperature measurement	535 mm	Secondary
X2	X-ray tomography	870 mm	Primary
T2	Temperature measurement	1015 mm	Secondary
X3	X-ray tomography	1320 mm	Primary
T3	Temperature measurement	1495 mm	Secondary
X4	X-ray tomography	1800 mm	Primary
T4	Temperature and heat flux measurement	1975 mm	Both
X5	X-ray tomography	2170 mm	Primary
H2	End of un-isolated part	2510 mm	Primary
I2	Cooling water inlet (P, $\dot{m}$, T meas.)	3070 mm	Secondary
O1	SW mixture outlet (P, T meas.)	3070 mm	Primary

The thermocouples in the secondary side detected the cooling water temperature axially in four positions. At one of this positions (T4), the azimuthal and radial temperature distribution was recorded as well. An additional heat flux probe was installed here, which measured the inner and outer wall temperature of the condensation pipe at five azimuthal positions (Fig. 1.12).

The inlet conditions for the primary side were set by two pressure transducers and flow meters. The initial flow pattern of the two phase, the annular flow regime, was ensured by a flow straightener and a ring injection system at the water inlet (the ring was 0.5 mm thick). The inlet was followed by a 460 mm long adiabatic section, which ensured the fully developed flow pattern at the inlet of the condensation section. The 2510 mm long condensation part is followed by a 560 mm long outlet adiabatic part. The outlet pressure of the condensation pipe was the pressure of the separation tank, where the temperature was recorded as well.

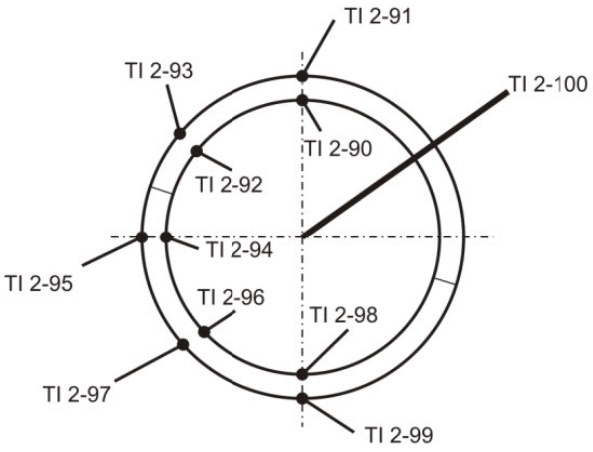

Figure 1.12: The location of the heat flux probes at the T4 position. The thermocouple names are the indexes from the report of Geißler *et al.* [101].

The outer diameter of the condensation pipe was 48.3 mm, 2.5 mm was the wall thickness and 0.76° was the inclination of the pipe. The separation tank had a diameter of 550 mm. The secondary side pipe had an inner diameter of 110.4 mm. The pipe was made of stainless steel.

The conditions for the 23 experiments (Table 1.8) had similar values to the KERENA emergency condenser system. The pressure varied between 5-65 bars in the primary side. The void fraction varied between 0-1 for all the pressure values, while the total mass fraction was kept constant for the corresponding pressure. The only exceptions were the 5 bars experiments, where the lower void fraction required a higher mass flow. The mean temperature of the cooling water was kept constant (313 K for the pressures 5-45 bars, 315 K for the 65 bars experiments) during the measurements. The secondary side temperature increased 3 K from the inlet to the outlet for low pressures (5 and 15 bars), and 5 K for higher pressures.

The Appendix contains the detailed measurement data for the experiment series. The thermocouples had an uncertainty of 0.3 K, the pressure measurement obtained 1%, the flow meters 3% error. The heat flux probe had an uncertainty of 8%.

The radial and azimuthal temperature measurements indicated that the temperature fluctuation at the secondary side is in a range of 0.5–2 K.

Table 1.8: Measurement matrix for the COSMEA facility

No.	P_{pr} [bar]	ϵ_{pr}	$\dot{m}_{total}$ [kg/s]	$\dot{m}_v$ [kg/s]	$\dot{m}_w$ [kg/s]	No.	P_{pr} [bar]	ϵ_{pr}	$\dot{m}_{total}$ [kg/s]	$\dot{m}_v$ [kg/s]	$\dot{m}_w$ [kg/s]
51	5	1	0.088	0.088	0	**451**	45	1	0.610	0.610	0
52		0.63	0.130	0.064	0.042	**452**		0.85	0.610	0.520	0.09
151	15	1	0.255	0.255	0	**453**		0.70	0.610	0.429	0.181
152		0.80	0.255	0.204	0.051	**454**		0.56	0.610	0.339	0.271
153		0.60	0.255	0.153	0.102	**455**		0.41	0.610	0.248	0.362
154		0.40	0.255	0.102	0.153	**456**		0.33	0.610	0.203	0.406
251	25	1	0.406	0.406	0	**651**	65	1	0.800	0.800	0
252		0.83	0.406	0.336	0.07	**652**		0.85	0.800	0.678	0.122
253		0.66	0.406	0.266	0.14	**653**		0.70	0.800	0.556	0.244
254		0.48	0.406	0.196	0.21	**654**		0.54	0.800	0.434	0.366
255		0.31	0.406	0.125	0.281	**655**		0.43	0.800	0.340	0.470
						656		0.31	0.800	0.245	0.555

The flume height determined from the X-ray tomography images had an uncertainty of 0.5 mm. The liquid film at the wall was not detected.

Table 1.9 shows the material properties for the experiments. The properties were calculated for the saturation condition for all the pressures.

Table 1.9: Material properties for the experiments

	Water	Steam	Water	Steam	Water	Steam
P [bars]	5.05		15.1		25.2	
T_s [K]	425.36		471.76		497.53	
ρ [kg/m^3]	914.93	2.693	866.28	7.6417	834.56	12.607
C_p [J/kgK]	4316.07	2416.14	4487.05	2969.1	4641.04	3412.83
λ [W/mK]	0.68165	0.03192	0.66413	0.0398	0.6461	0.04511
μ [kg/ms]	0.0001796	1.406E-5	0.000135	1.566E-5	0.0001190	1.656E-5
C_p [kJ/kg]	641.80	2748.55	846.1359	2791.208	963.955	2802.132
	Water	Steam	Water	Steam		
P [bars]	45.4		65.4			
T_s [K]	531.12		554.41			
ρ [kg/m^3]	786.77	22.907	748.016	33.8671		
C_p [J/kgK]	4955.717	4244.55	5309.5	5128.8		
λ [W/mK]	0.61154	0.053449	0.57796	0.06109		
μ [kg/ms]	0.0001025	1.7796E-5	9.301E-5	1.875E-5		
C_p [kJ/kg]	1124.812	2797.725	1243.311	2778.346		

2 Mechanistic model development for the RELAP5 code

The RELAP5 thermal hydraulic code was used for pre-test calculations of the INKA facility [7], [8], [9]. The comparison of the post-test calculations and experimental results showed that RELAP5 correctly captured the important phenomena in the emergency condensers; furthermore, it could reproduce the heat transfer from the emergency core cooling system to the containment pool [8]. Further proposals were made for test specification, based on integral pre-test calculations of the INKA Experiments [9].

However, the stratified flow, which occurs in the emergency condenser, is not well reproduced in the RELAP5 calculations. The Chato correlation, which is used to calculate the heat transfer coefficient in horizontal pipes, does not allow the consideration of local void fraction values and flow patterns. To overcome these limitations, I implemented a mechanistic model into the RELAP5/mod3.3 code to calculate the condensation heat transfer coefficient in horizontal or slightly inclined pipes. This chapter presents the model development.

The model uses the local void fraction in the pipe as input quantity, and it assumes that stratified flow occurs for the conditions of the emergency core cooling system of the KERENA reactor [34] [35]. To characterize the flow pattern, the calculation considered a cross section of a slightly inclined horizontal pipe. It was coded in MATLAB for testing purposes before the implementation into RELAP5.

The model divided the flow pattern into three parts: vapor core in the middle of the pipe, thin liquid film on the upper wall, and condensate flume at the bottom of the pipe cross section. The model assumed a laminar film condensation process in the upper part, a turbulent axial flow in the bottom part, and it calculated heat transfer coefficients and wall temperatures for both sections independently. The output of the calculation provided both heat transfer coefficients, the condensate film thicknesses and the inner pipe wall temperatures. Based on these values, the average heat transfer coefficient was calculated for the entire cross section.

The program had the following main functions:

- input parameters, calculation of the liquid and vapor properties (Section 2.1);

- determination of the flow pattern (Section 2.2);
- estimation of the heat transfer of the axial flume (Section 2.3);
- estimation of the heat transfer of the condensate film (Section 2.4);
- calculation of the inner wall temperature (Section 2.5);
- calculation of the average heat transfer coefficient for the cross section (Section 2.6);
- displaying the results (Section 2.7).

2.1 Input parameters

The input parameters include geometrical data (radius (R), wall thickness, length of the pipe (L), slide thickness, inclination angle(θ)) and flow parameters (incoming mass flow (W), void fraction (ϵ), pressure (P), secondary side temperature (T_{out})).

The liquid (l), vapor (v) and the wall material properties were calculated by the program according to the pressure and the temperature inputs. The gas phase is indicated as vapor in this chapter, because non-condensable gas effects are not considered, *i.e.* the gas phase contains only the vapor of the liquid. Table 2.1 shows the constant parameters, which were used in the program.

The saturation temperature at the corresponding pressure, and the phasic properties were estimated using the IAPWS-97 tables [102]. The fluids were considered at saturation condition. The fluid property values were plotted against the pressure in range of 1–100 bars. Either polynomial fitting (Eq. 2.1) or an exponential function (Eq. 2.2) was applied to acquire the relation between the corresponding property and the pressure (e.g. Fig. 2.1). The exponential curve was used when the polynomial fitting did not obtain good results:

$$y(P) = A + B1 \cdot P + B2 \cdot P^2 + B3 \cdot P^3, \tag{2.1}$$

$$y(P) = a \cdot x^b. \tag{2.2}$$

Table 2.2 shows the fitted parameters (A, B1, B2, B3 or a, b) for each fluid property.

The thermal diffusivity (Eq. 2.3), the kinematic viscosity (Eq. 2.4) and the Prandtl number (Eq. 2.5) were calculated from the fluid properties (Table 2.2):

$$a = \frac{\lambda_l}{C_{pl} \cdot \rho_l}, \tag{2.3}$$

$$v_l = \frac{\mu_l}{\rho_l}, \tag{2.4}$$

$$\mathrm{Pr} = \frac{v_l}{a}. \tag{2.5}$$

Table 2.1: Constant parameters in the MATLAB calculation

	Description	**Value**
Pr_t	Turbulent Prandtl number	0.9
g [m/s^2]	Gravitational constant	9.81
λ_0 [W/mK]	Thermal conductivity for $T_0 = 0K$	11.45649
β [1/K]	Temperature coefficient	0.001127

Table 2.2: Parameters used for the calculation of the liquid and vapor properties

	Description	**A**	**B1**	**B2**	**B3**
C_{pl} [J/kgK]	Water specific heat	4.205	0.022	$-2.49e{-4}$	$3.5e{-06}$
h_{lv} [J/kg]	Latent heat	2252.7	-28.766	$6.58e{-1}$	$8.2e{-03}$
λ_l [W/mK]	Thermal cond.	0.6853	$-7.48e{-4}$	$-5.09e{-5}$	$8.2e{-07}$
μ_v [kg/ms]	Vapor viscosity	$1.26e{-5}$	$2.95e{-7}$	$-7.16e{-9}$	$8.6e{-11}$
ρ_l [kg/m^3]	Density of liquid	958.1	-8.556	$1.94e{-1}$	$-2.4e{-03}$
ρ_v [kg/m^3]	Density of vapor	0.130	0.507	$-9.00e{-4}$	$2.0e{-05}$
σ [N/m]	Surface tension	58.38	-1.979	$4.93e{-2}$	$-6.0e{-04}$
		a		**b**	
μ_l [kg/ms]	Liquid viscosity	2.79e-04		-0.265	
T_s [K]	Saturation temp.	102.57		0.241	

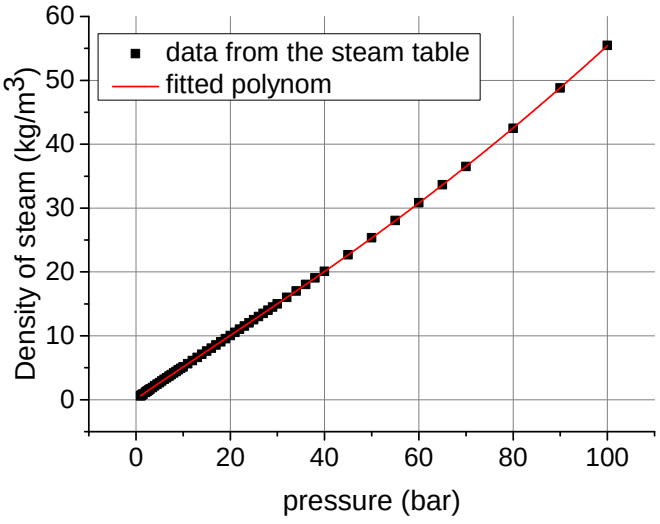

Figure 2.1: Saturated steam density as a function of the pressure

The initial guess for the inner wall temperature is calculated as the average of the saturation temperature and the outer wall temperature (Eq. 2.6):

$$T_w^0 = \frac{T_{out} + T_s}{2}. \tag{2.6}$$

The homogeneous flow model [16] was applied to calculate the mass quality (Eq. 2.7):

$$X_m = \frac{1}{1 + \frac{1-\epsilon}{\epsilon} \cdot \frac{\rho_l}{\rho_v}}. \tag{2.7}$$

The wall thermal conductivity is linear with the temperature (Eq. 2.8):

$$\lambda_w = \lambda_0 \left(1 + \beta T\right). \tag{2.8}$$

The outer surface heat transfer coefficient is a constant input parameter of the calculation.

2.2 Determination of the flow pattern

The next step after defining the input parameters is to calculate the flow pattern from the void fraction. The flow pattern is determined by the following parameters: stratification angle (Φ_{strat}), film thickness of the upper part (δ_f), thickness of the flume (δ_b) (Fig. 2.2).

Figure 2.2.a shows a fully developed stratified flow in horizontal pipes. The equivalent geometry (Fig. 2.2.b) was defined, with the same stratification angle, but the bottom flow is considered with a uniform film thickness [48], [49]. Figure 2.2.c shows the assumed flow pattern, if the void fraction is below 0.5; consequently, the stratification angle is smaller than 180°.

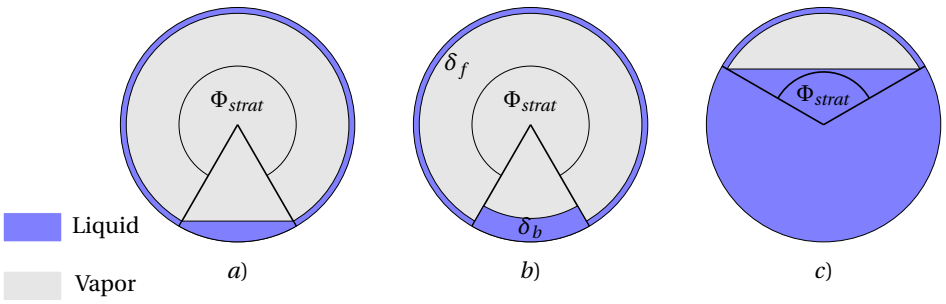

Figure 2.2: Stratified flow pattern in horizontal pipes

The stratification angle can be estimated by an explicit formula (Eq. 2.9), if the laminar film thickness is negligible comparing to the bottom liquid flow thickness [103]. The stratification angle is estimated by replacing the void fraction with the liquid fraction in the equation, if

the void fraction is smaller than 0.5:

$$\Phi_{strat} = 2\pi - 2\pi(1-\epsilon) + 2(3\pi/\epsilon)^{1/3}\left[1-2(1-\epsilon)+(1-\epsilon)^{1/3}-\epsilon^{1/3}\right] - \frac{2}{200}(1-\epsilon)\epsilon\left[1-2(1-\epsilon)\right]\left[1+4\left((1-\epsilon)^2+\epsilon^2\right)\right]. \quad (2.9)$$

Thome *et al.* [49] calculated the flow pattern, assuming that the liquid cross section is equal to the the axial flow area. I used an iteration to refine the stratification angle with the area occupied by the laminar condensate film at the upper part.

If the stratification angle (Eq. 2.9) and the film thickness are determined (see Section 2.4), the liquid cross section is calculated in two ways. The sum of the liquid area of the upper part (Eq. 2.10) and of the bottom part (Eq. 2.11) is the liquid cross section for the pipe (Eq. 2.12), and the result is compared to the definition of the void fraction (Eq. 2.13):

$$A_l^{up} = \frac{\left(2R\delta_f - \delta_f^2\right)\Phi_{strat}}{2}, \quad (2.10)$$

$$A_l^{bottom} = \begin{cases} R^2\left[\pi - \dfrac{\Phi_{strat} - \sin(\Phi_{strat})}{2}\right] & \text{if} \quad \epsilon > 0.5 \\ \dfrac{R^2}{2}\left[(2\pi - \Phi_{strat}) - \sin(2\pi - \Phi_{strat})\right] & \text{if} \quad \epsilon \le 0.5, \end{cases} \quad (2.11)$$

$$A_l^{calc} = A_l^{bottom} + A_l^{up}, \quad (2.12)$$

$$A_l = A(1-\epsilon) = R^2\pi\cdot(1-\epsilon). \quad (2.13)$$

The stratification angle is accepted if the difference between the two values is smaller than 0.001%. Otherwise, the stratification angle is tuned, until the two cross section calculation obtains the same value.

The thickness of the bottom axial liquid flow is calculated from geometrical considerations (Eq. 2.14):

$$\delta_b = \begin{cases} R - \left[R^2 - \dfrac{2A_l^{bottom}}{2\pi - \Phi_{strat}}\right]^{1/2} & \text{if} \quad \epsilon > 0.5 \\ R + R\cos(\Phi_{strat}/2) & \text{if} \quad \epsilon \le 0.5. \end{cases} \quad (2.14)$$

The outputs of the flow pattern calculation are the stratification angle and the axial flume thickness.

2.3 Estimation of the heat transfer of the axial flume

The heat transfer of the bottom axial flume and the upper laminar film is calculated independently. This section describes the heat transfer coefficient calculation for the bottom part. Chitti *et al.* [38] calculated axial annular flow heat transfer in horizontal pipes. I used the analogy of their derivation to calculate the axial bottom flume.

The input parameters of the calculation are the flow pattern geometry and the fluid properties described in Section 2.1. The flow direction (x) is the direction of the horizontal pipe, a slide of the cross section (Δx) is considered in the calculation, which acts as a calculation node (Fig. 2.3).

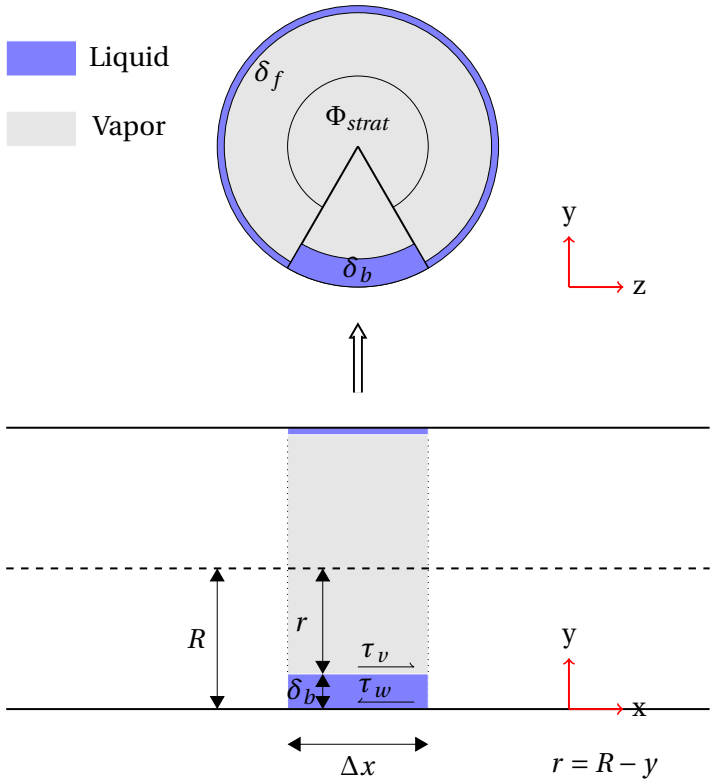

Figure 2.3: The axial flume flow

The following assumptions are considered for the bottom flow:

- steady, turbulent flow, characterized by the axial velocity component, whereas turbulent length scale is considered from the Von-Karman theory;
- The thickness of the liquid film is uniform (Fig. 2.3); consequently, the flow is one-dimensional;
- The liquid properties are constant in the liquid film;
- The liquid subcooling is negligible;
- The vapor is at saturation temperature;
- The gravitational effect is negligible;

- The bottom flume thickness is uniform in the corresponding computational node.

The aim of the calculation is the heat transfer coefficient of the bottom axial flow. The definition of the heat transfer coefficient (Eq. 2.15) is reformulated (T_δ is the temperature at the liquid vapor interface) by substituting the non-dimensional velocity (Eq. 2.16), coordinate (Eq. 2.17) and temperature (Eq. 2.18) parameters:

$$\alpha_b = \frac{q_w}{T_w - T_\delta}, \tag{2.15}$$

$$u^+ = \frac{u}{u^*} = \frac{u}{\sqrt{\tau_w/\rho_l}}, \tag{2.16}$$

$$y^+ = \frac{y u^*}{v_l} = \frac{y\sqrt{\tau_w/\rho_l}}{v_l}, \tag{2.17}$$

$$T^+ = \frac{(T_w - T)\, u^*}{\left(q_w/\left(\rho_l C_{pl}\right)\right)}. \tag{2.18}$$

The result (Eq. 2.19) contains the non-dimensional temperature at the liquid–vapor surface (T_δ^+) and the friction velocity (u^*):

$$\alpha_b = \frac{\rho_l C_{pl} u^*}{T_\delta^+}. \tag{2.19}$$

The non-dimensional temperature is obtained from the heat governing equation (Eq. 2.20), which is expressed by the heat eddy diffusivity (ϵ_h):

$$q = -\left(\lambda_l + \rho_l C_{pl} \epsilon_h\right) \frac{\mathrm{d}T}{\mathrm{d}y}. \tag{2.20}$$

The heat conduction is uniform along the liquid layer, the heat is transferred in the radial direction. Consequently, the vertical coordinate is used (y). The non-dimensional form of the equation (Eq. 2.21) is a differential equation containing the Prandtl ($\mathrm{Pr} = \mu C_p/\lambda$) and the turbulent Prandtl numbers:

$$\frac{q}{q_w} = \left(\frac{1}{\mathrm{Pr}} + \frac{1}{\mathrm{Pr}_t}\left[\frac{\epsilon_m}{v_l}\right]\right) \frac{\mathrm{d}T^+}{\mathrm{d}y^+}. \tag{2.21}$$

The turbulent Prandtl number is calculated as a ratio between the momentum and heat eddy diffusivity ($\mathrm{Pr}_t = \epsilon_m/\epsilon_h$). The governing equation is solved for the temperature (Eq. 2.22), the integral is solved from the film surface (δ_b^+) until the wall (0), *i.e.* through the liquid layer:

$$T_\delta^+ = \int_{\delta_b^+}^{0} \left(\frac{q/q_w}{\frac{1}{\mathrm{Pr}} + \frac{1}{\mathrm{Pr}_t}\left[\frac{\epsilon_m}{v_l}\right]} \mathrm{d}y^+ \right). \tag{2.22}$$

The heat transfer coefficient (Eq. 2.19) is determined by the following expressions:

- the non-dimensional film thickness (δ_b^+);
- the friction velocity (u^*);
- the heat flux ratio (q/q_w) in terms of the non-dimensional coordinate (y^+);
- the ratio of the momentum eddy diffusivity and the kinematic viscosity (ϵ_m/υ_l) in terms of the non-dimensional vertical coordinate (y^+).

The non-dimensional liquid layer thickness is calculated by Eq.2.17 using the flume thickness from the flow pattern calculation. In the followings, the calculation of the other three terms is presented.

The friction velocity

The friction velocity is the characteristic velocity at the wall, which is defined with the wall shear stress and the liquid density (Eq. 2.23):

$$u^* = (\tau_w/\rho_l)^{1/2}. \tag{2.23}$$

The wall shear stress is obtained from the force balance equation at the wall. The two phase friction (TPF) forces act on the fluid element with an axial length dx (Eq. 2.24):

$$\tau_w 2R\pi = \left(\frac{\mathrm{d}P}{\mathrm{d}x}\right)_{\mathrm{TPF}} R^2\pi. \tag{2.24}$$

From the above equation, the wall shear stress is calculated by the two-phase flow pressure drop (Eq. 2.25):

$$\tau_w = \left(\frac{\mathrm{d}P}{\mathrm{d}x}\right)_{\mathrm{TPF}} 2R. \tag{2.25}$$

The pressure drop is obtained by the Lockhart-Martinelli correlation, which is commonly used to calculate the pressure drop of two-phase flows in pipes [104]. The model assumes that the pressure loss of the two separate phases are independent. The phasic Lockhart-Martinelli parameters (Eq. 2.26) are defined as the ratio of the two-phase pressure drop and the corresponding single phase pressure drop:

$$\phi_{vv}^2 = \frac{\left(\frac{\mathrm{d}P}{\mathrm{d}x}\right)_{\mathrm{TPF}}}{\left(\frac{\mathrm{d}P}{\mathrm{d}x}\right)_v}. \tag{2.26}$$

The single phase pressure drop (Eq. 2.27) and the Lockhart-Martinelli parameter (Eq. 2.28, substituting Eq. 2.29) are determined by empirical correlations (W is the mass flow rate):

$$\left(\frac{\mathrm{d}P}{\mathrm{d}x}\right)_v = \frac{0.143\cdot\mu_v^{0.2}(W\cdot X_m)^{0.8}}{\rho_v(2R)^{4.8}}, \tag{2.27}$$

$$\phi_{vv} = 1 + 2.85\cdot X_{tt}^{0.523}, \tag{2.28}$$

$$X_{tt} = \left(\frac{\mu_l}{\mu_v}\right)^{0.1} \left(\frac{1-X_m}{X_m}\right)^{0.9} \left(\frac{\rho_v}{\rho_l}\right)^{0.5}. \tag{2.29}$$

The friction velocity (Eq. 2.24) is calculated by substituting the expression for the two-phase pressure drop (Eq. 2.30):

$$u^* = \left[\frac{R}{2\rho_l}\phi_{vv}^2 \left|\frac{\mathrm{d}P}{\mathrm{d}x}\right|_v\right]^{1/2}. \tag{2.30}$$

The heat transfer distribution

The heat transfer distribution is derived from the heat flux continuity in the radial direction (Eq. 2.31, L is the length):

$$q(2\pi rL) = q_w(2\pi RL). \tag{2.31}$$

The radial coordinate is transformed to the vertical coordinate ($r = R - y$), and the non-dimensional transformation is used to obtain the result (Eq. 2.32):

$$\frac{q}{q_w} = \frac{R}{r} = \frac{R}{R-y} = \frac{1}{1-y^+/R^+}. \tag{2.32}$$

The ratio of momentum eddy diffusivity and kinematic viscosity (ϵ_m/v_l)

The ratio of the momentum eddy diffusivity and the kinematic viscosity (ϵ_m/v_l) is calculated from the Prandtl's mixing length theory, applying the Van-Dreist't hypothesis [105].

The mixing length theory defines the mixing length (l) in a turbulent boundary layer. The mixing length is the maximum length, in which eddies travel perpendicular to the surface in the boundary layer, while the time averaged velocity of the flow remains constant [105]. Van Driest modified the model, considering a damping function in the viscous sublayer, which accounts for the eddy diffusivity [105]. The definition of the mixing length (Eq. 2.33) contains empirical constants, the Von Karman's constant ($\kappa = 0.4$) for pipes, and a dimensionless viscous sublayer thickness ($A^+ = 26.0$):

$$l = \kappa y^+ \left[1 - \frac{1}{\mathrm{e}^{y^+/A^+}}\right]. \tag{2.33}$$

The definition of the momentum eddy diffusivity (Eq. 2.34) is rearranged in the non-dimensional form by substituting the mixing length (Eq. 2.33, obtaining Eq. 2.35):

$$\epsilon_m = l^2 \left|\frac{\mathrm{d}u}{\mathrm{d}y}\right|, \tag{2.34}$$

$$\frac{\epsilon_m}{v_l} = \kappa^2 y^{+2} \left[1 - \frac{1}{e^{y^+/A^+}}\right]^2 \left|\frac{\mathrm{d}u^+}{\mathrm{d}y^+}\right|. \tag{2.35}$$

The velocity gradient is calculated from the Von-Karman velocity distribution (Eq. 2.36):

$$u^+ = \begin{cases} y^+ & \text{if} \quad 0 < y^+ < 5, \\ -3.05 + 5.0 \ln y^+ & \text{if} \quad 5 < y^+ < 30, \\ 5.5 + 2.5 \ln y^+ & \text{if} \quad 30 < y^+. \end{cases} \tag{2.36}$$

The final expression for the heat transfer coefficient

The substitution of the heat transfer distribution (Eq.2.31) and the ϵ_m/υ_l term (Eq.2.35) leads to the integral for the temperature (Eq. 2.22), where all the terms are known parameters. The three velocity groups are defined by the Von-Karman distribution, and the integrands depend on the thickness of the liquid layer (Eq. 2.38-2.40):

$$T_\delta^+ = \begin{cases} \int_{\delta_b^+}^{0} \mathrm{I}_1 & \text{if} \quad 0 < \delta_b^+ < 5, \\ \int_{5}^{0} \mathrm{I}_1 + \int_{\delta_b^+}^{5} \mathrm{I}_2 & \text{if} \quad 5 < \delta_b^+ < 30, \\ \int_{5}^{0} \mathrm{I}_1 + \int_{30}^{5} \mathrm{I}_2 + \int_{\delta_b^+}^{30} \mathrm{I}_3 & \text{if} \quad 30 < \delta_b^+, \end{cases} \tag{2.37}$$

$$\mathrm{I}_1(y^+) = \frac{1}{1 - \frac{y^+}{R^+}} \left(\frac{1}{\frac{1}{\mathrm{Pr}} + \frac{1}{\mathrm{Pr}_t} \kappa^2 \cdot y^{+2} \left[1 - \frac{1}{e^{y^+/A^+}} \right]^2} \right), \tag{2.38}$$

$$\mathrm{I}_2(y^+) = \frac{1}{1 - \frac{y^+}{R^+}} \left(\frac{1}{\frac{1}{\mathrm{Pr}} + \frac{5}{\mathrm{Pr}_t} \kappa^2 \cdot y^{+} \left[1 - \frac{1}{e^{y^+/A^+}} \right]^2} \right), \tag{2.39}$$

$$\mathrm{I}_3(y^+) = \frac{1}{1 - \frac{y^+}{R^+}} \left(\frac{1}{\frac{1}{\mathrm{Pr}} + \frac{2.5}{\mathrm{Pr}_t} \kappa^2 \cdot y^{+} \left[1 - \frac{1}{e^{y^+/A^+}} \right]^2} \right). \tag{2.40}$$

The calculation of the friction velocity (Eq.2.30) and the non-dimensional temperature at the liquid–vapor interface obtains the heat transfer coefficient for the bottom part of the pipe:

$$\alpha_b = \frac{\rho_l C_{pl} u^*}{T_\delta^+}.$$

The heat transfer is neglected in the code, if the void fraction is smaller than 0.5.

2.4 Estimation of the heat transfer of the condensate film

The heat transfer coefficient of the upper laminar film layer is calculated independently from the bottom part heat transfer. The Nusselt's theory of laminar film condensation on vertical walls was applied [16]. The theory considers the condensate as downwards flow, on

which the gravity force acts, and condensate is added to the flow at the vapor–liquid surface.

The Nusselt theory divides the flow into fluid elements. The analogy was applied for the stratified flow; Figure 2.4 shows the fluid element of the upper laminar film.

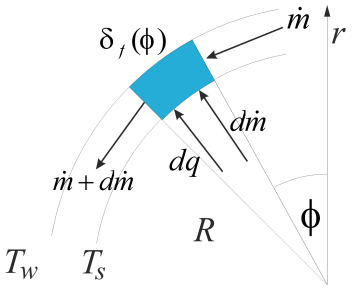

Figure 2.4: Scheme of the falling laminar condensate film. The incoming mass flow has two components, the condensation mass flow (d$\dot{m}$), and the mass flow from the falling film ($\dot{m}$). The local heat flux (dq) is constant through the film, which has saturation temperature at the surface (T_s), and the wall temperature is T_w. The local liquid film thickness (δ_f) is a function of the angular coordinate (ϕ).

The following assumptions were considered for the film condensation in horizontal pipes and for the two-dimensional fluid element:

- the flow is laminar and the thermal profile is fully developed, linear across the film; consequently, one-dimensional heat conductivity applies through the liquid film to the wall,
- the vapor temperature is uniform and at saturation temperature;
- the liquid properties in the film are constant, *i.e.* they do not vary with the temperature;
- the film thickness is negligible compared to the radius; therefore, the fluid element considered as an element of an inclined vertical wall. Hence, the area of the fluid element at the vapor–liquid interface and the wall is equal to $R\mathrm{d}\phi$, where ϕ is the polar coordinate, which runs along the periphery of the pipe;
- the horizontal pipe has an inclination of θ.

The Nusselt's theory of film condensation assumes that the driving force for the condensation is the heat transfer through the liquid film. Hence, the released heat of condensation is equal to the heat, which can be conducted through the liquid film to the wall.

The heat flux across the liquid film depends on the film thickness and the thermal conductivity of the liquid (Eq. 2.41), if the convective effects are neglected:

$$\mathrm{d}q''(\phi) = \frac{\lambda_l}{\delta_f}\left(T_s - T_w\right) R\mathrm{d}\phi. \tag{2.41}$$

Using the definition of the heat transfer coefficient (Eq. 2.42), we can conclude that the local heat transfer coefficient of the fluid element is equal to the thermal conductivity divided by the film thickness (Eq. 2.43):

$$\alpha_{loc}(\phi) = \frac{q''(\phi)}{T_s - T_w}, \tag{2.42}$$

$$\alpha_{loc}(\phi) = \frac{\lambda_l}{\delta_f(\phi)}. \tag{2.43}$$

Consequently, the heat transfer coefficient is determined through the local liquid film thickness. The film thickness is determined by solving the force balance equation in the direction of the flow (*i.e.* ϕ) for the fluid element (Eq. 2.44):

$$(r-(R-\delta_f))r\,R\mathrm{d}\phi\,\mathrm{d}x\,(\rho_l-\rho_v)g\cos\theta\sin\phi = \tau\frac{\mathrm{d}u}{\mathrm{d}r}r\,\mathrm{d}\phi\,\mathrm{d}x. \tag{2.44}$$

The inertia effects are negligible [106], and steady state conditions are assumed; therefore, the flow element has zero acceleration. The left hand side of Eq. 2.44 is the gravity acting on the element in the direction of the fluid velocity, accounting for the inclination of the pipe. The left hand side is the viscosity force.

The above equation is rearranged (Eq. 2.45) by applying the transition of the coordinate system($y = R - r$). The y coordinate is zero at the pipe wall, and it is equal to R in the center of the pipe:

$$(\delta_f - y)(\rho_l - \rho_v)g\cos\theta\sin\phi = \mu_v\frac{\mathrm{d}^2u}{\mathrm{d}y^2}. \tag{2.45}$$

The velocity distribution (Eq. 2.47) in the condensate film is calculated by integrating Eq. 2.45. The velocity is zero at the wall, and the velocity gradient is zero at the liquid–vapor interface (Eq. 2.46):

$$u(y=0) = 0; \qquad \left|\frac{\mathrm{d}u}{\mathrm{d}y}\right|_{y=\delta_f} = 0, \tag{2.46}$$

$$u(y) = \frac{(\rho_l-\rho_v)g\cos\theta\sin\phi}{2\mu_l}\left(y\delta_f - \frac{y^2}{2}\right). \tag{2.47}$$

The velocity distribution in the liquid film is used to calculate the mass flow rate of the flow element, by integrating the velocity along the film thickness, and multiplying with the liquid density (Eq. 2.48):

$$\dot{m} = \rho_l\int_0^{\delta_f} u(y)\mathrm{d}y \;= \frac{(\rho_l-\rho_v)g\cos\theta\sin\phi}{3\mu_l}\,\delta_f^3\rho_l. \tag{2.48}$$

The above equation is a function between the mass flow rate and the film thickness. The differentiation of the relation yields Eq. 2.49. The $\mathrm{d}\dot{m}$ term is the additional mass flow in the corresponding fluid element, which originates from condensation:

$$\frac{\mathrm{d}\dot{m}}{\mathrm{d}\delta_f} = \frac{\rho_l(\rho_l-\rho_v)g\cos\theta\sin\phi}{\mu_l}\,\delta_f^2. \tag{2.49}$$

The energy conservation equation provides a relation between the additional mass flow rate and the heat flux (Eq. 2.50):

$$\mathrm{d}q = h_{lv}\mathrm{d}\dot{m}. \tag{2.50}$$

The heat flux in Eq. 2.50 is substituted with Eq. 2.41, obtaining the additional mass flux (Eq. 2.51):

$$\mathrm{d}\dot{m} = \frac{\lambda_l}{\delta_f}\frac{1}{h_{lv}}\left(T_s - T_w\right)R\mathrm{d}\phi. \tag{2.51}$$

Equation 2.51 is substituted into Equation 2.49, the result is a correlation between the flow rate and the film thickness (Eq. 2.52):

$$\frac{\lambda_l}{\delta_f}\frac{1}{h_{lv}}\left(T_s - T_w\right)\frac{R\mathrm{d}\phi}{\mathrm{d}\delta_f} = \frac{\rho_l(\rho_l - \rho_v)g\cos\theta\sin\phi}{\mu_l}\delta_f^2(\phi). \tag{2.52}$$

The variables are separated (Eq. 2.53), and the equation is integrated (Eq. 2.54). After rearrangement, the film thickness is expressed as a function of the angular coordinate ϕ (Eq. 2.55):

$$\lambda_l\mu_l\left(T_s - T_w\right)R\mathrm{d}\phi = \rho_l(\rho_l - \rho_v)g\cos\theta\sin\phi h_{lv}\delta_f^3(\phi)\mathrm{d}\delta, \tag{2.53}$$

$$\lambda_l\mu_l\left(T_s - T_w\right)R\phi = \rho_l(\rho_l - \rho_v)g\cos\theta\sin\phi h_{lv}\frac{\delta_f^4(\phi)}{4}, \tag{2.54}$$

$$\delta_f(\phi) = \left[\frac{4\lambda_l\mu_l\left(T_s - T_w\right)R}{\rho_l(\rho_l - \rho_v)g\cos\theta h_{lv}}\right]^{1/4}\left[\frac{\phi}{\sin\phi}\right]^{1/4}. \tag{2.55}$$

The film thickness is substituted into Eq. 2.43; as a result, the local heat transfer coefficient is estimated (Eq. 2.56):

$$\alpha_{loc}(\phi) = \left[\frac{\rho_l(\rho_l - \rho_v)g\cos\theta h_{lv}\lambda_l^3}{4\mu_l\left(T_s - T_w\right)R}\right]^{1/4}\left[\frac{\sin\phi}{\phi}\right]^{1/4}. \tag{2.56}$$

The integral of the local heat transfer coefficient for the periphery of the pipe is the average heat transfer coefficient of the liquid film (Eq. 2.57):

$$\alpha_f = \left[\frac{\rho_l(\rho_l - \rho_v)g\cos\theta h_{lv}\lambda_l^3}{4\mu_l\left(T_s - T_w\right)R}\right]^{1/4}\frac{2}{\Phi_{strat}}\int_0^{\Phi_{strat}/2}\left[\frac{\sin\phi}{\phi}\right]^{1/4}d\phi. \tag{2.57}$$

This latter expression contains known geometrical and fluid parameters and the inner wall temperature. The stratification angle comes from the flow pattern calculation. The temperature is calculated in the MATLAB function, as it is described in the next section.

2.5 Calculation of the inner wall temperature

The heat transfer through the wall is described by the heat conduction equation (Eq. 2.58). To calculate the temperature of the inner wall of the tube, the equation is solved:

$$\frac{\partial}{\partial r}\lambda r\frac{\partial T}{\partial r}=0. \tag{2.58}$$

The following assumptions were considered during the calculation:

- no heat generation happens and no heat is stored in the pipe wall;
- steady state heat conductivity is assumed;
- the wall thermal conductivity is linear with the temperature (Eq. 2.59);
- the boundary conditions for the outer and inner walls are Eq. 2.60 and 2.61, *i.e.* the heat transfer coefficient corresponds to the temperature gradient at the wall;
- polar coordinate system was applied:

$$\lambda_w=\lambda_0(1+\beta\,T), \tag{2.59}$$

$$\alpha_{in}\left(T_s-T_{w,in}\right)=\lambda\left[\frac{\partial T}{\partial r}\right]_{R,in}, \tag{2.60}$$

$$\alpha_{out}\left(T_{w,out}-T_{out}\right)=\lambda\left[\frac{\partial T}{\partial r}\right]_{R,out}. \tag{2.61}$$

The heat conduction equation is integrated along the radius (Eq. 2.62). The C constant is evaluated from the boundary condition at the inner wall (Eq. 2.60, resulting Eq. 2.63):

$$\lambda r\frac{\partial T}{\partial r}=C, \tag{2.62}$$

$$C=\alpha_{in}R_{in}\left(T_s-T_{w,in}\right). \tag{2.63}$$

After separating the variables, and integrating the equation (Eq. 2.64), the relation between the outer and inner wall temperature obtains (Eq. 2.65):

$$\int_{T_{w,in}}^{T_{w,out}}\lambda_0(1+\beta\cdot T)\mathrm{d}T=\int_{R_{in}}^{R_{out}}\frac{C}{r}\mathrm{d}r, \tag{2.64}$$

$$\lambda_0\left(T_{w,out}-T_{w,in}\right)+\frac{\lambda_0\beta}{2}\left(T_{w,out}^2-T_{w,in}^2\right)=C\cdot\ln\frac{R_{out}}{R_{in}}. \tag{2.65}$$

The two boundary condition equations above (Eq. 2.60-2.61) are divided, and rearranged. The expression is obtained for the outer wall temperature as a function of the inner wall

temperature and the outer cooling water temperature (Eq. 2.66):

$$T_{w,out} = \frac{\alpha_{in} R_{in}}{\alpha_{out} R_{out}} \left(T_s - T_{w,in}\right) + T_{out}. \tag{2.66}$$

Equation 2.63 and 2.66 is substituted into equation 2.65. The result contains one unknown parameter, which is the inner wall temperature (Eq. 2.67):

$$\lambda_0 \left(\left(\frac{\alpha_{in} R_{in}}{\alpha_{out} R_{out}} \left(T_s - T_{w,in}\right) + T_{out} \right) - T_{w,in} \right) + \frac{\lambda_0 \beta}{2} \left(\left(\frac{\alpha_{in} R_{in}}{\alpha_{out} R_{out}} \left(T_s - T_{w,in}\right) + T_{out} \right)^2 - T_{w,in}^2 \right) = \alpha_{in} R_{in} \left(T_s - T_{w,in}\right) \ln \frac{R_{in}}{R_{out}}. \tag{2.67}$$

The equation can be rearranged into the form of a quadratic equation (Eq. 2.68). The a, b, c parameters contain known parameters (Eq. 2.69-2.71):

$$\mathrm{a} \cdot T_{w,in}^2 + \mathrm{b} \cdot T_{w,in} + \mathrm{c} = 0, \tag{2.68}$$

$$\mathrm{a} = \frac{\lambda_0 \beta}{2} \left(\left(\frac{\alpha_{in} R_{in}}{\alpha_{out} R_{out}} \right)^2 - 1 \right), \tag{2.69}$$

$$\mathrm{b} = -\lambda_0 \left(\frac{\alpha_{in} R_{in}}{\alpha_{out} R_{out}} - 1 \right) - \lambda_0 \beta \frac{\alpha_{in} R_{in}}{\alpha_{out} R_{out}} \left(\frac{\alpha_{in} R_{in}}{\alpha_{out} R_{out}} T_{out} \right) + \alpha_{in} R_{in} \ln \frac{R_{out}}{R_{in}}, \tag{2.70}$$

$$\mathrm{c} = \lambda_0 \frac{\alpha_{in} R_{in}}{\alpha_{out} R_{out}} T_s + \lambda_0 T_{out} + \frac{\lambda_0 \beta}{2} \left(\frac{\alpha_{in} R_{in}}{\alpha_{out} R_{out}} T_{out} \right)^2 - \alpha_{in} R_{in} T_s \ln \frac{R_{out}}{R_{in}}. \tag{2.71}$$

The two roots of the quadratic equation are obtained by the quadratic formula (Eq. 2.72):

$$T_{w,in}^{1;2} = \frac{-\mathrm{b} \pm \sqrt{\mathrm{b}^2 - 4\mathrm{ac}}}{2\mathrm{a}}. \tag{2.72}$$

The temperature of the inner wall is higher than the outer surface temperature, and lower than the saturation temperature, which provides a filter for choosing the physical solution of the equation.

The calculation described in this section is applicable for both the upper and bottom part of the pipe. The iteration process is applied at the upper part, because the equation contains the heat transfer coefficient of the inner wall. For the bottom part the situation is simpler, because the heat transfer coefficient equation does not contain the inner wall temperature.

2.6 Calculation of the average heat transfer coefficient

The average heat transfer coefficient of the cross section can be calculated (Eq. 2.73) from the two heat transfer coefficient and the stratification angle. The length of the upper and bottom part is estimated by Eq. 2.74 and 2.75:

$$\alpha_{average} = \frac{\alpha_f p_f + \alpha_s p_b}{p_f + p_b} = \frac{\alpha_f \Phi_{strat} + \alpha_b (2\pi - \Phi_{strat})}{2\pi}, \tag{2.73}$$

$$p_f = R\Phi_{strat}, \tag{2.74}$$

$$p_b = R(2\pi - \Phi_{strat}). \tag{2.75}$$

2.7 Conclusions from the calculation with the mechanistic model

The steps of the heat transfer calculation are summarized in Fig. 2.5. The functions were coded in MATLAB. The calculation results in an average heat transfer coefficient for a computational node, *i.e.* for the cross section of a horizontal pipe. The calculation for the upper liquid film and the bottom axial flume is independent, and an average heat transfer coefficient results from the flow pattern calculation.

The heat transfer coefficient of the cross section depends on the radius of the pipe, the void fraction, the initial pressure, the outlet temperature and the inclination of the pipe. Figure 2.6 shows an example of the output of the MATLAB model; the box shows the input parameters. The calculated results are the two heat transfer coefficients, the inner wall temperatures, the stratification angle, the film thicknesses, and the average heat transfer coefficient.

The code allows the change of the parameters, and the analysis of the heat transfer depending on the various input parameters.

The INVEP experimental conditions were used to test the model (Section 1.4.1). Figure 2.6 shows the output of the MATLAB code for the b07 experiment. The purpose was to analyze the ratio between the upper and bottom part heat transfer coefficient, and the average heat transfer coefficient dependence on the local void fraction.

The void fraction dependence was tested by changing the void fraction with constant initial parameters. Figure 2.7 shows the average heat transfer coefficient according to the void fraction data for the b07 INVEP experiment. The heat transfer coefficient is changing with a changing void fraction. The increasing heat transfer surface with the increasing void in the tube results in a higher heat transfer to the secondary side.

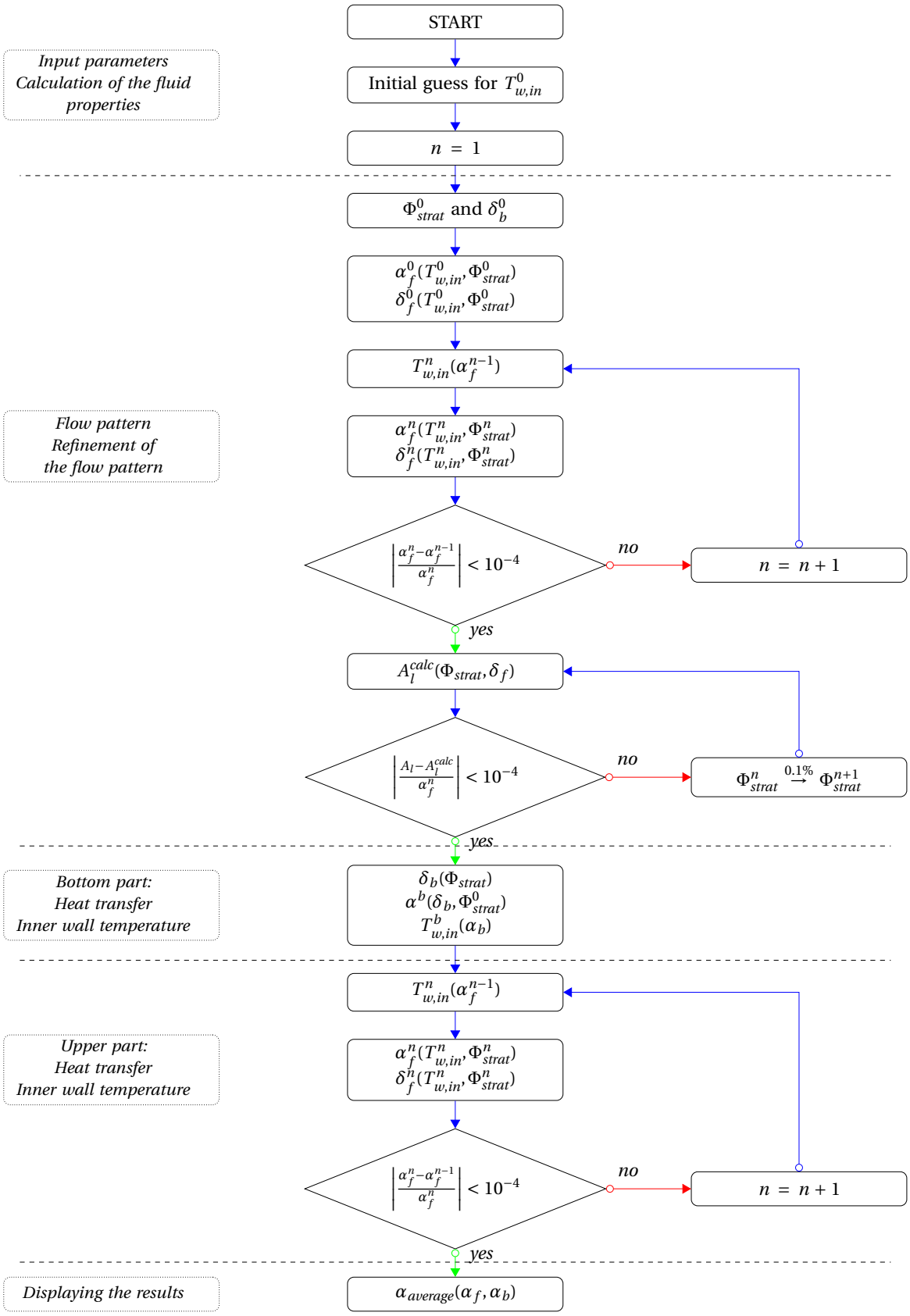

Figure 2.5: Flowchart of the MATLAB calculation

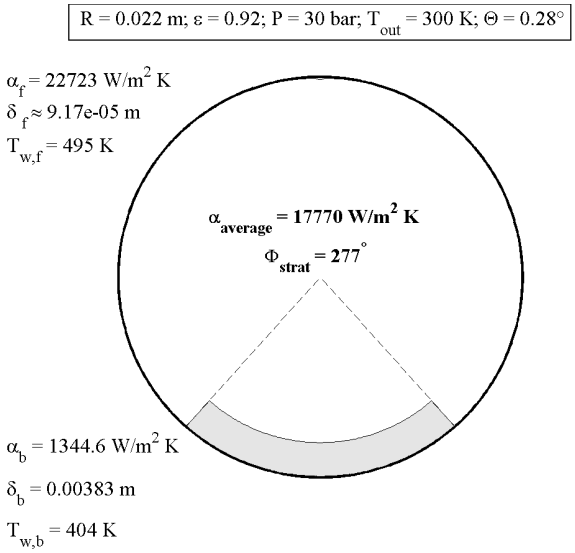

Figure 2.6: Output of the MATLAB model (HTC is the heat transfer coefficient)

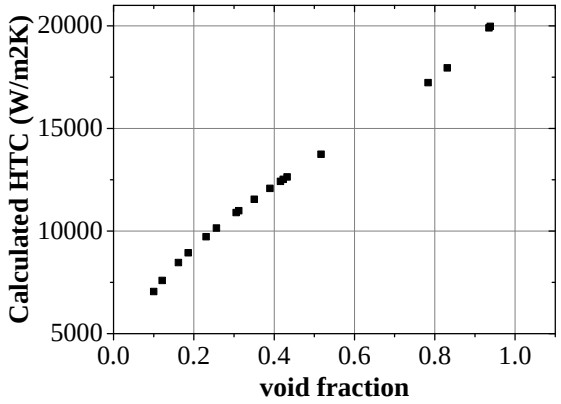

Figure 2.7: Calculated heat transfer coefficient as a function of void fraction in the MATLAB calculation

The conclusions form the MATLAB calculation are the following:

- the bottom part heat transfer coefficient is negligible compared to the heat transfer coefficient of the upper part;
- the void fraction is an important parameter, which has a significant effect on the heat transfer coefficient. Therefore, the stratification angle effect is not negligible;
- the area of the liquid at the upper part is negligible compared to the bottom part liquid fraction; therefore, the refinement of the flow pattern calculation is not necessary.

The above described model was implemented into the RELAP5/mod3.3, and the above conclusions were considered (See Section 4.1). The modified RELAP5 code was validated against the INVEP experiment. The assumptions of the model were justified by the computational fluid dynamics calculations (Chapter 5).

3 Condensation model development for computational fluid dynamics

The mechanistic approach of the previous chapter is based on a simplified geometry to describe the flow pattern in a horizontal pipe with condensation. Although the model does not fully represent the reality, it is sufficient to capture the main features. The mechanistic approach requires the assumption on the distribution of the phases and the velocities in the cross-section, while in reality the flow field and the phase distribution are the results of three-dimensional fluid-dynamics represented by the Navier-Stokes equations.

As an alternative to the mechanistic approach, three-dimensional fluid dynamics simulations using a commercial code was pursued. The simulations deliver the geometry of the interface as well as the flow field as a result of the integration of fundamental governing equations. For this purpose, an appropriate representation of the interface has to be chosen, which is the VOF method. The CFD simulations rely on geometry independent models, as they are formulated for the cells of the discretized flow domain. Therefore, experimental data from geometries different from the slightly inclined pipe can be used to check the validity of the CFD models.

This chapter summarizes the modeling strategy for phase change phenomena, particularly condensation, in CFD codes. Four methods are presented to calculate the mass and heat transfer. The four methods were coded in the C computational language, and they were implemented into the FLUENT software.

The first section (3.1) describes the theory of phase transition at the liquid–vapor interfacial region. Macroscopic treatment is applied to derive the heat flux balance equation at the interface. Another approach, the phase field theory is used to derive an equation for the mass transfer rate at the interface. Section 3.2 describes the theory of the four condensation models. Section 3.3 summarizes the considered aspects of the implementation, and Section 3.4 presents details about the implementation.

The FLUENT code with the implemented models was validated calculating condensation in two experimental facilities (Chapter 5).

3.1 Phase change in the liquid–vapor interfacial region

The driving force of the thermal phase transition is the temperature difference between two adjacent phases. We talk about melting or solidification if the two phases are solid and liquid, and boiling and condensation occurs in liquid–vapor interactions. In the following sections, only liquid–vapor phenomena are considered [104]. Both microscopic and macroscopic perspectives are introduced.

In continuum mechanics, the interface is a two-dimensional surface, where sharp discontinuity occurs in the material properties [104]. This macroscopic treatment neglects the thickness of the interface (Fig. 3.1.b). The microscopic treatment (Fig. 3.1.a) considers a region between the bulk liquid and vapor, where the density and other material properties continuously vary.

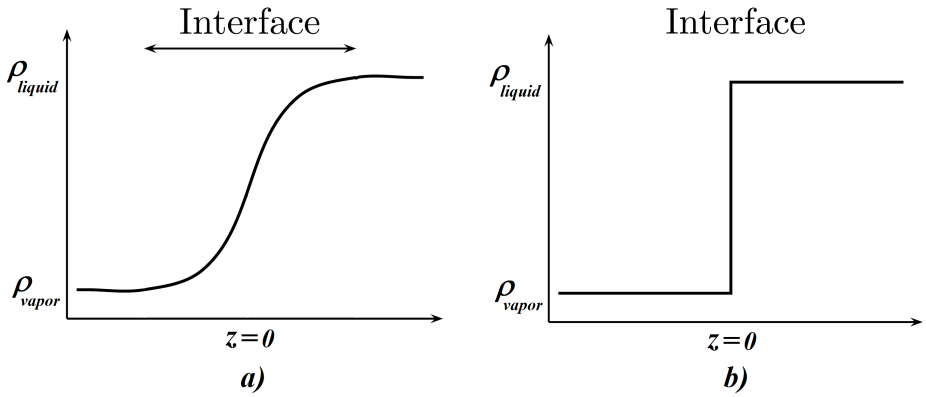

Figure 3.1: Microscopic (*b*) and macroscopic (*b*) treatment of the density at the interface

The microscopic perspective acknowledges the presence of a thin interfacial region on a molecular level (Fig. 3.2). The molecular interactions in this region lead to a better understanding of the interfacial phenomena.

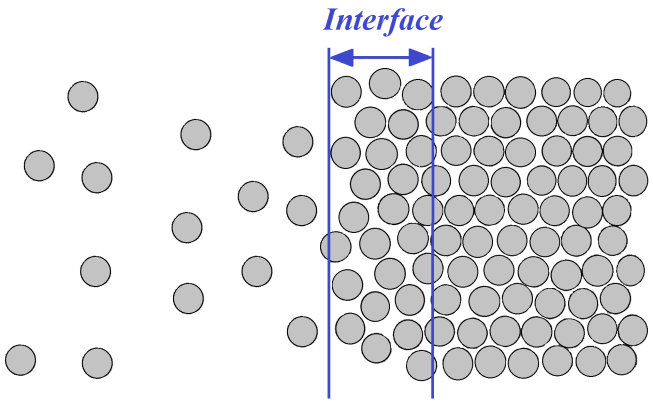

Figure 3.2: Molecular density variation at the interface in the molecular level

In the interfacial region the density of the molecules is lower than in the bulk liquid. The higher spacing between the molecules weakens the repulsive force of the direct neighbors,

and has negligible effect on the attractive force of the other molecules. Thus, this force imbalance draws the molecules towards the bulk fluid. The molecules in the interfacial region have higher energy; in other words, the interface introduces an additional free energy in the interfacial region [104], which is interpreted as a surface tension.

The Van der Waals theory of capillarity is used to extend the classical thermodynamic analysis to the interfacial region. The theory assumes that the material properties vary continuously at the interface, where local thermodynamic equilibrium exists. The theory is based on the mean field theory, *i.e.* the parameters of each molecule is driven by the mean field of the surrounding molecules [104].

The theory applies to a system with constant temperature and volume, hence, the second law of thermodynamics states that the equilibrium of the system corresponds to a minimum in the Helmholtz free energy, *i.e.* to the surface tension [104].

The microscopic treatment explains the origin of the surface tension and capillarity phenomenon. Such phenomena are beyond the scope of this thesis; for further details on the topic, see *e.g.* [107], [108].

The next section considers the macroscopic aspects of the interface to describe the transport effects between the two phases.

3.1.1 Transport effects at the liquid-vapor interface

In macroscopic perspective the interface is a two-dimensional surface between the liquid and the vapor of the same substance, where the material properties change abruptly (sharp interface approach). The boundary and transport conditions at the interface have to be determined before solving the continuity equations [104].

To derive the boundary conditions at the interface, the conservation principle of the mass, momentum and energy is applied for a thin control volume with an area A_i around the interface. The control volume moves together with the interface at the speed of $\mathrm{d}Z_i/\mathrm{d}t$ in the direction of the interface normal vector ($\vec{n}$); and it is thin enough that no mass accumulates here (Fig. 3.3). The velocity of the liquid and the vapor phase in the direction of the interface normal vector is $w_{l,n}$ and $w_{v,n}$, respectively. The $\vec{s}$ vector is an orthogonal direction of the tangential plane of the interface. The interface normal vector is calculated as $\vec{n}_l = -\vec{n}_v = \nabla\epsilon_v / |\nabla\epsilon_v|$, where ϵ is the void fraction.

Figure 3.4 shows the mass transport and the tangential and normal momentum transport at the interface. Figure 3.5, similarly, shows the energy balance at the interface.

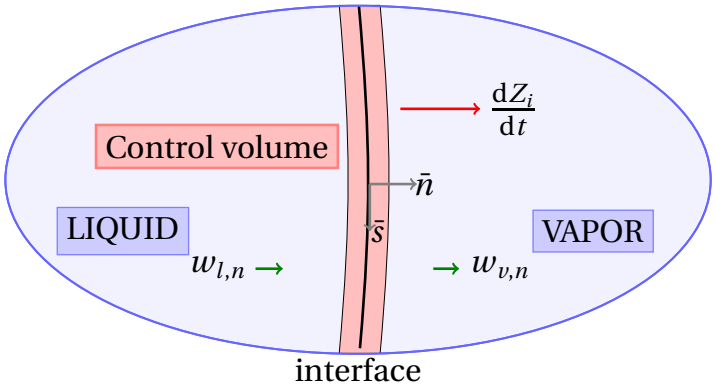

Figure 3.3: The interface and the control volume between the liquid and vapor phases. The $\vec{s}$–$\vec{n}$ coordinate system indicates the tangential and the normal vector of the interface. The $\vec{s}$ vector is an orthogonal direction of the tangential plane. The liquid, the vapor and the interface move with different velocities ($w_{v,n}$, $w_{l,n}$ and dZ_i/dt, respectively)

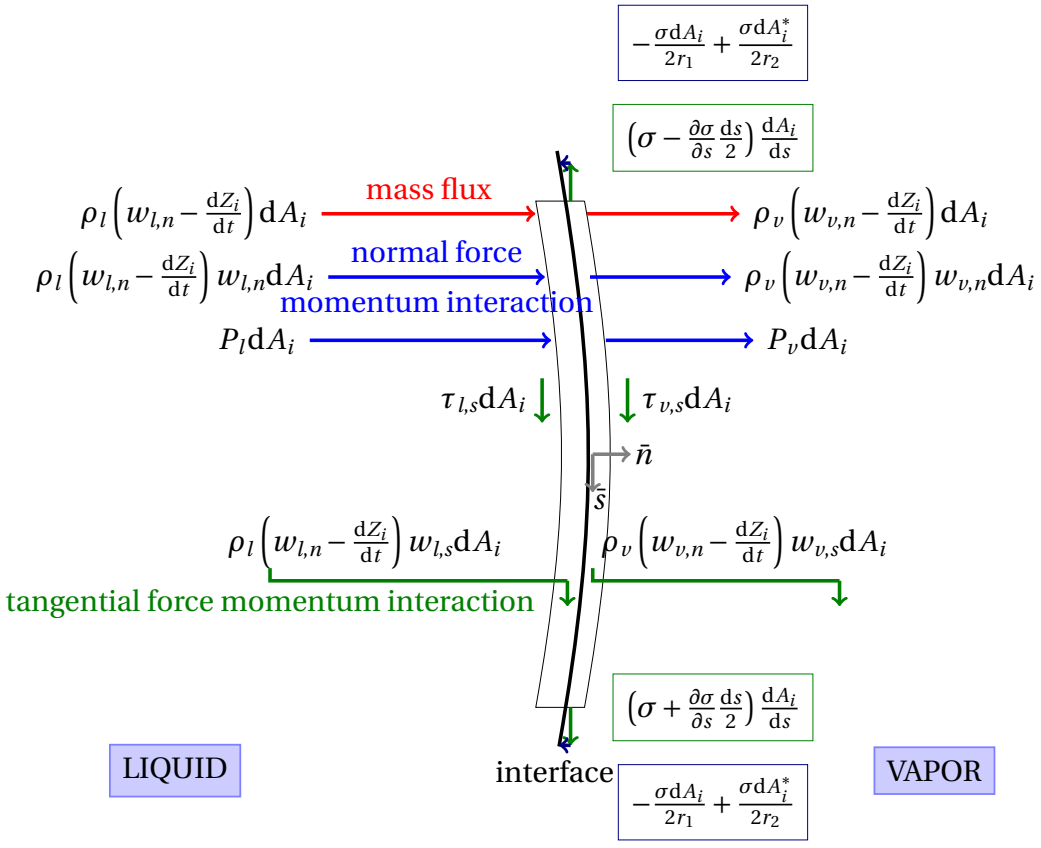

Figure 3.4: Mass and momentum balance at the interface. A_i is the area of the interface control volume, τ is the shear stress, σ is the surface tension, Z_i is the location of the interface along the normal coordinate, r_1 and r_2 are the inner and outer radius of the interface, w is velocity component, where the index indicates the direction and the phase. Coordinates and velocities in the normal direction from the liquid to the vapor are positive [104].

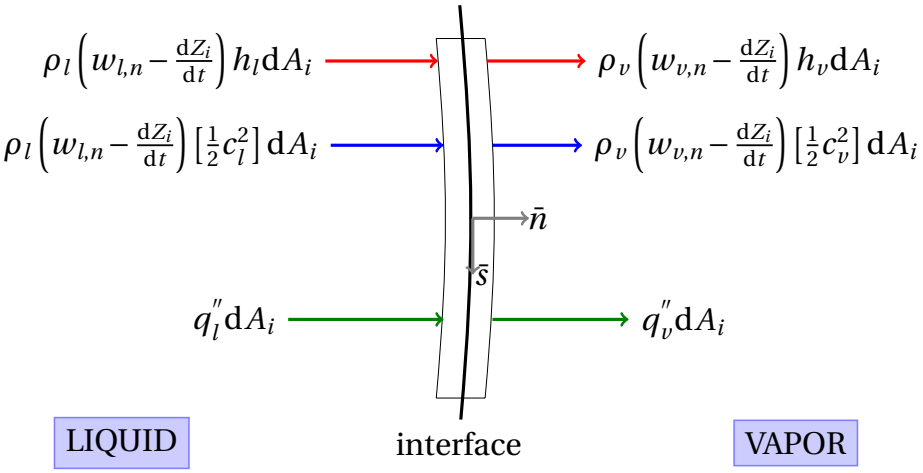

Figure 3.5: Energy balance at the interface considering the contribution of the fluid enthalpy and kinetic energy transported by the phases, the thermal energy transport through conduction and radiation. A_i is the area of the interface control volume, Z_i is the location of the interface along the normal coordinate, h is the entropy of the corresponding phase, w is velocity component, where the index indicates the direction and the phase, c is the magnitude of the velocity, q'' is a heat flux. Coordinates and velocities in the normal direction from the liquid to the vapor are positive [104].

The liquid and vapor mass flux towards the interface considers a relative velocity of the corresponding phase and the control volume. The **conservation of mass** principle requires that the mass entering an leaving the control volume is equal, thus (Eq. 3.1):

$$\rho_l\left(w_{l,n}-\frac{dZ_i}{dt}\right)dA_i=\rho_v\left(w_{v,n}-\frac{dZ_i}{dt}\right)dA_i. \tag{3.1}$$

The **conservation of momentum** normal to the interface (Eq. 3.2) considers the pressure (P) and surface tension forces (σ is a surface tension, r_1 and r_2 are the inner and outer radius of the interface):

$$P_l-P_v=\sigma\left(\frac{1}{r_1}+\frac{1}{r_1}\right)+\rho_v\left(w_{v,n}-\frac{dZ_i}{dt}\right)w_{v,n}-\rho_l\left(w_{l,n}-\frac{dZ_i}{dt}\right)w_{l,n}. \tag{3.2}$$

The **conservation of momentum** in the direction of the tangent vector $\vec{s}$ includes the shear stress (τ) at the interface and the surface tension variation along the interface (Eq. 3.3):

$$\tau_{l,s}-\tau_{v,s}-\left(\frac{d\sigma}{ds}\right)=\rho_l\left(w_{l,n}-\frac{dZ_i}{dt}\right)w_{l,s}-\rho_v\left(w_{v,n}-\frac{dZ_i}{dt}\right)w_{v,s}. \tag{3.3}$$

The **conservation of energy** contains the heat fluxes on the two sides of the interface (q''), the kinetic energy (c is the magnitude of the velocity) and the enthalpy (h) transported by the liquid and the vapor (Eq. 3.4):

$$q_v''-q_l''=\rho_l\left(w_{l,n}-\frac{dZ_i}{dt}\right)\left[\frac{1}{2}c_l^2+h_l\right]-\rho_v\left(w_{v,n}-\frac{dZ_i}{dt}\right)\left[\frac{1}{2}c_v^2+h_v\right]. \tag{3.4}$$

The momentum balance equation normal to the interface (Eq. 3.2) takes the form of the Young-Laplace equation, if the liquid and vapor momentum terms are neglected (Eq. 3.5). Consequently, the pressure difference of the two fluids depends on the geometry of the interface and the surface tension:

$$P_l - P_v = \sigma \left(\frac{1}{r_1} + \frac{1}{r_2} \right). \tag{3.5}$$

For constant surface tension and continuously varying velocity field in the phases, together with a no-slip condition for the tangential velocity component, the momentum balance equation (Eq. 3.3) reduces to the shear stress balance at the interface (Eq. 3.6):

$$\tau_{l,s} = \tau_{v,s}. \tag{3.6}$$

For Newtonian fluids the shear balance equation takes a form of Eq. 3.7, where μ is the viscosity:

$$\mu_l \left(\frac{\partial w_{l,n}}{\partial s} + \frac{\partial w_{l,s}}{\partial s} \right)_{z=Z_i} = \mu_v \left(\frac{\partial w_{v,n}}{\partial s} + \frac{\partial w_{v,s}}{\partial s} \right)_{z=Z_i}. \tag{3.7}$$

The magnitude of the velocity in the energy balance equation (Eq. 3.4) is calculated relative to the control volume (Eq. 3.8):

$$c_p = \sqrt{\left(w_{p,n} - \frac{\mathrm{d}Z_i}{\mathrm{d}t} \right)^2 + w_{p,s1}^2 + w_{p,s2}^2}. \tag{3.8}$$

The mass conservation equation (Eq. 3.1) is substituted in the energy balance equation (Eq. 3.4), and thermal equilibrium is assumed at the interface ($h_{lv} = h_l - h_v$); hence, the conservation of energy is reformulated as Eq. 3.9:

$$q_v'' - q_l'' = \rho_l \left(w_{l,n} - \frac{\mathrm{d}Z_i}{\mathrm{d}t} \right) \left[1 + \frac{c_l^2 - c_v^2}{2h_{lv}} \right] h_{lv}. \tag{3.9}$$

The continuous velocity field across the interface indicates that the vapor and liquid velocity magnitude is equal. Moreover, the saturation temperature is equal to the saturation temperature of the corresponding vapor pressure, if the interface curvature is small. If the radiation effects are negligible, the heat flux is equal to the thermal heat conductivity (λ) multiplied with the temperature gradient at the interface (Eq. 3.10):

$$q'' = \lambda \left(\frac{\mathrm{d}T}{\mathrm{d}z} \right)_{z=Z_i}. \tag{3.10}$$

With the above assumptions, the thermal boundary condition at the interface is:

$$\lambda_v \left(\frac{\mathrm{d}T}{\mathrm{d}z} \right)_{z=Z_i} - \lambda_l \left(\frac{\mathrm{d}T}{\mathrm{d}z} \right)_{z=Z_i} = \rho_l \left(w_{l,n} - \frac{\mathrm{d}Z_i}{\mathrm{d}t} \right) h_{lv}. \tag{3.11}$$

The right hand side of Eq. 3.11 is the mass transfer rate per unit area (Γ) multiplied by the latent heat of evaporation. Hence, the interfacial mass transfer rate is derived from the

energy balance at the interface (Eq. 3.12):

$$\dot{\Gamma}_{lv} = \frac{q_v'' - q_l''}{h_l - h_v}. \tag{3.12}$$

The mass transfer rate per unit volume ($\dot{m}$) is the mass transfer rate per unit area multiplied by the interfacial area density (A_{lv}) :

$$\dot{m}_{lv} = \dot{\Gamma}_{lv} A_{lv}. \tag{3.13}$$

The interfacial area density is the gradient of the void fraction (Eq. 3.14) :

$$A_{lv} = |\nabla \epsilon| . \tag{3.14}$$

Substituting the above expressions in Eq. 3.9, the result is the volumetric phase change mass transfer equation (Eq. 3.15):

$$\dot{m}_{lv} = \frac{\lambda_v \left(\frac{\mathrm{d}T}{\mathrm{d}z}\right)_{z=Z_i} - \lambda_l \left(\frac{\mathrm{d}T}{\mathrm{d}z}\right)_{z=Z_i}}{h_{lv}} \nabla \epsilon. \tag{3.15}$$

The above equation provides the boundary condition at the interface, which closes the continuity equations.

3.1.2 Phase field modeling of the interfacial region

Solving directly the heat flux balance at the sharp interface (Eq. 3.15) obtains accurate result only if the thermal boundary layer is resolved by the mesh. The model implementation into numerical solvers is difficult due to the calculation of the temperature gradient. The above model was implemented into the FLUENT software (see Section 3.2). However, another approach is used as well, to overcome the limitations of the heat flux balance based models.

Badillo [84], [85] developed a general model using phase field theory for boiling phenomena. This section summarizes his results.

The phase field theory is a mathematical approach to calculate interface related problems. Diffuse interface is considered, *i.e.* the material properties vary continuously along the interfacial region. The interfacial region in the theory is not equivalent to the one of the micro scale, which is couple of angstrom thick. The interfacial region here is rather a mathematical concept, which is defined by the size of the computational cells.

The principle behind the phase field theory is the free energy ($\mathbb{H}$) minimization of processes in the nature. The system, which evolves from the higher free energy level to a lower one, is described mathematically by the negative free energy derivative (Eq. 3.16):

$$\frac{\mathrm{d}\mathbb{H}}{\mathrm{d}t} < 0. \tag{3.16}$$

If the free energy changes only by the distribution of an order parameter (ϕ), then the above equation is reformulated (Eq. 3.17) with the functional derivative (δ) and the integral on the system volume (Ω):

$$\int_{\Omega}\left(\frac{\delta\mathbb{H}}{\delta\phi}\frac{\partial\phi}{\partial t}\right)\mathrm{d}\Omega<0. \tag{3.17}$$

To satisfy the inequality for a non-conserved order parameter, the evolution of ϕ is:

$$\frac{\partial\phi}{\partial t}=-\sum_{i}M_i\left(\frac{\delta\mathbb{H}}{\delta\phi}\right)^{i}\qquad\text{for}\quad i=1,2,3...\quad\text{and}\quad M_i>0. \tag{3.18}$$

The linear terms dominate in systems close to the equilibrium; thus, the higher order terms are neglected, and Eq. 3.18 yield the Allen-Cahn equation (Eq. 3.19), which is a governing equation in phase field models with non-conserved order parameters:

$$\frac{\partial\phi}{\partial t}=-M\hat{\mu}, \tag{3.19}$$

where the M constant is a mobility coefficient, and $\hat{\mu}$ is the transformation potential.

The order parameter in phase change processes is the phase field. The phase field has two distinct values, and it varies smoothly across the interface [109]. The interfacial region is represented by the energy of the mixture.

Badillo [84] derived a set of equations to describe the flow field using the two-phase flow averaged approach. The detailed derivation is found in [84], and it is not repeated here. The two-phase flow averaged approach assumes an internal micro-structure, where the two phases are separated by a sharp atomic interface, and an averaging procedure is done on a control volume containing an interface (Fig. 3.6). The $X_p(\vec{x})$ function is equal to one in phase p, and it is zero otherwise. The average of this function obtains the volume fraction ($\phi_p=\langle X_k\rangle$). The volumetric average of a quantity Φ (for phases $p=v,l$) in the control volume is defined as:

$$\langle\Phi\rangle=\frac{1}{V}\int_{V}\left(\Phi X_p\right)\mathrm{d}V_p; \tag{3.20}$$

The normal vector of the interface is $\vec{n}_p=-\nabla\phi_p/\left|\nabla\phi_p\right|$. The velocity of the mixture is the volume-weighted average:

$$\bar{\vec{u}}=\phi_l\left\langle\vec{u}_l{}^{l}\right\rangle+\phi_v\left\langle\vec{u}_v{}^{v}\right\rangle; \tag{3.21}$$

Similarly, the material properties, as the density ($\bar{\rho}=\rho_l\phi_l+\rho_v\left(1-\phi_l\right)$) and the heat capacity per unit mass ($\bar{C}_p=\left(\rho_l C_{pl}\phi_l+\rho_v C_{pv}\left(1-\phi_l\right)\right)/\rho$) are calculated as a weighted average.

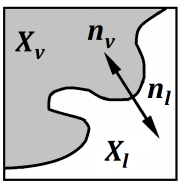

Figure 3.6: Control volume for the two-phase flow averaging approach [84]

The above described averaging technique yields the model equations ($\dot{m}_l$ is an interfacial mass transfer rate per unit volume):

1. Mass conservation:
$$\nabla \cdot \bar{\vec{u}} = -\left(\frac{1}{\rho_l} - \frac{1}{\rho_v}\right)\dot{m}_l; \tag{3.22}$$
2. Linear momentum conservation (for the details about the momentum equation, see [84]):
$$\frac{\partial \bar{\rho}\bar{\vec{u}}}{\partial t} + \nabla \cdot \left(\bar{\rho}\bar{\vec{u}}\bar{\vec{u}}\right) = -\nabla \bar{P} + \nabla \cdot \left(\bar{\mu}\left(\nabla \bar{\vec{u}} + \nabla \bar{\vec{u}}^T\right)\right) + \bar{\vec{f}} + \vec{f}_{lv}^{\sigma}; \tag{3.23}$$
3. Energy conservation:
$$\bar{\rho}\bar{C_P}\left(\frac{\partial T}{\partial t} + \bar{\vec{u}}\nabla T\right) = -\nabla \bar{q} - h_{lv}\dot{m}_l + \bar{S} + \left(\rho_l C_{Pl} - \rho_v C_{Pv}\right) \times \frac{w}{\sqrt{2}}\left(\nabla \cdot \bar{\vec{u}}\right)\vec{n}_l \nabla T; \tag{3.24}$$
In the equation the mixture heat flux is defined as $\bar{q} = \phi_l \bar{q}_l + \phi_v \bar{q}_v$, similarly to the mixture source ($\bar{S}$). The characteristic interface thickness is w. The last term in the right hand side is a correction factor, which acts against the non-linearity of the energy equation due to the phase change. This term (Eq. 3.25) is zero outside of the interfacial area, and can be calculated by substituting the mass conservation equation:
$$E_{corr} = \left(\rho_l C_{Pl} - \rho_v C_{Pv}\right) \times \frac{w}{\sqrt{2}}\left(\frac{1}{\rho_v} - \frac{1}{\rho_l}\right)\vec{n}_l \nabla T; \tag{3.25}$$
4. Phase field equation:
$$\frac{\partial \phi_l}{\partial t} + \nabla \cdot \left(\phi_l \bar{\vec{u}}\right) = -\frac{\dot{m}_l}{\rho_l} + \left(2\phi_l - 1\right)\nabla \bar{\vec{u}}; \tag{3.26}$$
5. Mass evaporation rate:
$$\dot{m}_l = \rho M \hat{\mu}. \tag{3.27}$$
The above equation is the consequence of the Allen-Cahn equation (Eq. 3.19), which describes the time derivative of a non-conserved order parameter. The mobility coefficient is calculated as Eq. 3.28, the transition potential is Eq. 3.29:
$$M = \frac{w I_0}{4\sigma\tau}, \tag{3.28}$$
$$\hat{\mu} = \frac{4\sigma}{w I_0}\frac{w}{d_0}\frac{a_1 C_{pl}}{h_{lv}} 2\phi_l\left(1 - \phi_l\right)\Delta T. \tag{3.29}$$

In the above equations, w is the interfacial area thickness, usually equal to the grid spacing, σ is the surface tension. The integral I_0 is equal to a constant $2\sqrt{2}/3$, and the thermal capillary length is:
$$d_0 = \frac{\sigma T_s \rho_v C_{pv}\left(1 - \rho_v/\rho_l\right)}{\left(\rho_v h_{lv}\right)^2}. \tag{3.30}$$

The relaxation time (τ) is the time scale governing the transformation at mesoscale. The value of the relaxation time is derived from the asymptotic analysis of the conservation equations (for the temperature far from the critical temperature):

$$\tau = \frac{w}{d_0}\frac{w^2}{D_l}a_2. \tag{3.31}$$

The constants in the above equations are $a_1 = 1/\sqrt{2}$, $a_1 = 5/\left(6\sqrt{2}\right)$, and $D_l = \lambda_l/\left(C_{pl}\rho_l\right)$.

Substituting the relaxation time (Eq. 3.31), the mobility coefficient (Eq. 3.28) and the transformation potential (Eq. 3.29) into the mass flux equation (Eq. 3.27), and using the expression for the gradient of the order parameter (Eq. 3.32) yields to the general expression for the phase change mass flux (Eq. 3.33):

$$\left|\Delta\phi_l\right| = \frac{\sqrt{2}\phi_l\left(1-\phi_l\right)}{w}. \tag{3.32}$$

$$\dot{m}_l = \rho\frac{6\sqrt{2}}{5}\frac{D_l}{w}\frac{C_{pl}}{h_{lv}}\Delta T\left|\Delta\phi_l\right|. \tag{3.33}$$

This latter expression is the condensation mass transfer for the interfacial cells in the computational domain.

3.2 Model development for phase change phenomena

The development of phase change models requires the understanding of the possibilities and limitations of the VOF method and the phenomenon itself. The literature review (Section 1.3.2) and the study of the FLUENT software led to the development of four independent models to calculate the heat and mass transfer coefficient:

1. Lee numerical iteration technique [78];
2. Surface renewal theory correlation [72];
3. Direct solution of the heat flux balance equation;
4. Phase field theory based equation [84].

The next sections introduce the background of the models. The last subsection contains information about the additional numerical tools necessary for the implementation into FLUENT.

The volumetric mass transfer rate is calculated for the phase change process ($\dot{m}$). The mass transfer rate is added as a source in the vapor continuity equation (Eq. 1.54), the source of the liquid continuity equation is the negative value of the vapor source ($-\dot{m}$). The source in the energy equation (Eq. 1.56) is calculated from the latent heat and the mass transfer rate ($Q = -\dot{m}h_{lv}$).

3.2.1 Lee numerical iteration technique

The Lee model [78] imposes a boundary condition at the interface that the temperature is at the saturation value. In other words, a mass source is calculated if two conditions met:

- if the corresponding cell contains an interface, *i.e.* the void fraction is not equal neither to one nor zero, and
- the temperature of the corresponding cell differs from the saturation temperature.

If the above conditions are true, the vapor mass source is calculated from the relaxation factor (r), the void fraction (ϵ), the density (ρ), the cell temperature (T_{cell}) and the saturation temperature (T_s):

$$\dot{m}_v = \begin{cases} -r\epsilon_l\rho_l\dfrac{T_{cell}-T_s}{T_s} & \text{if} \quad T_{cell} \geq T_s, \\ -r\epsilon_v\rho_v\dfrac{T_{cell}-T_s}{T_s} & \text{if} \quad T_{cell} < T_s. \end{cases} \tag{3.34}$$

The r relaxation factor influences the final residual difference of the interfacial temperature from the saturation value and the speed of convergence. Low values of the relaxation factor cause unacceptable deviation from the saturation temperature in the interfacial cells, and high r values cause difficulties in the convergence of the solver. Therefore, the relaxation factor has to be tuned such that compromise is found between the final result and the convergence speed.

The main drawback of the method is the value of the relaxation time has to be tuned for each simulations independently. The long expected calculation time of the simulation limits the usability of the model, considering the trial-and-error procedure it requires.

The Lee numerical iteration model was implemented as the equation above.

3.2.2 Surface renewal theory correlation

The driving force of the condensation is the temperature difference from the saturation temperature of a liquid or surface which is adjacent to the vapor. A heat transfer coefficient (α) defines the transferred heat per unit temperature gradient, time and unit area of the surface or interface.

Knowing both the temperature difference between the interface (T_i) and the fluid (T_p) and the heat transfer coefficient (α_{ip}, $p = v, l$), the heat flux (q'') is calculated on both sides of the interface as Eq. 3.35:

$$q'' = \alpha_{ip}\left(T_i - T_p\right). \tag{3.35}$$

Applying this expression in the heat flux balance equation (Eq. 3.12), the heat transfer

coefficient directly calculates the phase change mass transfer (Eq. 3.36):

$$\dot{m}_{lv} = \frac{\alpha_{iv}(T_i - T_v) - \alpha_{il}(T_i - T_l)}{h_{lv}} |\nabla \epsilon| . \tag{3.36}$$

The comparison of the above equation to Eq. 3.15 results in Eq. 3.37 for the two phases ($p = v, l$):

$$\lambda_p \left(\frac{\mathrm{d}T}{\mathrm{d}z} \right) = \alpha_{ip} \left(T_i - T_p \right) . \tag{3.37}$$

The heat transfer equation (Eq. 3.36) is equivalent to the heat transfer calculation in the RELAP5 code (Eq. 1.19 in Section 1.2.1).

The main consequence of the above equation is that knowing the heat transfer coefficient provides the phase change mass transfer as well, without a need to calculate the temperature gradient. The approach is widely used in engineering applications (*e.g.* RELAP5); therefore, attempts were made to adopt this method in CFD calculations as well.

The surface renewal theory is based on the assumption that the heat transfer correlation in direct contact condensation depends on the turbulence level in the liquid, as turbulence eddies transport the heat away from the interface [72]. The theory suggests that wave formation between the liquid and the vapor, *i.e.* the turbulent eddies cause the presence of a bulk state at the interface, which affects the molecular diffusion into the liquid state. The renewal theory calculates the effect of the reduced interfacial shear and the eddy diffusivity distribution on heat and mass transfer by directly deriving them from the momentum transfer.

The renewal theory calculates the heat transfer coefficient from the renewal period, which is the ratio of the eddy velocity (V_t) and length scale (L_t). The Hughes-Duffey correlation [67] was implemented into the FLUENT software, as the correlation was used for the LAOKOON experiment in previous works [69]. In the equations, v is the kinematic viscosity, k_l is the turbulence kinetic energy and ϵ_l is the turbulence dissipation:

$$\alpha_{SR} = \frac{2}{\sqrt{\pi}} \lambda_l \left(\frac{\mu C_{pl}}{\lambda_l} \right)^{1/2} \left(\frac{1}{L_t} \right)^{1/2} \left(\frac{V_t}{v_l} \right)^{1/2} , \tag{3.38}$$

$$L_t = \left(\frac{v_l^3}{\epsilon} \right)^{1/4} , \tag{3.39}$$

$$V_t = (v_l \epsilon_l)^{1/4} . \tag{3.40}$$

The surface renewal correlation assumes that the gas is at saturation temperature; hence, the mass transfer depends on the temperature gradient in the liquid phase only. This boundary condition is exposed in the two-fluid models by setting the gas temperature to saturation and disregard the gas energy equation. This approach is not feasible for the VOF method, as only one energy equation is solved for the whole domain.

The surface renewal theory heat transfer was implemented into the FLUENT code as Eq. 3.38. The driving force was calculated as the temperature difference between the cell temperature and the saturation temperature. The gas side heat transfer was not considered; consequently, the mass transfer rate is (Eq. 3.41):

$$\dot{m}_v = \frac{\alpha_{SR}(T_{cell} - T_s)}{h_{lv}} |\nabla \epsilon|. \tag{3.41}$$

3.2.3 Direct solution of the heat flux balance equation

The heat flux balanced based model directly applies Eq. 3.42:

$$\dot{m}_{lv} = \frac{\lambda_v \nabla T_v \nabla \epsilon_v - \lambda_l \nabla T_l \nabla \epsilon_l}{h_{lv}}. \tag{3.42}$$

The model requires the temperature gradient at the liquid and the vapor side. The VOF method has one temperature field for the whole fluid domain; therefore, the cell based temperature gradient calculation does not distinguish between the liquid an the gas phases.

The condensation is driving the interface to the saturation temperature; hence, the subcooling of the gas phase is allowed in the calculation. The implementation of the heat flux balance equation requires the calculation of the temperature gradient on both sides of the interface. The discrete form of the Gauss theorem was applied to calculate the gradients.

Gradient of scalars

The gradient of an arbitrary scalar (ϕ) can be calculated by the discrete form of the Green–Gauss theorem [110]. The theorem states that the gradient of the scalar in the center of the cell is equal to the sum of the scalar on the faces multiplied with the face surface vector (A_f is a face area, $\vec{n}$ is the face normal vector) divided by the volume of the cell (V_c in Eq. 3.43):

$$\nabla \phi_c = \frac{1}{V_c} \sum_{\text{faces}} \phi_f A_f \vec{n}. \tag{3.43}$$

Gradient of the temperature

The temperature is represented by one scalar field in the VOF method; therefore, the build in gradient is equal for the two phases. The implemented gradient calculation splits the temperature field into two:

- for the vapor temperature gradient calculation the gas temperature is the temperature of the cell, whereas the liquid temperature is the saturation temperature;
- for the liquid temperature gradient calculation the liquid temperature is the temperature of the cell, whereas the gas temperature is the saturation temperature.

The two new temperature fields ($p = l, v$) are the weighted average of the above defined phase temperatures (Eq. 3.44):

$$T_{cell}^{p} = \epsilon_v \cdot T_v + \epsilon_l \cdot T_l. \tag{3.44}$$

Consequently, the new temperature field for the vapor temperature gradient calculation (Eq. 3.45):

$$T_{cell}^{v} = \epsilon_v \cdot T_{cell} + \epsilon_l \cdot T_s. \tag{3.45}$$

Similarly for the liquid temperature gradient calculation (Eq. 3.46):

$$T_{cell}^{l} = \epsilon_v \cdot T_s + \epsilon_l \cdot T_{cell}. \tag{3.46}$$

The gradients in the vapor and the liquid are the result of the discrete form of the Gauss-Green theorem, *i.e.* $\phi = T_{cell}^{v}$ and $\phi = T_{cell}^{l}$, respectively.

The heat flux balance equation was implemented in the FLUENT code by defining the two temperature fields, and calculating the $\nabla T_v \nabla \epsilon_v$ and $\nabla T_l \nabla \epsilon_l$ values in Eq. 3.42. The void fraction gradient, too, was calculated by the Gauss-Green theorem.

3.2.4 Phase field theory based equation

The phase change mass transfer rate from the phase field theory (Section 3.1.2) has a form:

$$\dot{m} = \frac{\alpha_{pf}(T_i - T_s)}{h_{lv}} |\nabla \epsilon|. \tag{3.47}$$

The equation has a similar form to the surface renewal theory correlation (Eq. 3.41); however, the concept behind the equation is different. The driving force of the above correlation is that the interface temperature differs from the saturation temperature. Yet, the interface temperature is approximated by the temperature of the cell. The α_{pf} coefficient (Eq. 3.48) is calculated from the liquid parameters ($D_l = \lambda/(C_p \rho)$) and the characteristic length of the interface (w):

$$\alpha_{pf} = \frac{6\sqrt{2}}{5} \frac{D_l \rho_l C_{pl}}{w}. \tag{3.48}$$

The phase field theory based coefficient was coded as the above equations. The characteristic length is the thickness of the interface, which is approximated by the height of the interface cell ($w = 2\delta x$).

The energy correction term, which accounts for the non-linearity effects of the condensation (Eq. 3.25) was as well implemented into the code as a source for the energy equation.

3.2.5 Comparison of the four models

Summarizing, the four implemented models are the followings:

1. Lee numerical iteration technique (3.2.1):

$$\dot{m}_v = -r\epsilon_p\rho_p\frac{T_{cell}-T_s}{T_s} \quad p = v,l;$$

2. Surface renewal theory correlation correlation (3.2.2):

$$\dot{m} = \frac{\alpha_{SR}(T_{cell}-T_s)}{h_{lv}}|\nabla\epsilon|;$$

3. Direct solution of the heat flux balance equation (3.2.3):

$$\dot{m}_{lv} = \frac{\lambda_v\nabla T_v\nabla\epsilon_v - \lambda_l\nabla T_l\nabla\epsilon_l}{h_{lv}};$$

4. Phase field theory based equation (3.2.4):

$$\dot{m} = \frac{\alpha_{pf}(T_{cell}-T_s)}{h_{lv}}|\nabla\epsilon|.$$

The driving force in the implemented models is either the temperature difference in the interface cell (model 1, 2 and 4), or the temperature gradient. The Lee model has equivalent form to models 2 and 3, where the coefficient is (Eq. 3.49):

$$\alpha_{Lee} = \frac{r\epsilon\rho}{T_s}\frac{h_{lv}}{\nabla|\epsilon|}. \tag{3.49}$$

For the surface renewal theory correlation and the phase field theory models, respectively:

$$\alpha_{SR} = \frac{2}{\sqrt{\pi}}\lambda_l\left(\frac{\mu C_{pl}}{\lambda_l}\right)^{1/2}\left(\frac{1}{L_t}\right)^{1/2}\left(\frac{V_t}{v_l}\right)^{1/2},,$$

$$\alpha_{pf} = \frac{6\sqrt{2}}{5}\frac{D_l\rho_l C_{pl}}{w}.$$

The four models have fundamentally different theories behind the equations; however, three models have equivalent forms. The following list summarizes the dependence factors for the mass transfer rate, the advantages and disadvantages of the models:

1. Lee numerical iteration technique (3.2.1):
   - Mass transfer rate depends on:
     - ◇ temperature difference,
     - ◇ relaxation number - tuning parameter.
   - Advantages:
     - ◇ straightforward implementation,

- ◇ well refined interface (2-3 cells) is not necessary, only preferable,
- ◇ tuning: usable for a wide range of application.

- Disadvantages:
  - ◇ tuning: many trial-and-error simulations are needed to find a proper r.

2. Surface renewal theory correlation (3.2.2):
   - Mass transfer rate depends on:
     - ◇ temperature difference,
     - ◇ void fraction gradient,
     - ◇ turbulence.
   - Advantages:
     - ◇ straightforward implementation.
   - Difficulties:
     - ◇ well refined interface is needed (2-3 cells),
     - ◇ dependence on turbulence at the interface: the VOF method is not designed for resolving the turbulence at the interface if the velocity of the phases has a significant difference,
     - ◇ the correlation depends on the turbulent length and velocity scale; therefore, the model constants vary, see *e.g.* Štrubelj *et al.* [66]. The length scale of the turbulence limits the range of applicability.
3. Direct solution of the heat flux balance equation (3.2.3):
   - Mass transfer rate depends on:
     - ◇ temperature gradient,
     - ◇ void fraction gradient.
   - Advantages:
     - ◇ direct calculation of the heat flux balance at the interface.
   - Difficulties:
     - ◇ well refined interface is needed (2-3 cells),
     - ◇ not applicable if the mesh does not resolve the linear thermal boundary layer,
     - ◇ implementation difficulties due to the gradient calculation.
4. Phase field theory based equation (3.2.4):
   - Mass transfer rate depends on:
     - ◇ temperature difference,
     - ◇ void fraction gradient.
   - Advantages:
     - ◇ straightforward implementation,
     - ◇ the mass transfer rate depends on fluid parameters only,

- general model, wide range of applicability.

- Difficulties:
  - well resolved interface region is needed (2-3 cells),

3.3 Additional information for the model implementation in FLUENT

The implemented condensation models require additional functions. These function help the convergence or provide the necessary parameters, initial and boundary conditions.

3.3.1 The smearing function

The applied interface reconstruction methods in the VOF method (for details see Chapter 5) provide a well refined interface, *i.e.* the thickness of the interface is 2-4 cells. The mass transfer rate is introduced in the interface cells; therefore, the mass and energy sources in these cells are high, whereas the other cells of the domain have zero sources. This causes convergence difficulties. Hardt and Wondra [88] suggested an approach, which smears the mass and heat transfer through the neighboring cells. The method was used by Magnini [89] in the FLUENT code. Kunkelman [94] implemented the smearing function into the OpenFOAM code for simulating a boiling phenomenon. He prohibited the mass transfer in the interfacial cells, and smeared the mass flux to the cells with zero or one void fraction.

Figure 3.7 shows the smearing of the original, sharp mass transfer rate ($\varphi_0 = \dot{m}$), which diffuses to the neighboring cells, requiring a definition of the additional scalar field (φ).

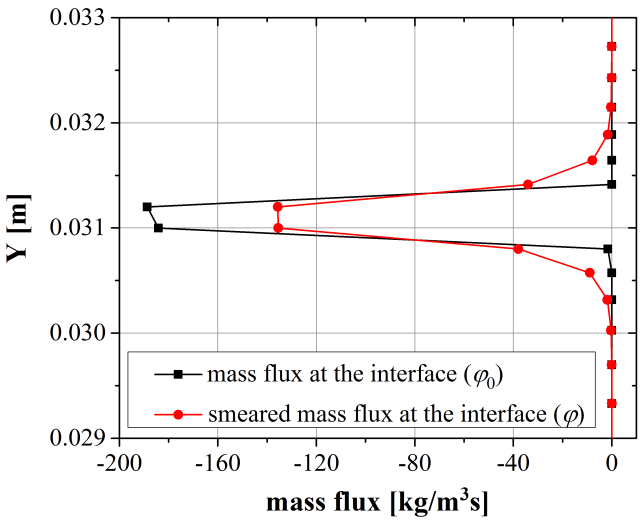

Figure 3.7: The original and the smeared mass flux at the interfacial cells

The source term distribution is calculated by solving a diffusion equation (Eq. 3.50) with the Neumann boundary condition (Eq. 3.51), which states that the flux is zero at the domain boundaries (Ω):

$$\nabla\varphi = \frac{1}{D}(\varphi - \varphi_0), \tag{3.50}$$

$$\vec{n}\nabla\varphi(\Omega) = 0. \tag{3.51}$$

The boundary condition ensures that the volumetric integral in the domain is equal for the smeared mass source and the original mass source. The D diffusion constant corresponds to the length scale of the smearing. The mass transfer source term (S_m) considers the mass appearance/disappearance at the vapor side and the liquid side of the interface by normalization factors (N_v and N_l, with the liquid and vapor void fraction ϵ):

$$S_m = N_v\epsilon_v\varphi - N_l\epsilon_l\varphi, \tag{3.52}$$

$$N_v = \frac{\int_\Omega \varphi \mathrm{d}\Omega}{\int_\Omega \epsilon_v\varphi \mathrm{d}\Omega}, \tag{3.53}$$

$$N_l = \frac{\int_\Omega \varphi \mathrm{d}\Omega}{\int_\Omega \epsilon_l\varphi \mathrm{d}\Omega}. \tag{3.54}$$

The source term of the energy conservation equation (S_e) contains two parts, the energy source due to phase change (S_e^p), which is shifted to the liquid side, and a correction term (S_e^c):

$$S_e = S_e^p + S_e^p = c, \tag{3.55}$$

$$S_e^p = -h_{lv}N_l^0\epsilon_l\varphi_0, \tag{3.56}$$

$$N_l^0 = \frac{\int_\Omega \varphi_0 \mathrm{d}\Omega}{\int_\Omega \epsilon_l\varphi_0 \mathrm{d}\Omega}. \tag{3.57}$$

$$S_e^c = \left(N_v\epsilon_v C_{pl} - N_l\epsilon_l C_{pl}\right) T\varphi. \tag{3.58}$$

The correction factor accounts for the decreased enthalpy flux due to the decreased mass flux in the phase change region.

The implementation of the smearing function is introduced in Section 3.4.

Calculation of the void fraction gradient

The void fraction gradient ($\nabla\epsilon$) on an arbitrary mesh can be calculated by the discrete form of the Green–Gauss theorem [110]. It states that the gradient of the scalar in the center of the cell is equal to the sum of the scalar on the faces multiplied with the face surface vector

(A_f is a face area, $\vec{n}$ is the face normal vector) divided by the volume of the cell (V_c):

$$\nabla \epsilon_c = \frac{1}{V_c} \sum_{\text{faces}} \epsilon_f A_f \vec{n}. \tag{3.59}$$

The above equation was implemented into FLUENT and was used instead of the built-in gradient functions.

Built-in limitations of the calculation

The implemented functions have limitations to avoid the numerical diffusion of the mass transfer rate to the bulk fluid regions. To restrict the mass transfer to the interface region, the following limitations are built in the functions:

- $\nabla \epsilon = 0$ if $\nabla \epsilon < 10^{-5}$;
- the mass transfer rate is not calculated in cells with $|T_{cell} - T_s| < 10^{-5}$ or $|\nabla \epsilon| < 1$;
- the mass transfer rate is not calculated in full vapor ($\epsilon_v = 1$) or full liquid cells ($\epsilon_v = 0$).

Calculation of the latent heat

The latent heat is calculated from the saturation temperature. The polynomial function (Eq. 3.60) is used, which was derived using a saturation temperature–latent heat table (Table 3.1 [104]):

$$h_{lv} = 1000 \cdot \left(710.114 + 9.543 \cdot T_s - 0.01461 \cdot T_s^2\right). \tag{3.60}$$

Table 3.1: Saturation temperature–latent heat table [104]

T_s [K]	373.15	400	430	460	490	520	550	580	610	647.3
h_{lv} [kJ/kg]	2256.7	2183	2092.8	1990.4	1871.5	1731.0	1562.6	1350.3	1064.2	0.0

3.4 The implementation

The FLUENT software was written in the C computational language. It has user defined functions (UDF), which are powerful tools to customize the simulations and to enhance the standard features of the software [111]. The UDFs are C functions, which are dynamically loaded with the solver. The `DEFINE` macros define the UDFs, which are coded by using additional macros provided by ANSYS. These macros and functions access the solver variables.

The FLUENT software stores additional variables, if user defined memories (UDM) are loaded. These variables are accessible for other macros and for post-processing. The user defined scalar (UDS) is a tool to define a scalar field in the calculation domain, which will be solved together with the other scalar equations.

The implementation of the condensation models, as well the customization of the simulations described in Chapter 5 required several C functions and built-in macros. The following `DEFINE` macros were used:

- `DEFINE_INIT`: to initialize the flow field;
- `DEFINE_PROFILE`: to calculate the inlet velocity profile, the void fraction profile at the inlet and outlet and the outlet pressure profile;
- `DEFINE_ADJUST`: to calculate the integrals (normalization factors for the smearing function), calculating and saving the void fraction gradient;
- `DEFINE_DIFFUSIVITY`: to define the diffusivity of the smearing function;
- `DEFINE_SOURCE`: calculate and pass the source for the vapor and liquid mass, the energy and the smearing function equations.

Figure 3.8 shows the calculation steps in the FLUENT pressure based segregated software. The calling sequence of the UDFs is indicated.

The smearing function was implemented as a user defined scalar transport equation [111]. FLUENT solves the transport equation (Eq. 3.61) for an arbitrary scalar (ϕ) in a same way as for other scalars *e.g.* for species mass fraction:

$$\frac{\partial}{\partial t}\left(\rho\phi\right) + \nabla\left(\rho\vec{u}\phi - \Gamma\nabla\phi\right) = S_\phi. \tag{3.61}$$

The diffusion coefficient (Γ) and the mass source (S_ϕ) has to be provided by the user. The diffusion is defined in a mixture, so the density and the velocity are the mixture values. To implement the smearing function (Eq. 3.50), the inlet diffusion, the flux function and the unsteady function are switched off. The diffusion is set to $\Gamma = D$, and the source is $S_\phi = \varphi - \varphi_0$. Consequently, the UDS is equivalent to Eq. 3.50:

$$D\nabla\varphi = (\varphi - \varphi_0).$$

The implemented C functions are in one source file, and the organization of the functions is the following:

- Definition of global variables:
  - ◇ normalization factors for the smearing function, (N_v, N_l and N_l^0);
  - ◇ Saturation temperature and latent heat of evaporation;
  - ◇ SMEAR: to be set to 1, if the smearing function is applied, and it is 0 otherwise;
  - ◇ COND: to choose the condensation model (1 = Lee model, 2 = surface renewal model, 3 = heat flux balance equation, 4 = phase field theory).
- Initialization of the flow field;
- Boundary conditions:
  - ◇ Velocity, void initial conditions, according to the setup solved;
  - ◇ Pressure outlet: outflow boundary condition, *i.e.* the boundary profile is copied from the adjacent cells;

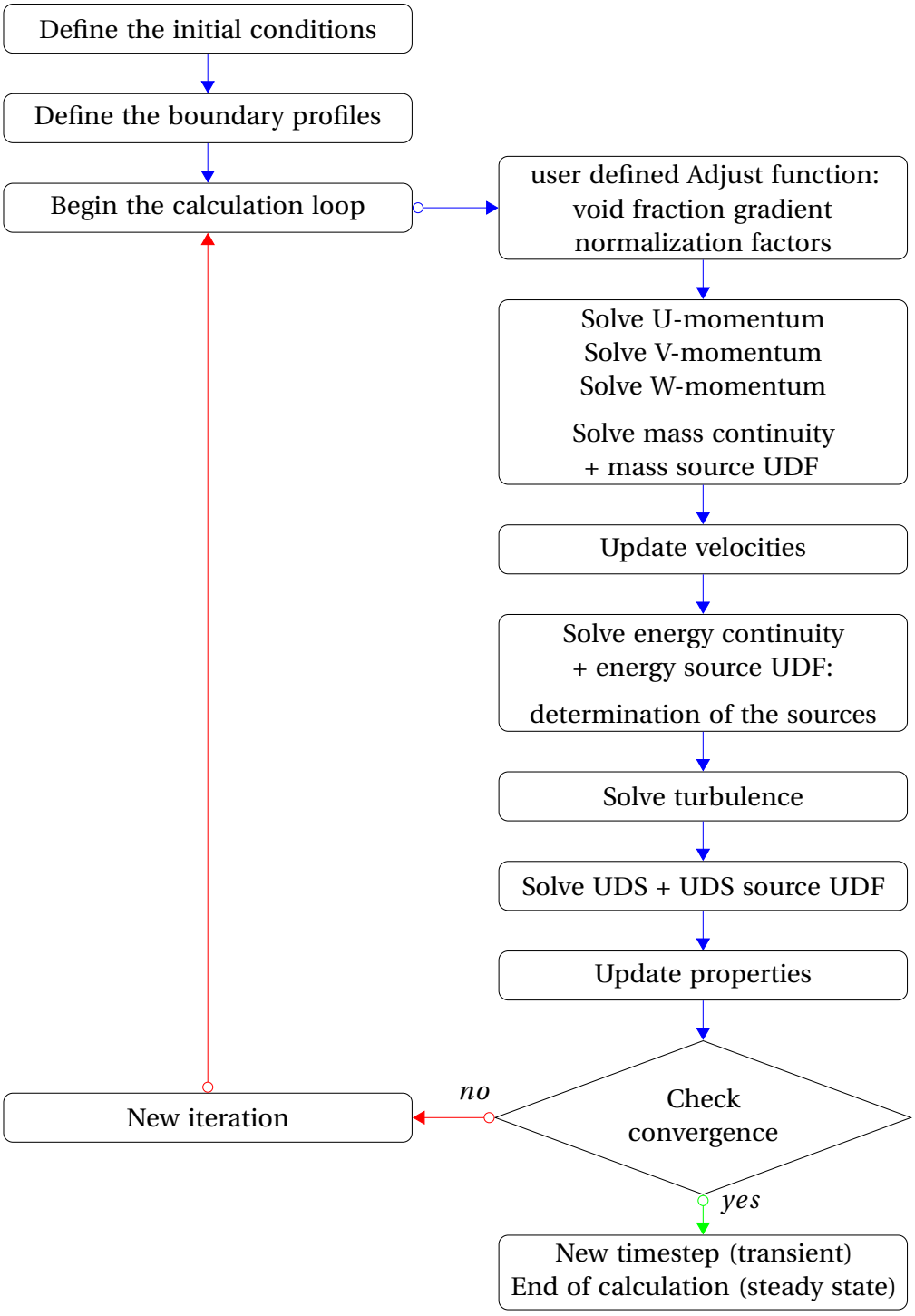

Figure 3.8: Solution procedure for the FLUENT solver with the implemented user define functions (UDF) and user defined scalar (UDS)

- Adjust:
  - ◇ Calculation of the magnitude of the void fraction gradient for all cells, and storing in UDM;
  - ◇ Calculation of the latent heat, and storing in global variable;
  - ◇ Calculation of radial coordinates, and storing in UDMs for postprocessing (for pipes only);
  - ◇ Calculation of the integrals for the normalization factors (Eq. 3.53, 3.54 and 3.57), and storing them in global variables;
- Diffusivity for the UDS: constant variable, the diffusivity for the smearing function;
- Definition of the sources:
  - ◇ Vapor mass source: copied from UDM;
  - ◇ Liquid: copied from UDM;
  - ◇ Energy: the sources are calculated in this function. The mass transfer rate calculation is done by a function, which is called according to the COND variable:
    - ∗ COND = 1: Lee numerical iteration (Eq. 3.34);
    - ∗ COND = 2: surface renewal (Eq. 3.38-3.41)
    - ∗ COND = 3: heat flux balance (Section 3.2.3)
    - ∗ COND = 4: phase field theory (Eq. 3.47-3.48)

    The smeared version of the mass source is passed to the mass equations, if SMEAR is equal to 1. The temperature difference from saturation, the mass transfer rate, the smeared mass transfer rate for liquid and vapor, the energy transfer rate, and the energy correction factor is stored for post-processing.
  - ◇ UDS source: the mass flux rate minus the UDS from the previous time step (right hand side of Eq. 3.4).

The above functions are applicable for two or three-dimensional flow fields, and for serial and parallel solvers without any changes [111]. The equations are solved implicitly, apart from the VOF equation, which is solved explicitly in transient calculations. The source terms are calculated in the energy source function, because the calculation in the mass source functions caused convergence difficulties and numerical error in the FLUENT solver. Chapter 5 contains the details on validation of the models.

4 Results with the RELAP5 code

This chapter contains the description of the implementation of the model, which was developed in Chapter 2, into the RELAP5 code. Section 4.1 describes the modification of the RELAP5 code; moreover, the validation of the RELAP5 implementation through the MATLAB code. Section 4.2 contains the calculation results for the Invert Edward Pipe Experiment (Section 1.4.1). Calculations were done by the unmodified RELAP5 code, TRACE, and the modified RELAP5 code. All calculations were compared to experimental results. Section 4.3 contains the calculations for the COSMEA facility. Finally, the last section of this chapter provides the conclusion on the RELAP5 calculations.

4.1 Modification of the RELAP5 /mod3.3 code

The RELAP5 code calculates the mass and heat transfer for condensation processes. The heat transfer coefficient for condensation in horizontal pipes is calculated in the CONDEN subroutine, and it is affecting the mass transfer near the wall (Section 1.2.1, Eq. 1.21). The code applies the horizontal condensation correlation only if the pipe is horizontal - the vertical condensation correlations are used with any inclination angle.

The horizontal condensation model of RELAP5 is based on the Nusselt theory, similarly to the model described in the Chapter 2; therefore, the implementation of the new model is convenient. The application range of the horizontal condensation model was extended to slightly inclined horizontal pipes until the value of 0.5 radian (equivalent to 2.9°) inclination from the horizontal.

4.1.1 The RELAP5 /mod3.3 condensation model for horizontal pipes

The RELAP5 condensation model for horizontal pipes considers stratified flow field with laminar film condensation on the wall. The heat transfer coefficient correlation is based on the classical Nusselt formula [23], with a modification of Chato [21]. The correlation (Eq. 4.1) contains a multiplicative factor (F_{Ch}), which corrects the original Nusselt correlation with the effect of the thicker water flume at the bottom of the tube. The Chato correlation defines

a constant value of $F_{Ch} = 0.296$. For more details, I refer to the RELAP5/mod.3.3 manual [10]:

$$\alpha_{RELAP} = F_{Ch}\left[\frac{\rho_l(\rho_l-\rho_v)g h_{lv}\lambda_l^3}{2\mu_L(T_s-T_w)R}\right]^{1/4} = F_{Ch}\cdot C^{1/4}. \tag{4.1}$$

4.1.2 Modifications of the RELAP5/mod3.3 condensation model

The new condensation model was implemented into the RELAP5 code with two simplifications. The iteration process was dispensed during the calculation of the stratification angle, because it would lead to complications in the iteration processes of the solver of RELAP5. The discarding is justified, because the liquid fraction of the upper part is negligible compared to the bottom part (Section 2.2, Eq. 2.9). The second simplification refers to the bottom heat transfer coefficient; thus, the implementation of the model into the RELAP5 code was limited to the calculation of the upper heat transfer coefficient. The MATLAB calculations showed that the error introduced from both modifications stays in an acceptable error limit.

The C term in the Chato correlation (Eq. 4.1) contains the fluid properties and geometrical parameters. The expression of the film heat transfer coefficient (Eq. 2.57) is rearranged (Eq. 4.2) by the C parameter:

$$\alpha = \frac{1}{2^{1/4}}C^{1/4}(\cos\theta)^{1/4}\frac{2}{\pi}\int_0^{\Phi_{strat}}\left[\frac{\sin\phi}{\phi}\right]^{1/4}\mathrm{d}\phi. \tag{4.2}$$

The C factor and the inner wall temperature is calculated by RELAP5; therefore, the iteration process for the heat transfer coefficient calculation is not necessary.

The integral in the correlation (Eq. 4.2) is calculated by a second term polynomial fitting (Eq. 4.3):

$$F \approx -0.102 + 0.9017\Phi_{strat} - 0.0257\Phi_{strat}^2. \tag{4.3}$$

With the assumptions above, the implementation of the model into RELAP5 is reduced into two equations: the calculation of the stratification angle (Eq. 2.9) and the calculation of the F factor (Eq. 4.3).

4.1.3 Verification of the modified RELAP5/mod3.3 code

The verification of the modified RELAP5 code was done through a comparison with the MATLAB code calculations. Figure 4.1 shows the effect of the simplification. Sample data sets showing the behavior of the modified RELAP5 model were picked from transient INVEP simulations. The instantaneous conditions found in a selected cell from the INVEP pipe model were sent to the MATLAB code for both the full and the simplified models. The resulting heat transfer coefficients were compared to each other and with those predicted by the extended RELAP5. The MATLAB calculations for the simplified calculation resulted in a heat transfer coefficient falling into an error band of 1%.

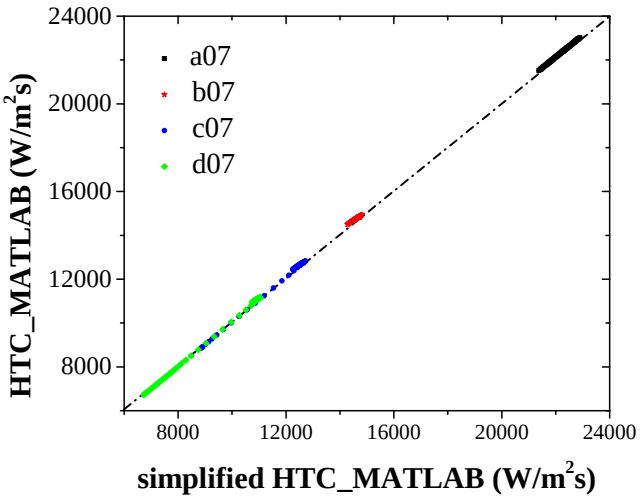

Figure 4.1: Effect of the simplification compared to the original MATLAB calculation. The dashed line is the 45°line, which represents the equal values.

Figure 4.2 shows the comparison between the MATLAB and the RELAP5 heat transfer coefficient values. The MATLAB calculations had the same initial conditions as the parameters of a node in the RELAP5 calculation. The pressure varied between the values of 5–70 bars, the void fraction varied between the values of 0.3–1; and 2400 data points were used to prepare the graph. The 45° line represents equal values for the two calculations. The dashed lines represent the boundaries of all of the data points. The maximum deviation between the two calculated values is 5.6%, but most of the data are in a 2–4% error range.

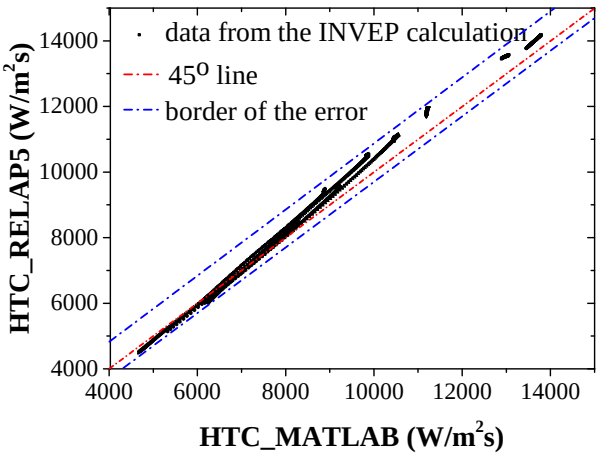

Figure 4.2: Verification of the modified RELAP5 condensation model with the MATLAB calculation

The deviation between the two calculated values is originated from the difference between the calculation of the material properties in RELAP5 and the MATLAB code. The RELAP5 code uses a new thermodynamically consistent set of steam tables, based in the IAPWS

formulation [10]. During the MATLAB calculation, a simplified correlation between the pressure and the material properties was used. The agreement between the two values is worse for higher heat transfer coefficient values; this range represents lower pressures, where the deviation of the material property calculation is higher.

4.2 Calculation results with the INVEP facility

Simulations of the INVEP experiments (Section 1.4.1) were done by two best-estimate thermal-hydraulic system codes TRACE and RELAP5, using the same nodalization. The experimental results and the simulations were compared for different initial conditions.

4.2.1 The model of the INVEP facility with RELAP5

Figure 4.3 shows the nodalization of the INVEP facility. The pressurizer, the pipe system, the valve, the condensation rod, and the cooling water tank (secondary side) were simulated. The pressurizer wall was modeled as a heat structure to represent the heat losses and the stored heat in the metal. A heat structure represented the 2 mm thick wall between the pipe component representing the condensation pipe and the water pool to ensure the heat transfer between the two sides.

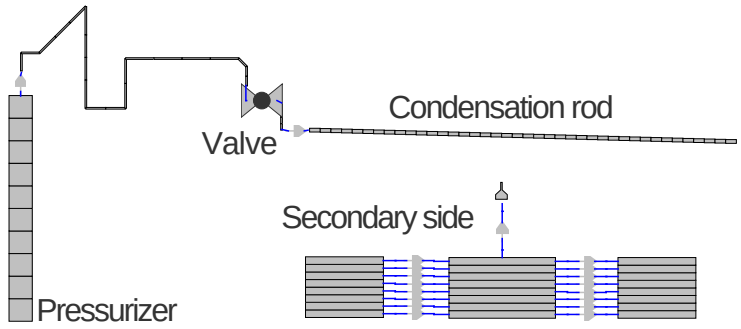

Figure 4.3: RELAP5 model of the INVEP facility

The cooling pool was simulated by three vertical pipes with eight nodes, which were connected horizontally by single junctions. The choice of the parallel pipe components ensured that cross flow and natural convection can occur in the tank during the transient. The heat structure of the condensation pipe was connected to the third node of the middle vertical pipe of this pool model. The condensation pipe had forty nodes. The default heat transfer correlation package was used for the wall heat structure model. The pressurizer had ten vertical nodes. The initial water level in the pipe was set by the void fraction values. The pressurizer heat structure had a convective boundary condition at the inner surface. The heat transfer of the outer surface was controlled by general tables.

The friction factors for the junctions were calculated using the tables of Ref. [112]. Twenty second long steady state calculations were done with a closed valve to acquire proper initial conditions for the transient calculations.

4.2.2 Analysis of the RELAP5 and TRACE heat transfer modeling

Sixteen experiments were calculated for four pressurizer pressures and six initial pipe pressures (Table 1.4). The *A* series correspond to the initial pressurizer pressure of 10 bars, the *B* to 30 bars, the *C* to 50 bars, and the *D* series to 70 bars. The *A*07, *B*07, *C*11 and the *D*07 experiment contained no non-condensable gas; the condensation pipe was filled initially with air of different pressures for the other experiments.

The experiments started by opening the valve between the pipe and the pressurizer. The pressurizer had a higher pressure; consequently, steam entered the pipe, and condensed on the wall. The liquid drained towards the lower situated, closed end of the pipe. The water accumulated at the bottom, and the liquid level started to increase. The experiment finished, when the pipe was filled with liquid. The condensation process depended whether non-condensable gas was present. The simulated transient was different for the RELAP5 and the TRACE code, which highlights the differences between the two code heat transfer estimation.

The temporal variation of the calculation parameters (such as the heat transfer coefficient at the inner wall, the temperature, the mass transfer between the phases due to condensation, the non-condensable gas quality and the void fraction) indicated the evolution of the transient. Figure 4.4 shows the evolution of the normalized values in time for four examples. The *C* experiment series had 50 bars initial pressure in the pressurizer, *C*08 had 3 bars initial non-condensable gas pressure in the pipe, and *C*11 was evacuated. The calculations were done with RELAP5 and with TRACE, and the values were normalized.

The transient condensation process was divided into five (RELAP5—*C*08), four (RELAP5—*C*11 and TRACE—*C*08) or three (TRACE—*C*11) parts, which were clearly set by the sudden change of the corresponding parameters. The boundaries between the phases are indicated on Fig. 4.4 by capital letters (Table 4.1) and black vertical lines. The corresponding flow pattern is drawn on the figure for the condensation phases.

Table 4.1: Arrival times and changes of the heat transfer coefficient calculation in the TRACE and RELAP5 calculations

Sign	Definition	RL C08	RL C11	TR C08	TR C11
A [s]	Non-condensable front arrives	64.7	–	109.0	–
B [s]	Water front arrives	103.5	69.1	119.8	91.24
C [s]	$\epsilon = 0.3$	138.5	90.5	–	–
D [s]	$\epsilon = 0.1$	169.6	104.0	–	–
E [s]	$\epsilon = 0.85$	–	–	134.1	106.7

Figure 4.4 and Table 4.1 shows the data evolution for the middle node of the pipe. The condensation process is introduced through this node in the in four sections.

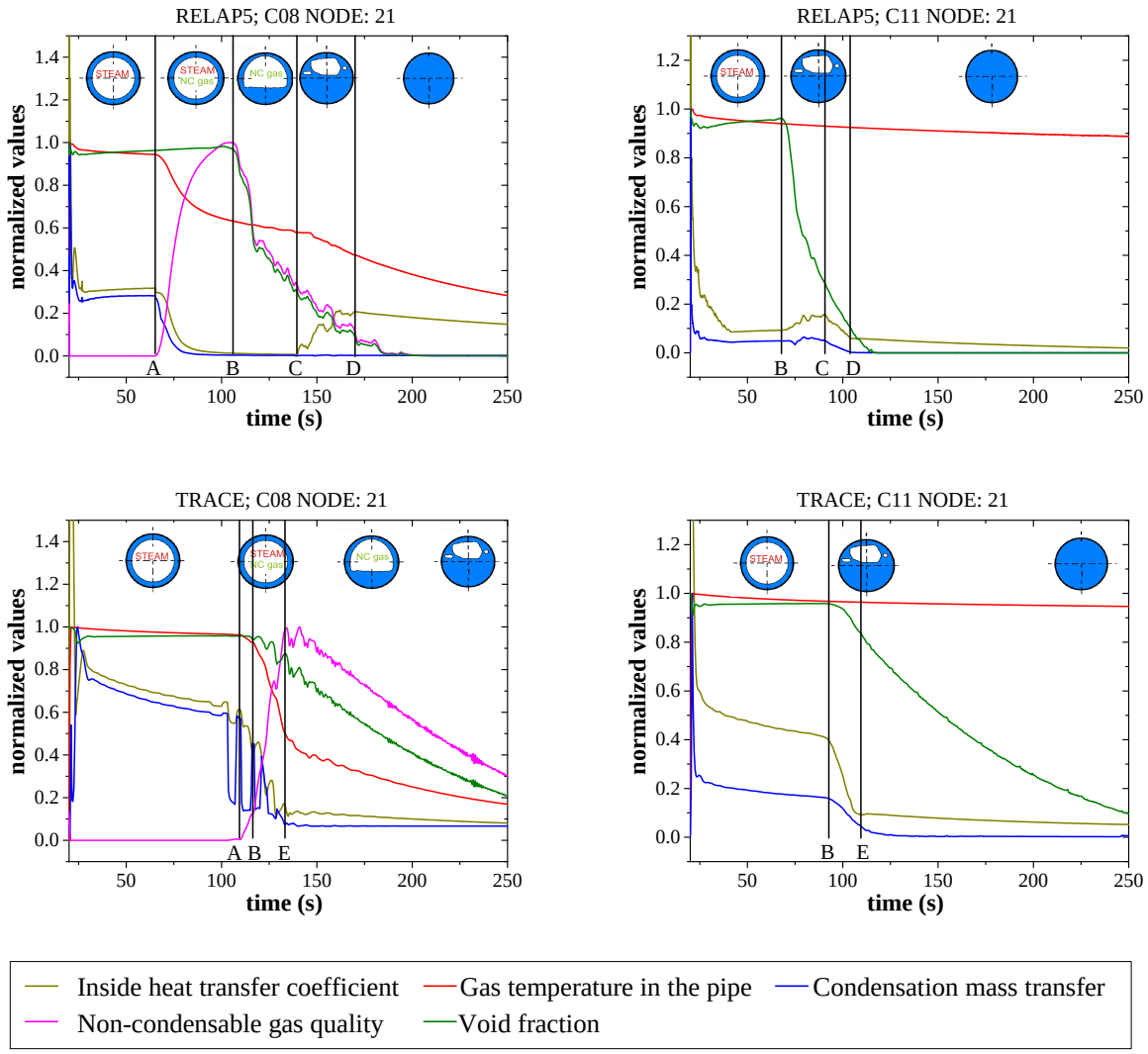

Figure 4.4: Temporal changes of the normalized variables for four calculations. The middle node of the condensation pipe, No. 21 was chosen to represent the condensation process over time. The drawings on the graphs help to follow the flow pattern change in the node.

1. The experiments started by opening the valve. The air was compressed and gathered at the closed end of the pipe. The condensation started on the pipe wall and the condensate flowed down to the lower end of the pipe. The non-condensable gas started to drift upwards, against the condensate flow direction. The phase change rate was determined by the condensation heat transfer coefficient in the beginning of the experiment in the middle of the pipe. The gas had saturation temperature, the void fraction remained nearly constant.
2. The point A defines the time when the front of the non-condensable bubble enters the node. The condensation model was switched to the non-condensable heat transfer

coefficient calculation. The inner heat transfer coefficient dropped significantly, similarly to the phase change rate. The temperature of the gas dropped below the saturation value. The void fraction does not change significantly. The RELAP5-*C*08 heat transfer coefficient was nearly zero.

3. The point B is the time, when the void fraction starts to decrease in the cell, *i.e.* when the condensate starts to fill the corresponding node. Consequently, the non-condensable gas mass decreased in the volume. The heat transfer coefficient increased in the RELAP5-*C*11 simulation, and it stabilized in the RELAP5-*C*08 simulation. The heat transfer coefficient decreased in the TRACE simulations.
4. After the void fraction started to decrease in the node (B), the RELAP5 and the TRACE codes switched to single phase heat transfer calculation.
   (a) RELAP5 code: the heat transfer model switches from the condensation heat transfer coefficient correlation to the single phase Dittus-Boelter correlation between the void fraction values of 0.3 - 0.1 (C and D points) (see Section 1.2.1). The *C*08 simulation showed an increased heat transfer coefficient between these values. The *C*11 had a decreased heat transfer coefficient. The single phase flow heat transfer coefficient changed with the temperature. The condensation stopped, and the node was filled with water.
   (b) TRACE: the heat transfer coefficient and the phase change rate decreased significantly, when the liquid front entered the cell. The heat transfer coefficient switches to the two-phase flow convection correlation between the void fraction values of 0.9 and 0.8 (see Section 1.2.2). When the void fraction was equal to 0.85 (E), the heat transfer coefficient became constant, and the phase change process stopped.

The RELAP5 code showed a faster condensation process. The ramp from the condensation to the convection heat transfer coefficient happened for higher void fraction values in the TRACE code; therefore, the heat transfer coefficient decreased faster then in the RELAP5 code. The non-condensable gas had a significant effect on the heat transfer, and it slowed down the condensation process.

Comparison with the experimental results

Figure 4.5 shows the comparison of the calculations and the experimental data for the *C*08 test. Four measurement points were selected, these are the pressure measurement at the closed end of the pipe, temperature measurements (T8 was 0.8L and T3 was 0.27L distance from the closed end), and two void fraction measurements (V7 was 0.6L and V3 was 0.27L distance from the closed end). The other experiments and measurement point followed the trends discussed in this section.

The data are plotted as a function of time, the sudden drop of the void fraction shows when the corresponding location is filled with liquid. The duration, until the change in the void fraction occurred, correlated with the transferred heat from the pipe to the secondary side,

i.e. with the heat transfer coefficient. The faster change in the void fraction data coincided with faster condensation process.

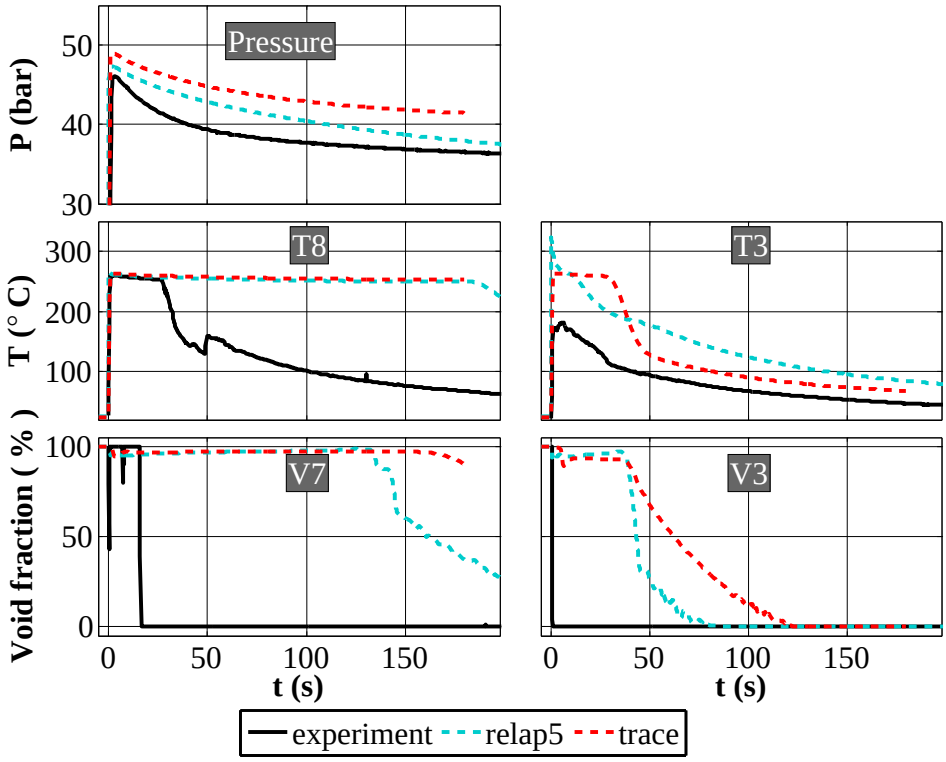

Figure 4.5: Comparison between the simulation and the measurement results of the INVEP setup

The condensation calculation of both RELAP and TRACE failed to reproduce the experimental results. The condensation process was significantly slower, and the higher temperature and pressure results imply that the transferred energy from the primary to the secondary side was not significant in the calculations. The condensation process was about ten times slower in the simulations than in the experiment. The condensation was slower in the TRACE simulation. The pressure results decreased in RELAP5 about the experimental value after 150 s, the TRACE pressure results showed about 15% deviation.

The condensate started to fill the pipe from the closed end towards the open end of the pipe. The water front arrival time was indicated by the sudden change in the void fraction; therefore, this time reflected the speed of the condensation. The water front pushed in front the non-condensable bubble, if the pipe was initially filled with air. The non-condensable gas was colder than the steam; therefore the temperature, colder than saturation indicated the arrival of the non-condensable bubble in the experiments and the calculations [96]. Figure 4.6 shows this processes for RELAP, TRACE and the experiment.

Figure 4.6.a shows the time of water front arrival. The effect of the non-condensable gas was significant for RELAP5; the condensation was twice faster, when no air was presented in the pipe. The TRACE calculations showed no difference.

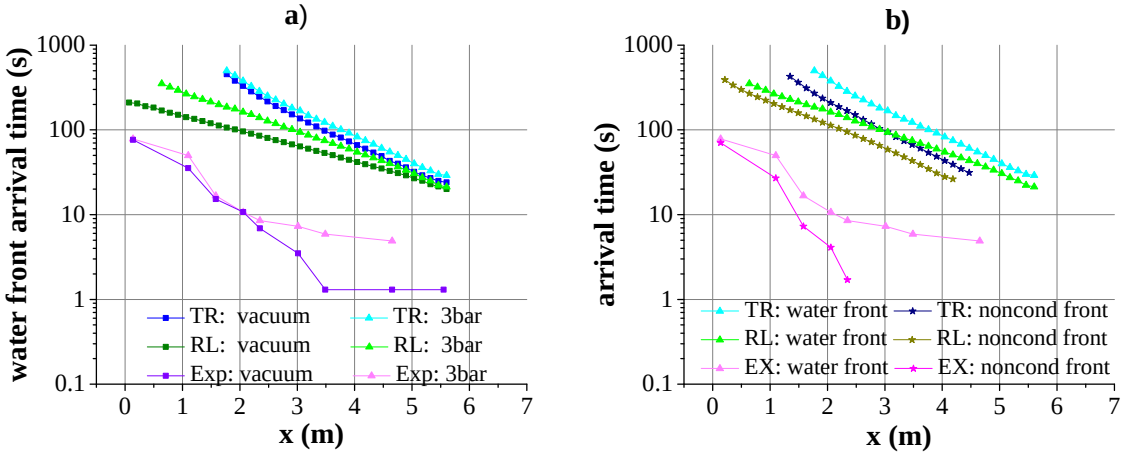

Figure 4.6: Movement of the air and the water fronts in the INVEP condensation pipe

Figure 4.6.b shows the movement of the air and the condensate along the pipe for the *C*08 experiment. The two fluids moved with the same speed in the calculations. The experiments had a faster condensation process, the two codes failed to reproduce the data.

Artificial increase of the heat transfer between the primary and secondary sides

Both the vacuum and the non-condensable simulations showed similar difficulties; nevertheless, the non-condensable gas influence was qualitatively captured (Fig. 4.6). The RELAP5 simulations were tested by the artificially increase of the heat structure between the two sides. Two approaches were used to enhance the heat transfer, the first approach increases the heat structure surface, while the second approach accounts for an increased heat transfer coefficient.

The heat structure surface is increased by setting the cylindrical length (CL), which represents the length of the heat structure. The default cylindrical length is equal to the length of the hydraulic node. Note that the increase of the heat structure had no effect on the geometry of the hydraulic element.

The cylindrical length was changed from the original 0.14 m value to the optimal value, which achieved the best agreement with the experiments for all initial conditions separately. The multiplication factor between the optimal and original cylindrical length is the CL factor.

The second approach was to increase the outer and inner heat transfer coefficient independently. The heat transfer coefficient–temperature correlation was derived from the original calculation, and a new correlation was implemented, which increased the original coefficient by a 3.5 linear multiplication factor. This factor was equal to the optimal CL factor for the *C*08 experiment.

Figure 4.7 shows the effect for the above described three enhanced heat transfer calculations in comparison to the original simulation and the experiment. The enhanced heat transfer

resulted in a faster condensation process in the pipe. The calculation with the optimal cylindrical length fitted on the experimental results for every location in the pipe over time.

The pressure data for the enhanced inner heat transfer coefficient followed the experimental results until about 50s, after it was smaller than in the experiment. The temperature and void fraction measurement showed a better results than the original calculation. The optimal agreement was not reached, as the multiplication factor was arbitrary chosen to be equal to the CL factor.

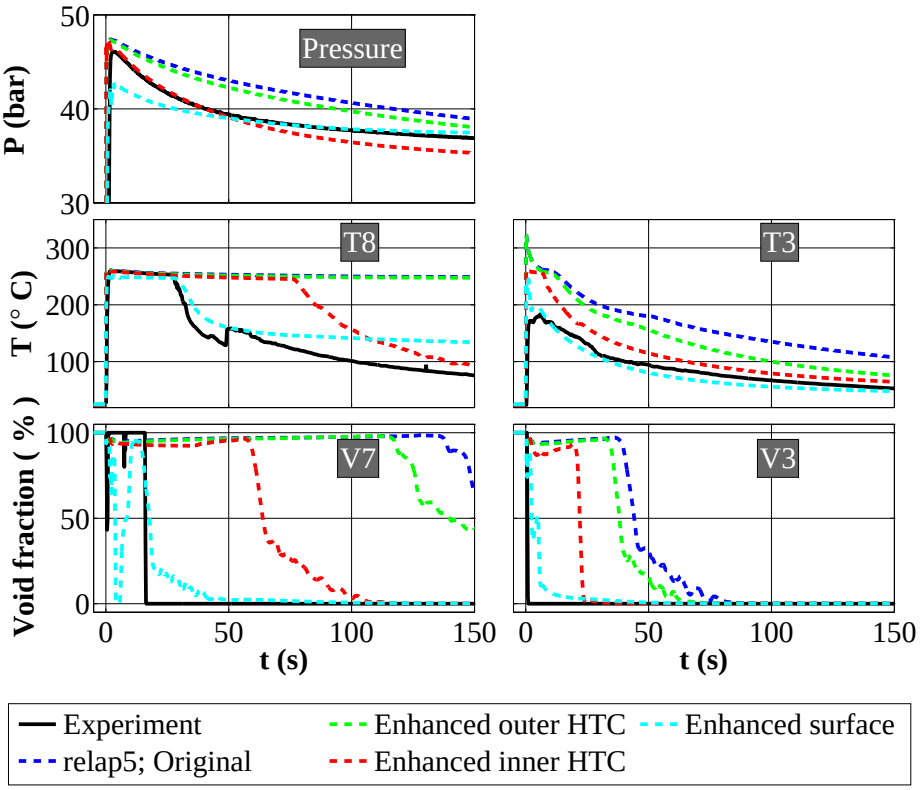

Figure 4.7: Effect of the enhanced cylindrical length in the RELAP5 simulation of the INVEP setup (HTC-heat transfer coefficient)

The results from the enhanced outer surface heat transfer coefficient differed significantly from the experimental data. The inner surface heat transfer coefficient had more significant effect.

The CL factor was defined for the 16 experiments (Fig. 4.8). The CL factor is interpreted as a necessary correction factor to the overall heat transfer. Figure 4.8 shows the CL factor as a function of the initial non-condensable gas mass in the pipe. The Figure suggests that the higher non-condensable gas mass causes a bigger deviation in the simulation.

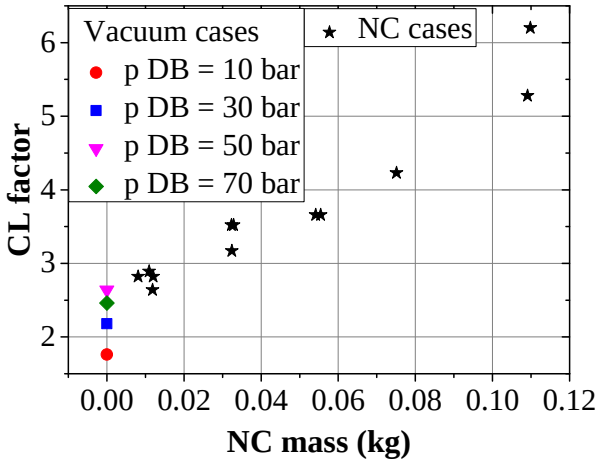

Figure 4.8: The CL factor according to the initial non-condensable mass in the pipe

4.2.3 Calculation with the modified RELAP5 code

The previous section showed that the linear enhancement of the heat transfer cannot eliminate the deficiencies of the heat transfer model in RELAP5, but the agreement between the calculation and experiment can be achieved by correcting the heat transfer alone. In conclusion, the heat transfer coefficient model of RELAP5 should be improved.

The RELAP5 condensation model was modified with the mechanistic model described in Chapter 2 and Section 4.1. The modification accounted for condensation without non-condensable gas; therefore, the INVEP vacuum experiments are presented here.

Figure 4.9 shows the progression of the experiment *B*07. The results of the experiment and the calculation with the original and the modified RELAP5 code are displayed for six time points. The water level (L), which is the length of the water column, was determined by the amount of transferred heat to the secondary side, *i.e.* the efficiency of the heat transfer was indicated by the speed of the raising water level in the pipe. The interface between a water and the vapor column was the point with 50% void fraction, which is indicated as vertical line on the figure.

The water level of the original RELAP5 calculation was significantly lower than in the experiment, demonstrating that the heat transfer between the secondary side and the condensation pipe was not efficient enough in the calculation. The modified RELAP5 code followed the experimental results significantly better. The water level was closer to the measured value than in the original RELAP5 calculation, which shows that the modified condensation model calculated a more efficient heat transfer process.

Figure 4.10 shows measured and calculated pressure data for the vacuum experiments. The solid lines show the pressure at the closed end of the pipe, the dashed lines show the pressure in the pressurizer, according to the time.

The pressure history of the experiment was characterized by a sudden pressurization in the

pipe after the valve opening. The pressure in the tank and the pipe equalized immediately after opening the valve in the high pressure experiments (*C* and *D*). In the lower pressure experiments the convergence was established slower, as the lower vapor density caused a smaller mass transfer from the vessel to the condensation pipe. The modified RELAP5 calculations were closer to the measured data, indicating the more efficient heat transfer process than the original simulations. For the initial low pressures, the calculation could not predict the discussed pressure decoupling between the pipe and the pressurizer at the beginning of the experiment, the pressure of the pipe jumped to the pressure of the tank after opening the valve immediately. For high pressures, the decoupling was not significant in the experiment, consequently the calculated values predicted the measured data better.

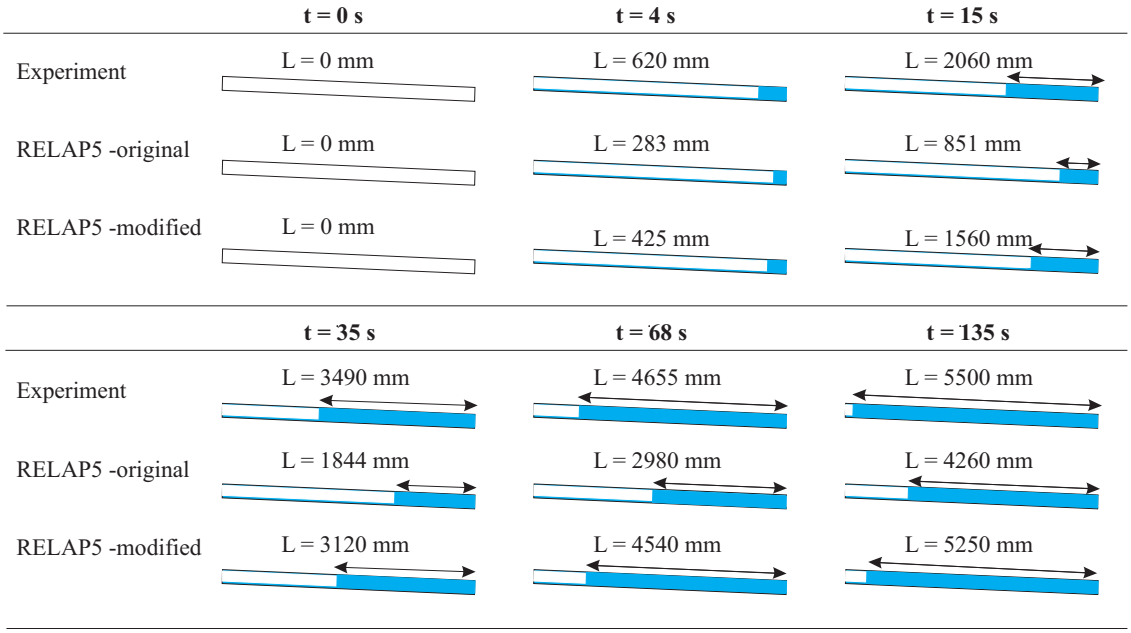

Figure 4.9: Experimental and calculated water levels for the b07 experiment

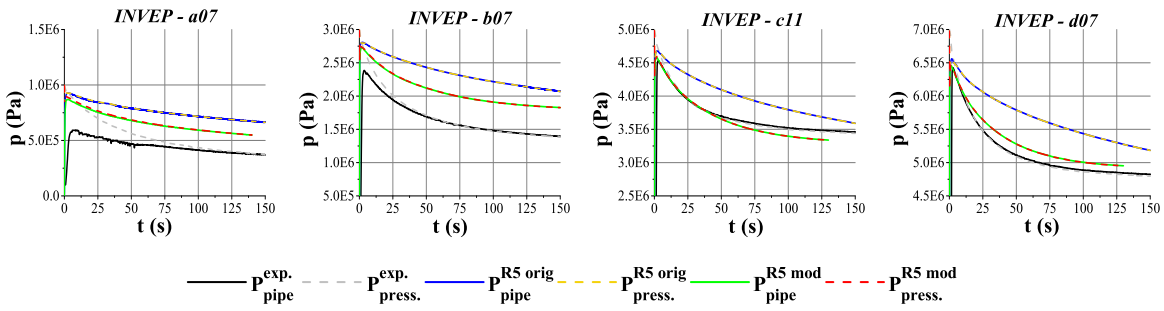

Figure 4.10: Measured and calculated pressure values at the closed end of the pipe (P_{pipe}) and in the pressurizer (P_{press})

Figure 4.11 shows the calculated and measured temperature data for the four experiments, at different locations along the pipe (T2, T5, T7). The plots shows that the modified RELAP5 code could predict the temperature data along the pipe for different locations, initial conditions and time points.

The temperature data showed a high and sudden increase at the beginning of the experiment. After a slow decrease of the temperature, a significant cooling happened as the condensate arrived to the corresponding location. The modified RELAP5 code showed the arrival of the condensate earlier than the original RELAP5 calculation, and the temperature drop was higher at the arrival of the liquid phase. The RELAP5 calculation predicted the temperature data well, a slight over-prediction was observed, especially at higher initial pressures.

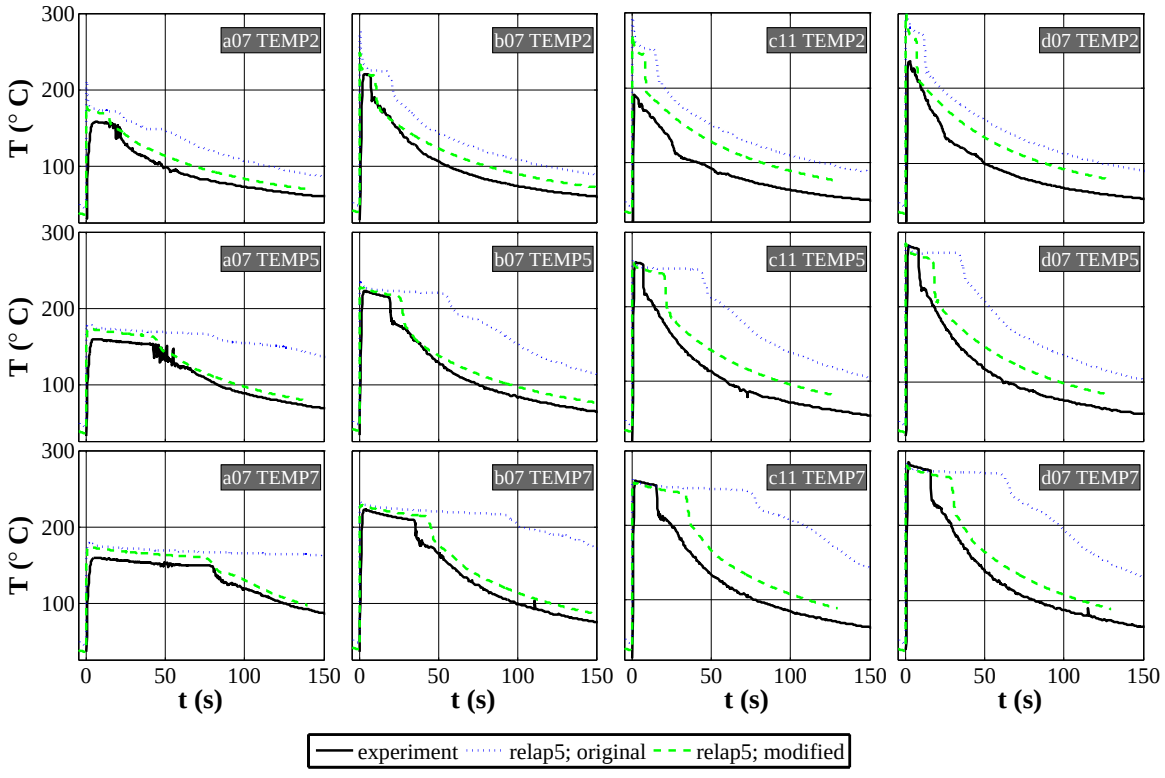

Figure 4.11: Measured and calculated temperature values for the four vacuum experiments at different locations along the condensation pipe

Figure 4.12 indicates, that the heat transfer coefficient changed significantly between the original and the modified RELAP5 calculation. The figure shows the heat transfer coefficient for the node No. 21. The opening of the valve caused a peak in the heat transfer coefficient, and the modified model had a higher value during the condensation process. The steam, therefore, condensed faster in the modified RELAP5 calculation.

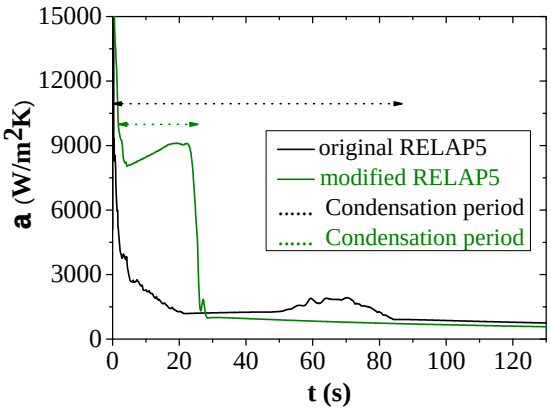

Figure 4.12: Change of the condensation heat transfer coefficient for the $C11$ calculation, in the middle of the pipe (Node 21)

4.2.4 Outlook - Considerations for the non-condensable gas

The modified condensation model did not affect the condensation heat transfer coefficient in presence of non-condensable gas. To demonstrate the effect of the non-condensable gas on the INVEP experimental process, further modifications were applied.

The Colburn-Hougen condensation correlation [24] was replaced with a geometrical model. I assumed that the air did not mix with the steam. The air bubble was compressed to the bottom of the pipe, and as the liquid column started to grow in the pipe, it pushed the air bubble forward. In such scenario, the Colburn-Hougen is not applicable, since these correlations assume a homogeneous mixture of the non-condensable gas and the steam.

Figure 4.13 shows the assumed geometry for a cross section of the pipe, when the non-condensable gas was present. The model considered three layers. The stratification angle defined the area of the steam layer, similarly to the previously introduced model.

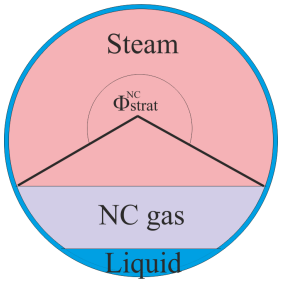

Figure 4.13: Assumed cross sectional flow pattern with the non-condensable in the gas phase

The same model (Section 4.1) was implemented for the non-condensable condensation correlation. The stratification angle was calculated by assuming the geometry on Fig. 4.13. The calculation considered this stratification angle to calculate the heat transfer coefficient (Eq. 4.2).

Figure 4.14 and Figure 4.15 show the results for four experimental conditions, for the pressure and the temperature results. The figures contain the experimental data, the original, the modified correlation calculation, and the modified correlation together with the modified non-condensable condensation heat transfer coefficient correlation.

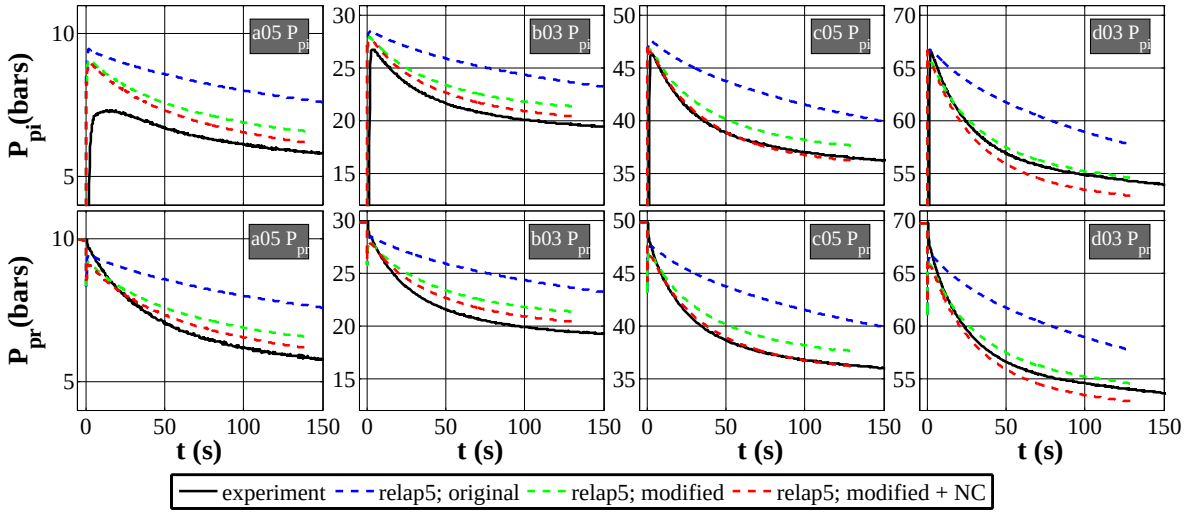

Figure 4.14: Experimental and calculated pressures for the INVEP *A*05, *B*03, *C*05 and *D*05

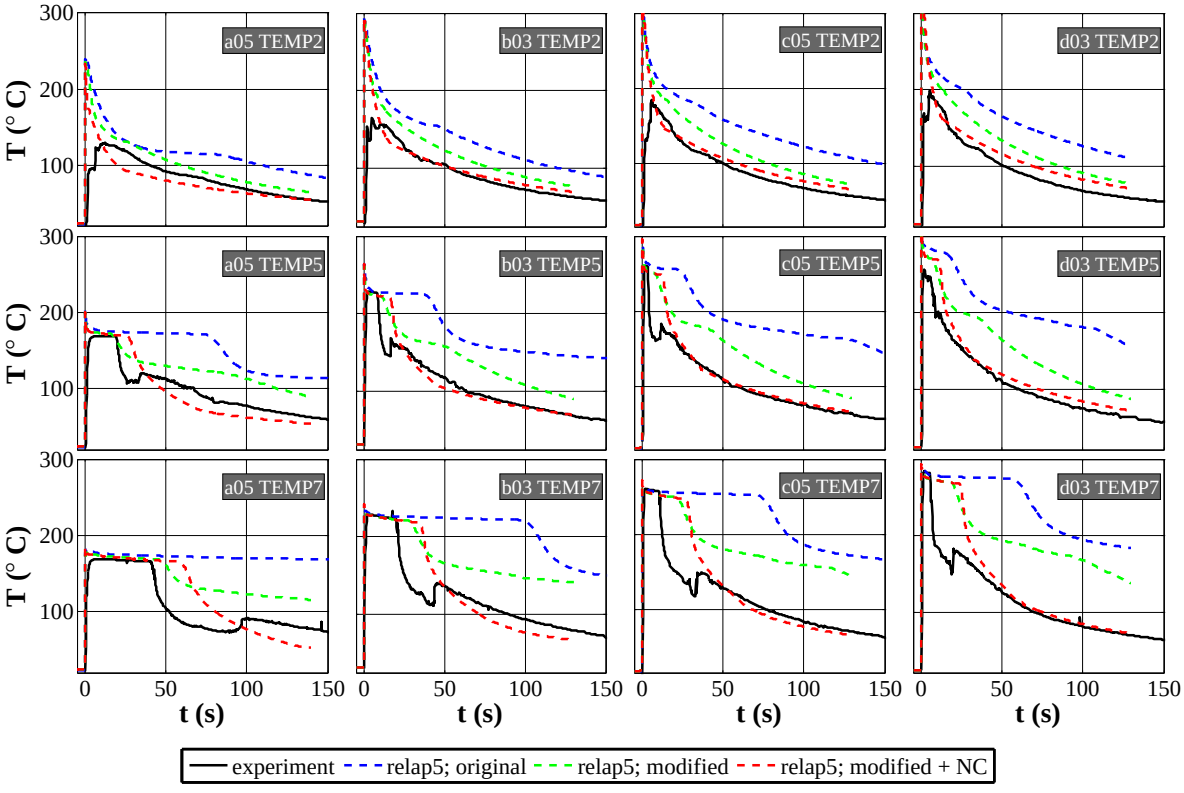

Figure 4.15: Experimental and calculated temperature data for the INVEP *A*05, *B*03, *C*05 and *D*05

The agreement between the calculation and the experiment improved significantly. The pressure data followed well the experimental results. The modified calculation for the non-condensable experiments fitted better to the temperature data than the calculation with the Colburn-Hougen correlation. The effect was pronounced in the temperature drop when the non-condensable front arrives. The new correlation caused a higher heat transfer to the secondary side; thus, the node cooled faster.

On the other hand, the pressure data did not show a significant improvement; however, the data improved comparing to the original RELAP5 calculations. The simulation predicted the pressure data well for the high pressure experiments (*C* and *D*), and resulted in a poorer agreement for the low pressures, especially for the pipe pressure. The pressure in the pipe and the pressurizer coupled fast in the simulation; however, in the experiment the equalization of the two pressures were slower. The RELAP5 code could not follow this phenomenon; consequently, it failed to reproduce the pressure results in the pipe for low pressures.

4.3 Calculation results with the COSMEA facility

The COSMEA facility (Section 1.4.3) was modeled with the modified RELAP5/mod3.3 code. The experiments were done without non-condensable gas; therefore, the heat transfer coefficient with non-condensable gas was not tested here.

4.3.1 The RELAP5 model of the COSMEA facility

The model of the COSMEA setup consisted of two pipes, which were connected by a heat structure. The heat structure is a 2.5 mm wall, made of stainless steel (Fig. 4.16). The condensation pipe was connected to an adiabatic inlet and outlet pipe. The inlet conditions were set by two time dependent junctions, which ensured the correct void fraction and mass flow for the steam–water mixture. A third time dependent junction was connected to the secondary side inlet. The outlet of both sides were connected to a time dependent volume through a single junction.

Table 4.2 shows the initial conditions for the RELAP5 calculations for the test matrix. The saturation temperature was calculated for the corresponding inlet pressure. The liquid and vapor were slightly subcooled. The adiabatic inlet pipe, therefore, showed phase change in the calculations.

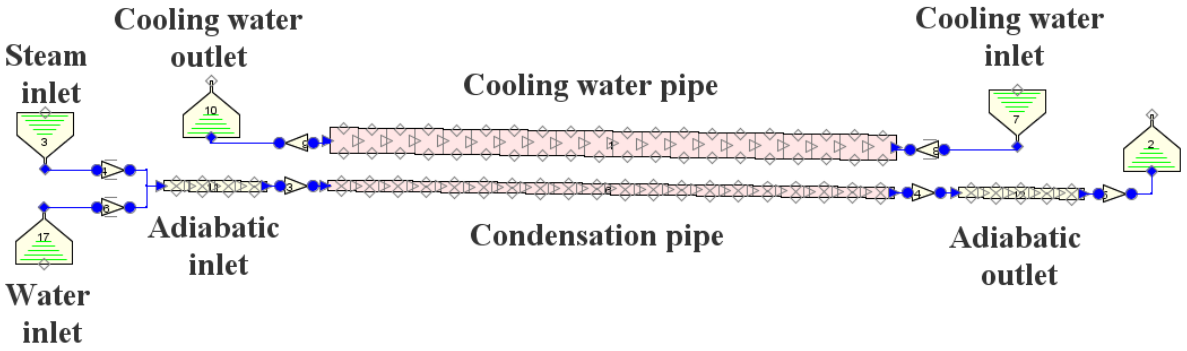

Figure 4.16: RELAP5 model for the COSMEA facility

Table 4.2: Input conditions for the RELAP5 calculation (COSMEA test matrix)

No.	P_{I1} [bars]	T_s [K]	$\dot{m}_v$ [kg/s]	T_v^{in} [K]	$\dot{m}_l$ [kg/s]	T_l^{in} [K]	P_{out} [bars]	P_{I2} [bars]	T_{I2} [K]	$\dot{m}_{I2}$ [kg/s]
51	5.0	425.35	0.087	425.2	-	–	5.0	3	311.65	15.7
52	5.0	425.25	0.064	425.1	0.041	424.7	5.0	3	311.65	14.3
151	15.2	472.07	0.256	471.8	-	–	15.0	5	311.85	29.6
152	15.1	471.88	0.206	471.7	0.050	467.4	15.0	5	311.65	27.5
153	15.1	471.76	0.152	471.6	0.102	471.0	15.0	4	311.65	25.7
154	15.1	471.82	0.103	471.6	0.151	471.6	15.0	4	311.75	23.4
251	25.4	497.86	0.406	497.6	-	–	25.0	4	310.65	19.1
252	25.3	497.76	0.334	497.5	0.072	493.6	25.0	4	310.75	18.8
253	25.2	497.59	0.270	497.4	0.138	496.8	25.0	4	310.65	17.5
254	25.2	497.46	0.195	497.3	0.209	497.2	25.0	3	310.65	16.1
255	25.2	497.50	0.124	497.4	0.272	497.8	25.1	3	310.65	14.9
451	45.5	531.19	0.605	530.9	-	–	45.0	4	311.55	25.3
452	45.4	531.18	0.523	530.9	0.091	526.1	45.0	4	310.55	23.9
453	45.4	531.07	0.428	530.8	0.180	529.6	45.0	4	310.65	23.1
454	45.4	531.07	0.342	530.8	0.266	530.6	45.1	4	310.65	22
455	45.5	531.21	0.250	531.0	0.356	531.5	45.3	4	310.25	20.3
456	45.4	531.10	0.202	530.9	0.398	531.7	45.2	4	310.55	19.1
651	65.7	554.67	0.801	554.4	-	–	65.0	5	312.65	29.6
652	65.5	554.49	0.684	554.3	0.117	549.9	64.9	5	312.05	28.5
653	65.4	554.45	0.568	554.2	0.238	552.7	65.0	4	313.15	27.9
654	65.2	554.17	0.434	554.0	0.360	553.8	64.8	4	312.95	26.7
655	65.4	554.36	0.343	554.1	0.462	554.5	65.1	4	312.75	25.4
656	65.7	554.76	0.247	554.5	0.559	555.1	65.5	4	312.65	23.3

4.3.2 Calculation results with the RELAP5 code

The RELAP5 code was run in a transient mode, until steady state conditions were reached. The results were compared to the experimental data for 23 different initial conditions.

Geißler *et al.* calculated the condensation rate in three different ways [101]. The first method used the pressure level in the outlet separation vessel together with the inlet mass flow, assuming that the level rise in the vessel corresponds to the condensation rate in the condensation pipe. Both the second and the third methods were based on the energy balance on the secondary side. The second method calculated the heat transfer from the temperature difference between the secondary side inlet and outlet. The third method used the amount of cooling water added to the secondary side to determine the power, which was needed to keep the facility in a steady state condition.

The steam, after entering the condensation pipe, condensed, and the condensate cooled below the saturation value. The three methods used the temperature data from the heat flux probe at the inner wall to account for the subcooling of the water. The thermocouples were 1095 m upstream from the outlet of the pipe; therefore, the condensation rate calculation from the experiments had a high uncertainty. The error was in a range of 20% for the 5 bars calculations, 30% for the 15 bars, 15-20% for the 25 bars, 15% for the 45 bars, and 15-25% for the 65 bars calculations. The error was higher for lower void fractions.

Figure 4.17 shows the comparison for the measured and simulated condensation rates for all the experiments. The condensation rate was an output of the RELAP5 calculation for all the nodes. The inlet adiabatic section had a condensation rate about 0.5% of the total value in the pipe, because of the initial subcooling of the water and steam. The outlet adiabatic section had a contribution of about 7-10% to the final condensation rate, because of the subcooling of the condensate.

The sum of the three parts were compared to the experimental results. The two data fitted for all the experimental results within the error bands. The agreement was best for medium void fractions. The highest difference, for the experiment E656, was 20%. Apart from the lowest and highest initial void fractions, the difference between the calculated and measures condensation rate values was in a range of 1–10%.

Figure 4.18 shows the comparison of heat flux data. The heat flux was taken from the RELAP5 output for the node at the same location as the heat flux probe in the experiment. The experimental heat flux was the average of the five heat flux probe values. The results agreed well, the highest difference was for the low void fraction and low pressure experiments (E51–21%, E52–20%, E153–15%, E154–26%, E255–22%, E456–12%, E656–10%). The absolute value of the heat flux is lower; therefore, the same absolute error corresponds to a higher relative error. For all the other experiments the difference between the experimental results and the simulated results was lower than the uncertainty of the experiment (8%).

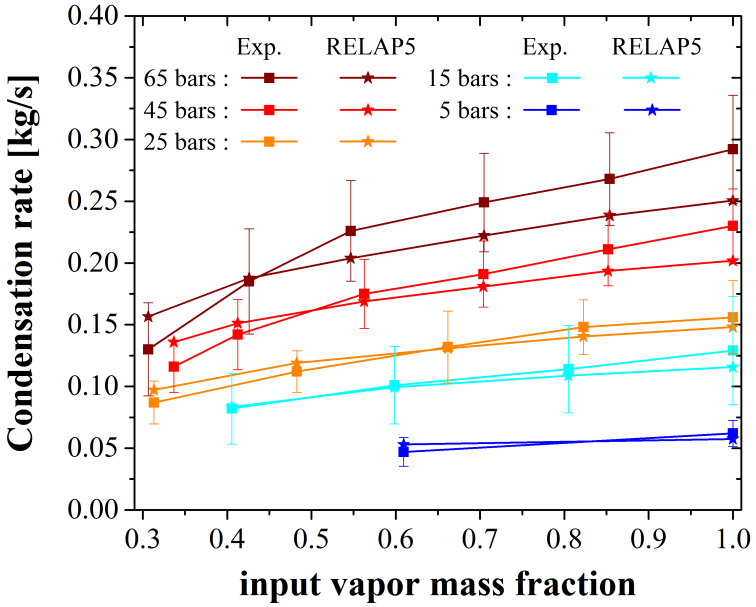

Figure 4.17: Comparison of the condensation rate for the experimental matrix

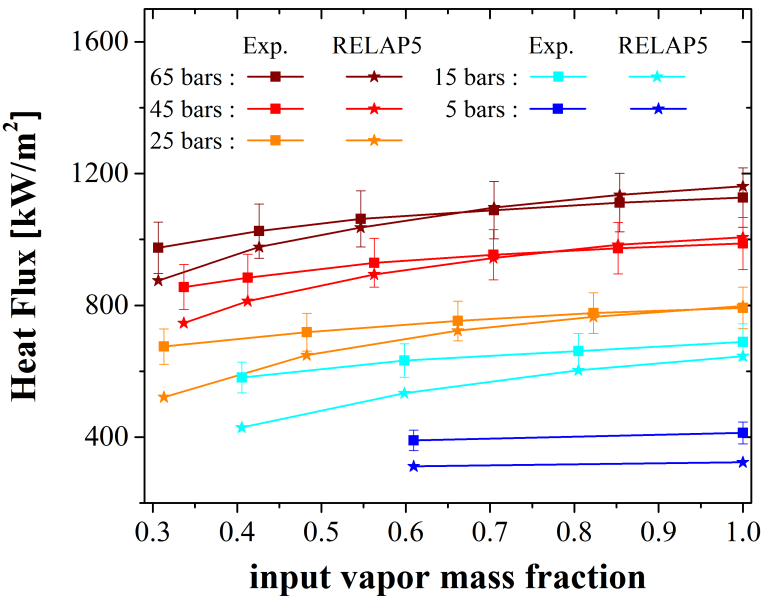

Figure 4.18: Comparison of the heat flux for the experimental matrix

The temperature of the secondary side was measured at 6 positions in the experiment (Table 1.8), at the inlet, the outlet, and 4 positions along the condensation section. The uncertainty of thermocouples was 0.3 K. The azimuthal and radial temperature distribution at the T4 position showed that the swirl generators ensured a homogeneous temperature field in the pipe within a residual nun-uniformity of 1.5 K.

Table 4.3 shows the comparison of the secondary side temperature. The inlet temperature was set corresponding to the experimental inlet conditions. Therefore, the outlet temperature data (T_{Outlet}), and the temperature difference (ΔT) were compared. The two data sets fitted in the error bands.

Table 4.3: Inlet and outlet temperature in the secondary side - comparison of the experiment and the calculation

No.	T_{Outlet} (R5)	T_{Outlet} (Exp.)	ΔT (R5)	ΔT (Exp.)	ΔT (R5) − ΔT (Exp)
51	313.555	313.85	1.905	2.2	0.295
52	313.606	313.85	1.956	2.2	0.244
151	313.774	314.05	1.924	2.2	0.276
152	313.616	313.85	1.966	2.2	0.234
153	313.568	313.85	1.918	2.2	0.282
154	313.563	313.95	1.813	2.2	0.387
251	314.28	314.45	3.63	3.8	0.17
252	314.328	314.35	3.578	3.6	0.022
253	314.321	314.45	3.671	3.8	0.129
254	314.313	314.45	3.663	3.8	0.137
255	314.032	314.45	3.382	3.8	0.418
451	314.999	315.15	3.449	3.6	0.151
452	314.142	314.15	3.592	3.6	0.008
453	314.245	314.25	3.595	3.6	0.005
454	314.263	314.35	3.613	3.7	0.087
455	313.888	313.95	3.638	3.7	0.062
456	314.175	314.25	3.625	3.7	0.075
651	316.046	316.35	3.396	3.7	0.304
652	315.52	315.75	3.47	3.7	0.23
653	316.597	316.85	3.447	3.7	0.253
654	316.388	316.65	3.438	3.7	0.262
655	316.203	316.45	3.453	3.7	0.247
656	316.118	316.35	3.468	3.7	0.232

Figure 4.19 shows the RELAP5 temperature distribution in the secondary side for E255. The temperature distribution showed a small degree of non-linearity. When the primary inlet contained more liquid, the difference between the inlet and outlet stratification angle was more significant. Therefore, the condensation heat transfer calculation changed according

to the local void fraction along the pipe, and this had a non-linear effect on the secondary side temperature.

Figure 4.19 shows two lines, which were fitted to the temperature data for $x = 2.5$ m and $x = 1.4$ m (red curve) and for for $x = 1.2$ m and $x = 0$ m (green curve). The gradient of the two curves is different. The shape of the data points is justified by the void fraction change, and, consequently the heat transfer coefficient distribution of the primary side. This illustrates that the modified RELAP code produces plausible results and confirms the significance of the introduced model improvement.

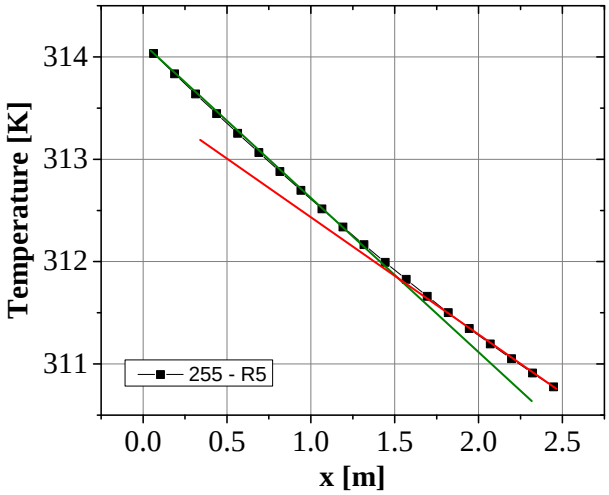

Figure 4.19: Non-linearity of the secondary side temperature distribution in E255

4.4 Conclusion from the RELAP5 calculations

The highly transient character of the INVEP experiment seriously challenged the prediction capabilities of the RELAP5 and the TRACE codes. The comparison with the experiments showed that the speed of the condensation was underpredicted in the simulations by both codes. This observation holds independently from the absence or presence of air in the pipe. The RELAP5 calculations showed a faster process than TRACE; however, the process was much slower than in the experiment. As expected, the non-condensable gas also showed a significant effect on the condensation process, especially in the RELAP5 simulations.

An enhancement of the heat transfer through the pipe wall in the frame of a sensibility study achieved an agreement between the simulation and the experiment, which showed that all other parts of the model are adequate and the attention can be focused on the performance of the heat structures. Higher enhancement of the heat transfer was needed if more non-condensable gas was present.

The inner and outer heat transfer coefficient of the pipe wall were increased independently to analyze the influence of the heat transfer of both sides individually. The enhanced heat

transfer resulted in a better fitting to the experimental data, although the inner surface heat transfer had more significant effect than the outer surface heat transfer.

A mechanistic model of the geometry of the gas-liquid interface was developed and implemented into the RELAP5/mod3.3 code. The model considered a stratified flow pattern, with steam phase in the core, axial turbulent flow at the bottom, and laminar film condensation on the upper part of the pipe cross section. The model considered local parameters of the computational node, such as the void fraction. The void fraction was used to calculate the stratification angle, which determined the stratified flow height in the pipe node.

The model was implemented into the RELAP5 code. The bottom part heat transfer coefficient was neglected during the implementation, as the pre-calculations with the MATLAB code showed that the bottom part heat transfer coefficient is negligible compared to the heat transfer coefficient of the upper part. This simplification was needed to avoid additional iterations and related complications with the solver.

The error introduced by the simplification was quantified through MATLAB calculations. They showed no significant difference, when the bottom part heat transfer was neglected.

The modified RELAP5 code was validated by simulating the transient INVEP tests and the COSMEA steady state condensation experiments.

The modified RELAP5 code achieved very good agreement with the experimental results for the temperature, pressure, and void fraction measurements during the transient condensation process for the pure steam condensation. The speed of the phase change, *i.e.* the movement of the liquid column in the pipe, was well predicted. The void fraction evolution in the computational nodes resulted in a fast altering heat transfer coefficient, which was captured by the mechanistic model.

The COSMEA facility was modeled with the modified RELAP5 code. The experimental and calculation results agreed well for the steady state condensation process in the condensation rate, secondary side temperature and the heat flux data. The calculation did not show significant difference between the original and modified RELAP5 calculations, because the flow in the pipe was in steady state condition, and the outlet flow was a mixture of steam and water. Hence, the void fraction did not change significantly along the pipe, and the Chato correlation, which considered the average flow pattern in the pipe, calculated the same heat transfer as the mechanistic model.

A geometrical correction of the heat transfer correlation was implemented for condensation with non-condensable gas. The model accounted for the specific flow pattern in the INVEP facility. The model assumed that the non-condensable gas and the steam did not mix in the pipe, and the non-condensable gas stayed on the surface of the bottom liquid flow. Therefore, laminar film condensation of pure steam occurs only at the upper part of the pipe wall, whereas the air blocks the lower part of heat transfer surface. The calculation with the geometrical correction showed very good agreement with the experimental data for different

initial conditions, different locations in the pipe, and during the transient condensation process. The model performed better than the modified RELAP5 code without the account for the non-condensable gas core. The approach is specific for a scenario, when the air and the steam do not form a homogeneous mixture.

5 Results with computational fluid dynamics

The ANSYS FLUENT v15.0 code with the implemented condensation models, which were presented in Chapter 3, were used to simulate two facilities, the LAOKOON and the COSMEA experiments.

Section 5.1 describes the developed mesh and calculation models for the LAOKOON experiment. The sensitivity study of the condensation models is presented, which was done by comparing the calculation results to the experiment. The conclusion from the sensitivity studies were used to optimize the COSMEA calculations. Section 5.2 describes the mesh, the calculation details and results for the COSMEA experimental facility. The comparison to the RELAP5 calculation is presented, and the conclusion is made regarding the simulation of transient condensation in horizontal pipes.

5.1 Calculation results for the LAOKOON facility

The LAOKOON experimental setup [99] (Fig. 5.1), which was introduced in Section 1.4.2, has been used to validate CFD codes for direct contact condensation, *e.g.* the NEPTUNE_CFD and the CFX-5 codes were used in the frame od the European ECORA project [69]. The investigation was followed by the NURESIM project [70], where the CFX software [71] was applied. Furthermore, Ceuca and Macián-Juan implemented two surface renewal theory based correlations into CFX, and simulated the facility [72] using the VOF method.

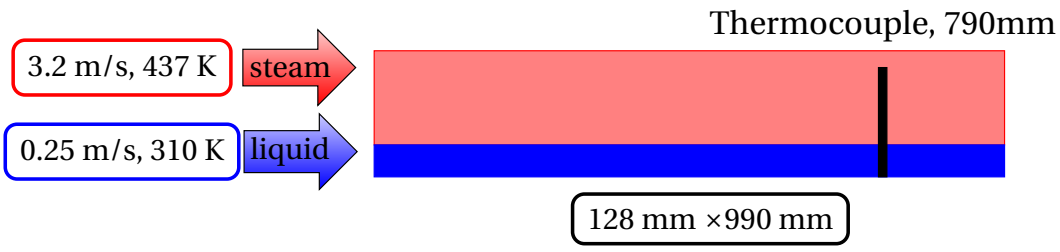

Figure 5.1: The LAOKOON experimental facility

The ECORA project [69] suggested to consider an isothermal steam flow, *i.e.* the energy equation was solved only for the liquid phase. As the walls were isothermal, the steam entered at saturation temperature, and no homogeneous condensation occurred, this approach is justified. A block velocity profile was set at the water inlet with 8% turbulence intensity. The report suggested to have pressure based outlet boundary conditions for the water and the steam.

The height of the pipe differs in the ECORA and NURESIM studies, 128 mm and 106 mm, respectively. The difference encounters the choice of the test section cross section (Fig. 5.2). The smaller value represents the height of the water channel, whereas the higher value represents the cover above the open channel. Ceuca and Macián-Juan, too, used the 106 mm height of the duct.

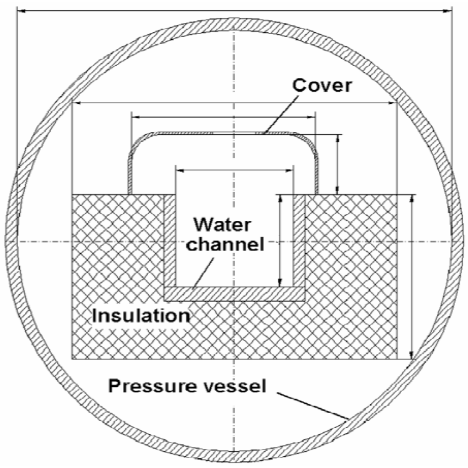

Figure 5.2: Cross section of the LAOKOON test section. The horizontal liquid flow situated at the bottom of the channel surrounded by an insulation to ensure the adiabatic wall conditions, and the whole facility was placed in a pressure chamber.

The above mentioned studies used two dimensional mesh to simulate the LAOKOON channel, which was refined towards the interface.A block inlet velocity profile and pressure outlet conditions were applied. The condensation heat and mass transfer was calculated from the turbulence at the liquid interface in the ECORA project (see Eq. 1.70). The Hughes-Duffey correlation was used together with the NEPTUNE_CFD code, and a modified version in the CFX-5 code, as well in the study of Ceuca. The NURESIM project considered a constant heat transfer coefficient. Table 5.1 summarizes the calculation details for the simulations.

The NEPTUN_CFD code could predict well the experimental data for low Reynolds number experiments, but for the high Reynolds numbers it under-predicted the condensation rates. The CFX-5 calculations within the ECORA project showed very good agreement with the high Reynolds number experiment, but for the low Reynolds number cases convergence was not achieved. The results of the CFX simulations in the frame of the NURESIM project differed significantly from the experimental results.

Table 5.1: Simulation of the LAOKOON data

Property	NEPTUNE_CFD [69]	CFX [69]	NURESIM [71]	Ceuca [72]
Section length	n.i.*	n.i.	990 mm	990 mm
Section height	128 mm	128 mm	106 mm	106 mm
Grid size	n.i.	120 × 60	106 × 99 and 212 × 198	21400 nodes
Water turb. intensity	8%	8%	3%	n.i.
Steam turb. intensity	n.i.	n.i.	1%	n.i.
Walls	adiabatic	adiabatic	symmetry	symmetry
Turbulence	k-ϵ	Steam: Laminar, Water: k-ω + TD**	k-ω SST	k-ω SST
Time step	-5×10^{-3} s	stationary	-5×10^{-4} s, adaptive	steady state
Material Properties	CATHARE	n.i.	IAPWS-97 tables	IAPWS-97 tables
Heat transfer coeff.	Hughes [67]	$\alpha = \mathrm{Nu}_i \cdot \lambda_i \cdot \lvert\nabla\epsilon\rvert$	Constant $\alpha = 1000$	H&D [67] and Shen

* : n.i. = no information
** : TD = turbulence damping applied at the interface (Eq. 1.63 with $B = 100$)

Ceuca and Macián-Juan implemented two surface renewal theory based correlations into the CFX software, the Hughes-Duffey and the Shen correlations [72]. They achieved better agreement with the experimental results when the Shen correlation was used.

Table 5.2 shows the parameters, which I used to simulate the LAOKOON flow channel. The 1.1 m long condensation duct was applied to avoid the outlet effect at the measurement location.

Table 5.2: Parameters of the LAOKOON experiment

Horizontal dimension of the flow field [m]	1.1
Vertical dimension of the flow field [m]	0.128
Height of the water level [m]	0.031
Inlet velocity of water [m /s]	0.28
Inlet velocity of steam [m/s]	3.20
Pressure [bar]	6.97
Inlet water temperature [K]	310.2
Saturation temperature [K]	437.93

5.1.1 The mesh for the LAOKOON facility

The developed mesh for the LAOKOON experiment followed the suggestions from the previous works [69],[71],[72]. The two-dimensional mesh was refined towards the water–steam interface and the walls, x is the direction of the flow (horizontal), and y is the vertical coordinate. The mesh (M01) contained 186 nodes in the horizontal direction, and vertically 100 nodes resolved the steam phase and 42 the water phase. The number of cells therefore was 25620. The inlet and outlet faces were divided into two sections according to their water level in the channel. Figure 5.3 shows the developed mesh, which was prepared using the ANSYS ICEM CFD 14.5.7 software. The x surfaces (top and bottom) were defined as adiabatic walls, and the the y surfaces were the inlet and outlet.

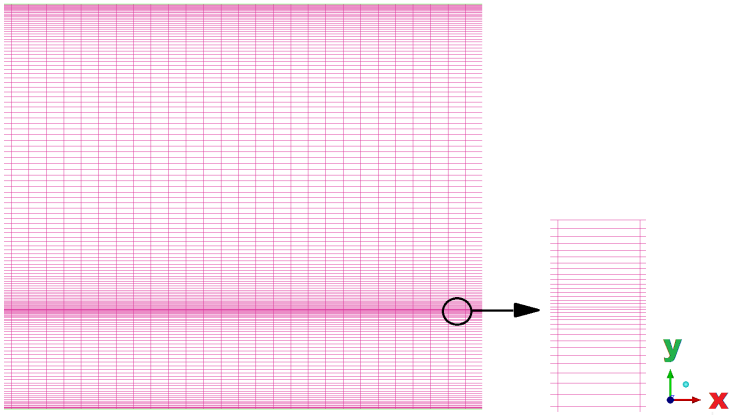

Figure 5.3: The mesh for the LAOKOON facility

Table 5.3 shows the node numbers for the meshes used for mesh refinement studies. The resolution at the interface is 0.25 mm and 0.1 mm for the two meshes in the y direction. A third mesh, M03 was used as well, which had a same number of nodes as M02, but the resolution of the interface was 0.05 mm.

Table 5.3: Node numbers on the mesh

horizontal	M01	M02
0 – 1100 mm	186	350
vertical	M01	M02
0 – 31 mm	42	84
31 – 128 mm	100	200

5.1.2 Calculation details for the LAOKOON facility

The detailed description for the here listed settings is found in the FLUENT Manuals [54],[55].

The calculations for the LAOKOON facility were run in a transient mode until the steady state conditions were reached. The simulation requires a well resolved interface, which is best achieved with a piecewise linear interface calculation (PLIC) algorithm [113] and the explicit VOF solver. The pressure-based solver was used with the gravity pointing in the $-y$ direction, the flow moved towards the x coordinate. The standard $k-\epsilon$ turbulence model was used. The pressure-velocity coupling was achieved by the PISO scheme. The pressure was discretized with the PRESTO! algorithm, and second order upwind scheme was applied for the other equations.

The material properties for steam (primary phase) and water (secondary phase) were constant, and they correspond to the inlet temperatures for the two phases (Table 5.4).

Table 5.4: Material properties in the LAOKOON experiment

Property	Steam	Liquid
Density ρ [kg/m^3]	3.66	996.77
Specific heat C_p [J/kgK]	2543	4179
Thermal conductivity λ [W/mK]	0.03389	0.6109
Viscosity μ[kg/ms]	$1.45{\cdot}10^{-5}$	$8.4{\cdot}10^{-4}$
Temperature T[K]	437.93	310.2

The following boundary conditions were set:

- the x surfaces: adiabatic wall;
- steam and water inlet: velocity;
- steam and water outlet: pressure.

Fourteen user defined memories (UDM) were defined and a used defined scalar (UDS), which correspond to the implementation details introduced in the previous chapter (Section 3.4). The following source functions were implemented on the cell level:

- Energy source on the mixture level;
- UDS source on the mixture level;
- Mass source on the primary phase level;
- Mass source on the secondary phase level.

The initialization function and the adjust function were used (for details see Section 3.4).

The initial temperature, velocity and void fraction data were set in the center of the cells and faces:

- if $y > 0.031$ m: steam phase with 3.20 m/s and 437.95 K;
- if $y < 0.031$ m: water phase with 0.28 m/s and 310.2 K.

The initial inlet conditions were set correspondingly to the flow field. The pressure outlet was set as outflow condition, *i.e.* the pressure was smaller than the adjacent cell pressure.

Transient calculation for the adiabatic flow, *i.e.* the energy and the UDS equations were switched off, run with 10^{-6} s timestep until convergence was reached. The resulted flow field was used to define proper inlet and outlet conditions for the flow field. The velocity and pressure profiles were saved along a vertical line, and this values were set as inlet and outlet conditions. The proper outlet pressure prevented the reverse flow and the divergence of the solver at the outlet. The block velocity profile introduced significant y velocity components in the inlet region. The new velocity profile achieved a smooth condition in the velocities at the interface and the walls.

After the boundary conditions were set, the initial flow field was calculated with the new pressure and velocity profiles by running the adiabatic transient until $t = 0.005$ s. The

resulted velocity field was used further as initial condition for the calculation with the condensation models. The proper initial flow field allowed higher timesteps for the calculations with energy and mass transfer ($\Delta t = 10^{-5}$). The calculations with the energy and UDS equations run until the steady state conditions were reached (about 10 s of process time).

The calculations were run in parallel mode, on 12 processors. On average, 300 000-700 000 timesteps were finished in 24 hours, which is equivalent to 3-7 s transient time.

5.1.3 Calculation results for the LAOKOON facility

The LAOKOON facility was used for the sensitivity studies of the condensation models,to test their performance for predicting the condensation rate and the temperature distribution in the water phase. The four condensation models are (Section 3.2):

1. Lee numerical iteration technique;
2. Surface renewal theory correlation;
3. Direct solution of the heat flux balance equation;
4. Phase field theory based equation.

The models are indicated with the $C = 1,2,3,4$ symbol. The models were tested with and without the smearing function ($S = 0$ and $S = 1$), and for different diffusion coefficient values of the smearing function (D). The Lee condensation model was tested for different relaxation factor values (r). Three meshes were calculated for the mesh refinement studies (M01, M02 and M03). Table 5.5 shows the calculation parameters and the fulfilled calculations.

Table 5.5: Sensitivity calculations for the LAOKOON experiment

Condensation model	M01 $S = 0$	M01 $S = 1$ $D = 10^{-8}$	M01 $S = 1$ $D = 10^{-7}$	M02 $S = 1$ $D = 10^{-7}$	M03 $S = 1$ $D = 10^{-9}$
$C = 1$ and $r = 500$	01c	11c	21c	41c	
$C = 1$ and $r = 1000$	01d	11d	21d	41d	
$C = 1$ and $r = 2000$	01e	11e	21e	41e	
$C = 1$ and $r = 2500$	01i	11i	21i	41i	
$C = 1$ and $r = 3000$	01g	11g	21g	41g	
$C = 1$ and $r = 4000$	01h	11h	21h	41h	
$C = 1$ and $r = 5000$	01f	11f	21f	41f	
$C = 2$	02a	12a	22a	42a	
$C = 3$	03a	13a	23a	43a	63b
$C = 4$	04c	14c	24c	44c	64b

The smearing function was necessary to achieve convergence for the $C = 3$ and 4 models, and for the numerical iteration model for relaxation factors higher than 2000. Without the smearing function, the pressure field at the outlet did not converge, and reversed flow, waves appeared in the calculation domain (Fig.5.4).

The results are presented through the temperature distribution along the thermocouple line. The experimental water level was at $y = 0.031$ m. The comparison focused on whether the results were dependent on the smearing diffusion coefficient and the mesh, and whether the steady state conditions were reached.

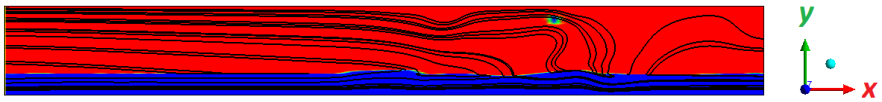

Figure 5.4: Flow pattern for the 01f study, $t = 0.4$ s. The blue color indicates the liquid, and the red the vapor phase. The balck streamlines show the resulted velocity waves and reverse flow at the outlet.

The Lee condensation model

The Lee condensation model delivered mesh independence. Figure 5.5 shows the temperature distribution along a vertical line for $r = 500$ and $r = 1000$. The temperature distribution in the two simulations with the same diffusion coefficient and relaxation factor values followed closely each other. The mesh independence was proved for other relaxation factor values as well. The mass transfer rate in the Lee condensation model did not depend on the mesh; therefore, this result was expected.

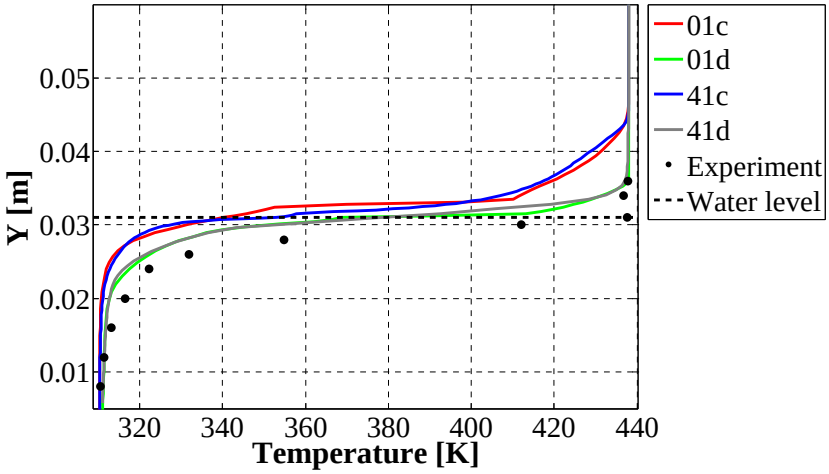

Figure 5.5: Temperature distribution for the M01 and M02 meshes, C = 1 in the LAOKOON facility

Figure 5.6 shows the calculation results for $r = 2000$. The 01 series were without smeared mass flux, 11 and 21 had 10^{-8} and 10^{-7} diffusion coefficients, respectively. The calculation results are presented for different times. The 01 series showed a temperature fluctuation in

time along the vertical line. Waves formation was observed on the water surface (Fig. 5.11) in the 01e simulation. The high relaxation factor values caused instability in the solver, and waves formed on the water surface. Consequently, temperature fluctuations were observed. The smearing function eliminated this effect, as 11e and 21e did not show the same fluctuation (see Fig 5.11). The difference in the diffusion coefficient did not have an effect on the results.

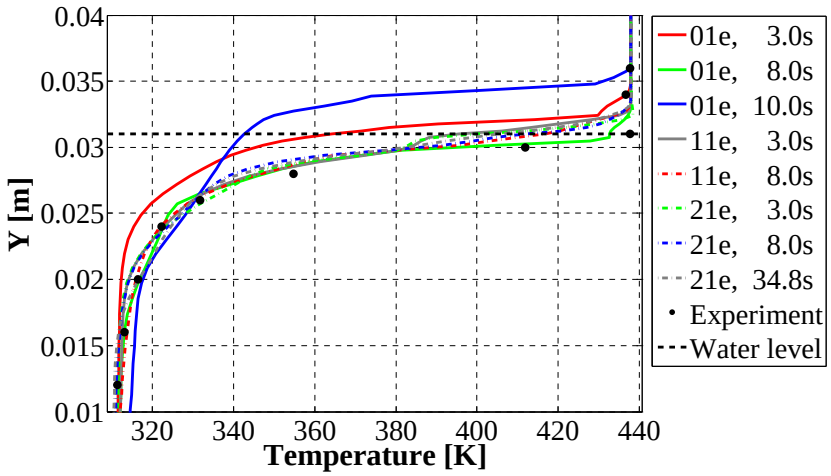

Figure 5.6: Temperature distribution for different diffusion coefficients and times in the LAOKOON facility

The Lee numerical model was run with seven relaxation factor values ranging from 500 to 5000. Figure 5.7 shows the temperature distribution for the different relaxation factors.

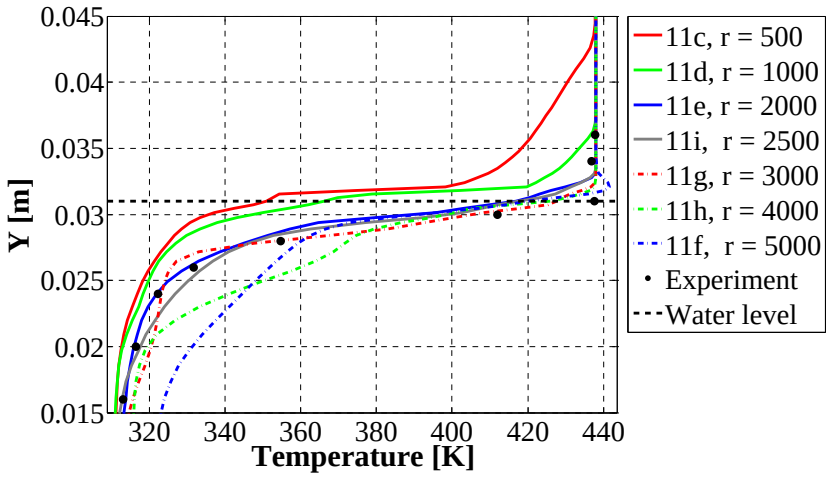

Figure 5.7: Temperature distribution for relaxation values ranging from $r = 500 - 5000$ in the LAOKOON facility

The small relaxation factor values (11c and 11d) resulted in a subcooling of the steam phase, and a relevant difference between the saturation temperature and the interface temperature. High r values (11g, 11h and 11f) resulted in wave formation on the water surface, and temperature fluctuation along the vertical line (see 11h on Fig 5.11). The calculations

for $r > 2000$ diverged without the smeared mass transfer rate. They converged with the diffusion of the mass transfer to the neighboring cells, but the wave formation and the unstable temperature solver was not avoided.

The 11e and 21e calculations showed the best agreement with the experimental results. The calculation was mesh, diffusion coefficient, and time independent.

The surface renewal model

The mass transfer rate, calculated by the surface renewal model, did not drive the interface to the saturation temperature. The calculations, however, were mesh, diffusion, and time independent. The mass transfer rate depends on the turbulence of the water; therefore, the probable explanation for the failure of the model is that the turbulence model did not calculate correctly the turbulent boundary layer at the interface. The VOF method has limitations resolving the momentum equation at the interface, if the velocity between the two phases significantly differ.

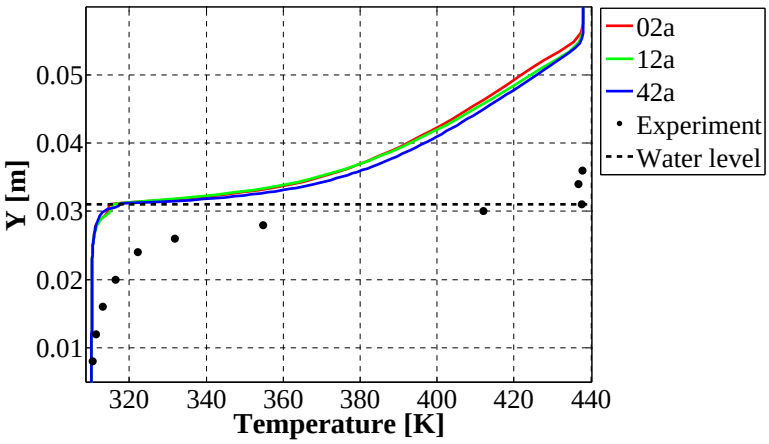

Figure 5.8: Temperature distribution for the $C = 2$ condensation model in the LAOKOON facility

The heat flux balance model

Figure 5.9 shows the calculation results for the heat flux balance based model, for two different values of the diffusion coefficient and all the three meshes.

The heat flux balance model was not mesh independent for the M01 and M02 meshes, because the temperature boundary layer was not resolved. The temperature gradient depends on the mesh, if not enough nodes are presented in the laminar boundary layer. The more refined mesh resulted in the interface temperature, which was closer to the saturation value. The M03 mesh, with a better resolution of the interfacial region, was as well tested. The finer mesh in the interfacial region resulted in a better agreement with the experimental results. However, the most refined mesh could not reproduce the experimental results. Better resolution of the interface was not possible with the solver settings reported above, and the k-ϵ turbulent model.

The diffusion coefficient did not have an effect on the calculation; nevertheless, the solver diverged for 03a, when the mass transfer rate was not smeared to the neighboring cells.

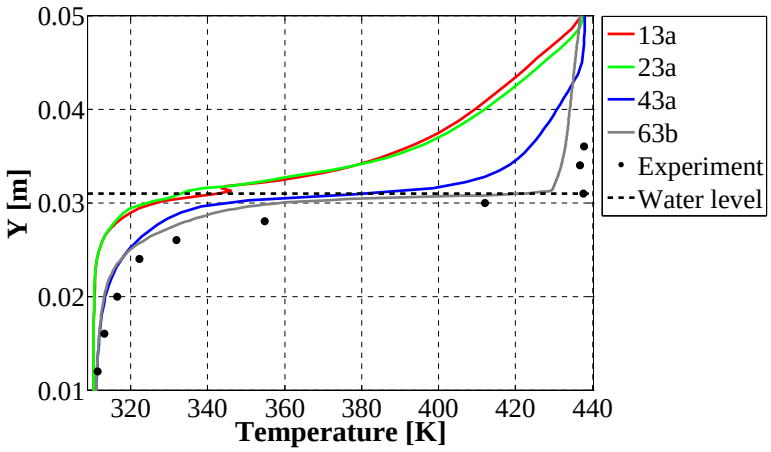

Figure 5.9: Temperature distribution for the $C = 3$ condensation model in the LAOKOON facility

The phase field model

The phase field model predicted the interface temperature better, when the refined mesh was used. With the M02 mesh, the steam was subcooled only in the interfacial region. The temperature distribution in the water followed close the experimental results. The diffusion coefficient did not have an effect on the results.

The M03 mesh was calculated, to test whether the calculation is mesh dependent. No relevant change was observed in the temperature distribution for the M03 mesh; however, the calculation time increased. The more refined mesh required smaller timesteps (10^{-6} s).

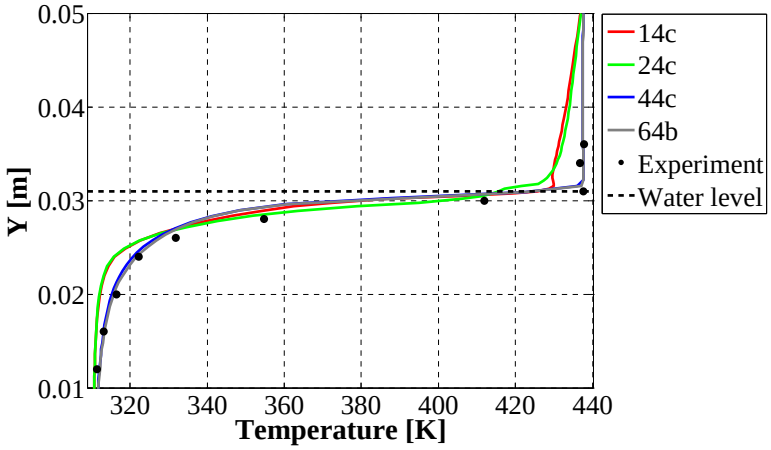

Figure 5.10: Temperature distribution for the $C = 4$ condensation model in the LAOKOON facility

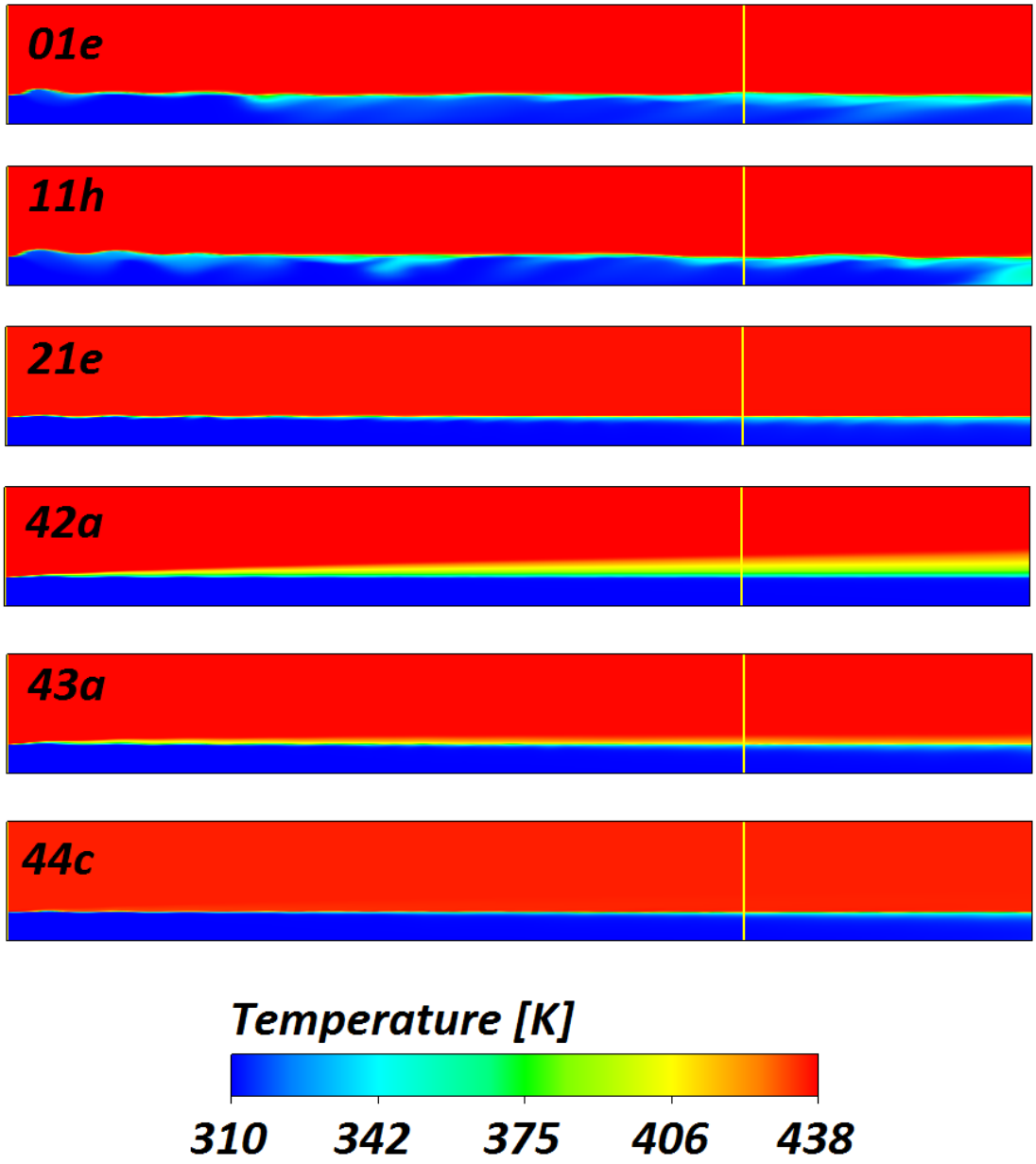

Figure 5.11: Two-dimensional temperature field for selected simulations in the LAOKOON facility

5.1.4 Conclusions from the LAOKOON calculations

The sensitivity study showed that the steady state conditions were reached by the transient calculation in 10 s with all four models. The diffusion coefficient did not have an effect on the temperature distributions; however, the diffusion itself improved convergence. Moreover, the $C = 1$ and 2 models were mesh independent for the resolution of M01 mesh. The phase field model ($C = 4$) was mesh independent for the resolution of M02 mesh. The $C = 3$ model was dependent on the cell size at the interface.

The driving force in the condensation is the temperature difference between the saturation and the interfacial cell temperature. After long enough iterations all models should achieve saturation temperature at the interface. However, if the temperature of the cell depends on other factors, such as heat convection, which acts against the driving force of the mass transfer, this might never be reached.

Figure 5.12 shows the results of the achieved best settings for the four condensation models. The Lee numerical iteration and the phase field models obtained the closest temperature distribution to the experimental data. The condensation mass transfer for the surface renewal model did not compensate the subcooling of the gas phase. The direct solution of the heat flux balance equation achieved results that are close to the experiment, but the subcooling of the gas phase in the interfacial region persisted.

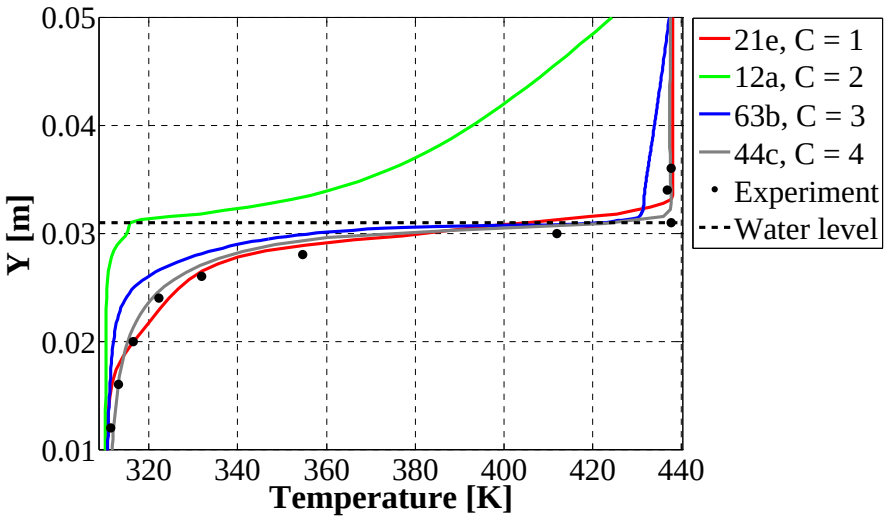

Figure 5.12: Temperature distribution results for the four condensation models in the LAOKOON facility

The optimal relaxation factor in the Lee model was independent from the mesh and the diffusion coefficient, although, it is dependent on the specific problem. The low values of r result in a subcooling of the gas phase, and the too high value causes convergence difficulties. The best practice for finding the optimal value is by trial-and-error, which is not efficient for big geometries.

The use of the surface renewal model is not suggested, as it is dependent on the turbulent conditions at the interface, which is difficult to resolve with the VOF model. The other three models are applicable, although, they have limitations. The phase field model and the heat flux balance model require a refined mesh in the interfacial region. The Lee model is suitable for a wide range of applications; however, the selection of the relaxation factor might be a limiting factor. The model is suggested for slow transients or steady state flows, with not too high calculation costs.

The sensitivity study considered several aspects; however, the effect of turbulence models or solver settings was not analyzed. The simulations, nevertheless, are expected to be independent from these settings. The next section shows that the models are suited for other applications as well.

5.2 Calculation results for the COSMEA facility

The COSMEA facility was calculated with the condensation models as well. Figure 5.13 shows the scheme of the setup, for more details see Section 1.4.3.

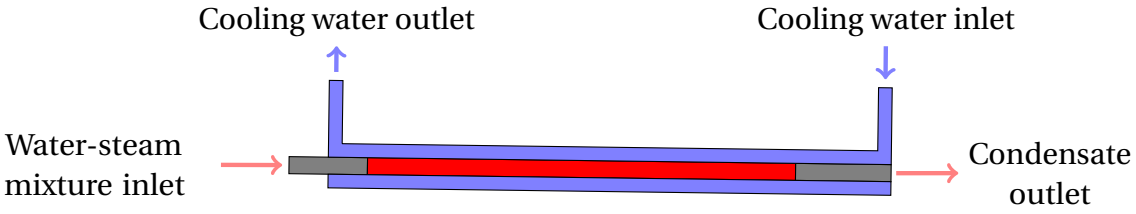

Figure 5.13: Scheme of the COSMEA experimental facility

The experimental facility consisted of a slightly inclined horizontal condensation pipe. The pipe wall was cooled by a secondary side. The instrumentation provided information about the flow pattern, the temperature and heat flux data at one location along the pipe, and the condensation rate during the experiment. The pipe had an inner diameter of 43.3 mm, and a length of 3530 mm.

5.2.1 The mesh for the COSMEA facility

The length per diameter ratio of the pipe was 81.5, and the mesh should be fine enough to resolve the liquid film on the wall; therefore, limiting the mesh to a feasible size resulted in cells with high aspect ratio. The flow was symmetric to the vertical plane in the middle of the pipe; consequently, only half of the pipe was simulated.

Figure 5.14 shows the cross section of the pipe (the x direction was the direction of the flow, y vertically, z horizontally define the cross section). The structured mesh consisting of three O-blocks with hexahedral cells was developed. The outer part was assigned to a 1 mm wide ring (e1). A second part (e2) was associated with the points in the middle of the pipe cross section, with a 12 mm distance from the center. The inner core of the pipe was

defined with a half O-grid (e3 and e4). Table 5.6 shows the number of nodes on the edges. The flow domain consisted of three axial sections: adiabatic inlet (ei), condensation (ec), and adiabatic outlet (eo). The number of nodes along these parts are presented in the table as well. The whole mesh had 1'690'392 nodes. The resolution of the mesh towards the wall is 0.02 mm.

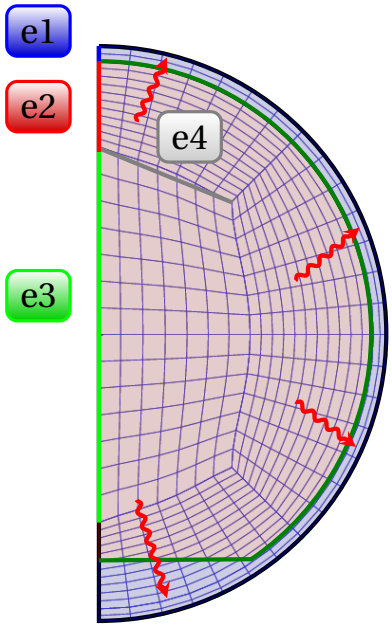

Figure 5.14: Scheme of the mesh in the cross-section of the COSMEA test pipe

Table 5.6: Number of nodes along the edges of the mesh for COSMEA

e1	e2	e3	e4	ei	ec	eo
50	30	20	15	60	300	60

5.2.2 Calculation details for the COSMEA facility

The condensation and the refined mesh towards the interface limited the timestep, and the long pipe required many cells. The hereby presented transient calculations lasted for 10 weeks on 32 processors. Therefore, one test case (No. 454) was chosen from the COSMEA measurement matrix to demonstrate the prediction ability of the condensation models.

For the COSMEA calculations, the pressure based solver was used, in both steady-state and transient. The gravity was set to $g_y = 9.81 \cdot \cos\theta = -9.8091$ in the y direction, and to $g_x = 9.81 \cdot \cos\theta = 0.13012$ in the x direction, where θ is the inclination angle of the pipe.

The k-ω turbulent model was used and the turbulent damping factor was set to 10 (see Eq. 1.63). The VOF multiphase method was set implicit in the steady state, and explicit in the transient calculations. The PISO scheme was applied for the pressure–velocity coupling,

and the PRESTO! algorithm discretized the pressure. The second order upwind scheme was set for the other equations.

The material properties were constant, and they corresponded to the inlet temperature of the two phases (Table 5.7). The operating pressure was 45.4 bars, the saturation temperature was 531.07 K.

Table 5.7: Material properties for the COSMEA experiment

Property	Steam	Liquid
Density ρ[kg/m^3]	22.907	786.77
Specific heat C_p[J/kgK]	4244.55	4955.717
Thermal conductivity λ[W/mK]	0.053449	0.61154
Viscosity μ[kg/ms]	$1.78{\cdot}10^{-5}$	$1.0{\cdot}10^{-4}$
Temperature T[K]	531.07	531.07

The inlet boundary condition for the void fraction and the velocity was defined by a user defined function. The experimental inlet mass flow rate was converted to block velocity profile. The injection system of the water inlet contains of a $y_{wl} = 0.5$ mm wide ring, which ensured the 0.5 mm thick annular water flow at the inlet (A_{water}). The core of the pipe (A_{steam}) was occupied by steam. Therefore, the steam and liquid inlet area was calculated:

$$A_{steam} = r^2 \cdot \pi = \left(R - y_{wl}\right)^2 \cdot \pi; \tag{5.1}$$

$$A_{water} = R^2 \cdot \pi - A_{steam} = \left(R^2 - \left(R^2 - y_{wl}\right)^2\right) \cdot \pi. \tag{5.2}$$

The velocity of the corresponding phase ($p = steam, water$) was calculated using the area, the mass flow rate and the density of the phase:

$$V_p = \frac{\dot{m}_p}{\rho_p A_p}. \tag{5.3}$$

The outlet boundary was an outflow condition, set by a user defined function. The $x-y$ plane obtained a symmetry boundary condition. The pipe wall was adiabatic for the inlet and outlet sections. The condensation section wall was made of a 2.5 mm thick stainless steel (8 g/cm^3 density, 15 W/mK thermal conductivity and 500 J/kgK specific heat). The secondary side was considered with an outlet wall temperature of 312.8 K.

The mesh had about 1.6 million nodes; therefore, the optimal initial conditions should be reached before calculating the condensation phenomenon. For this purpose, a steady state calculation was performed with the initial conditions being equivalent to the inlet velocity condition, *i.e.* a 0.5 mm annular water flow at 4.5 m/s and a core steam flow with 10.4 m/s.

The block velocity profile at the inlet caused a big pressure difference at the interface between the gas and the liquid, which resulted in a local peak of the cross sectional velocity

component at the inlet. This effect causes divergence in the momentum equation for high timestep values. To avoid this effect, the convergence for the velocity field in the pipe was reached with a small timestep (10^{-7} s), and a velocity profile was saved at the cross section $x = -230$ mm (for reference locations see Table 1.7). This profile was used later as inlet condition and a timestep of 10^{-5} s was achieved.

The initial field for the momentum and the void fraction equations were achieved by calculating the steady state solution without the energy equation (adiabatic flow). The convergence was reached after 450 iterations. The implicit VOF scheme was used and the modified HRIC scheme to reconstruct the interface.

5.2.3 Calculation results for the COSMEA facility

Adiabatic flow calculation - steady state solver

The void fraction distribution in the pipe was a result of a transient process. The proper initial conditions for the transient were reached by steady state simulations. As a first step, the energy and the user defined scalar equations were not solved, and the steady state solver was run until the convergence of the momentum, turbulence and VOF equations. The k-ϵ turbulent model caused divergence in the continuity equation; therefore, the k-ω model was used, with settings tuned to achieve the fastest convergence. The absence of turbulence damping, high values of the damping factor, and the SST k-ω model resulted in a divergence of the solver.

Saturation initial temperature was set for both phases, and the x velocity component was calculated according to the mass flow separately for the phases. The water phase assumed to occupied a 0.5 mm thick annular region, the core of the pipe was occupied by the steam phase.

The convergence of the momentum, turbulence and void fraction equations was reached after 450 iterations, and this results were used further as initial condition for the calculation with phase change.

Condensation calculation - steady state solver

In the second step, steady state calculations were run with the energy equation to achieve good initial conditions for the transient calculation. The steady state solver converged fast together with the energy and the UDS equations; therefore, it was used to find the optimal settings for the later simulations.

The simulations without the smearing of the mass source resulted in reversed flow at the outlet and divergence of the continuity equation, just as in the LAOKOON simulations. The diffusion coefficient was found such that the interface region occupied 6 cells ($D = 10^{-10}$). The Lee condensation model diverged with relaxation factor values higher than 8000. The surface renewal calculation resulted in an unphysical subcooling of the steam phase;

therefore, this model was not used for transient analysis.

The heat flux balance based ($C = 3$) condensation model achieved the best results for the temperature field in the steady state calculation. The gas phase subcooling did not occur, and the temperature distribution in the liquid layer was linear. Figure 5.15 shows the temperature data in the pipe cross section at $x = 1.32$ m. The temperature distribution is presented along five radial lines (0°, 45°, 90°, 135°and 180°). The liquid film was 0.2 mm thick in the upper region, and 1 mm thick at the bottom of the pipe, having a local minimum at 135°.

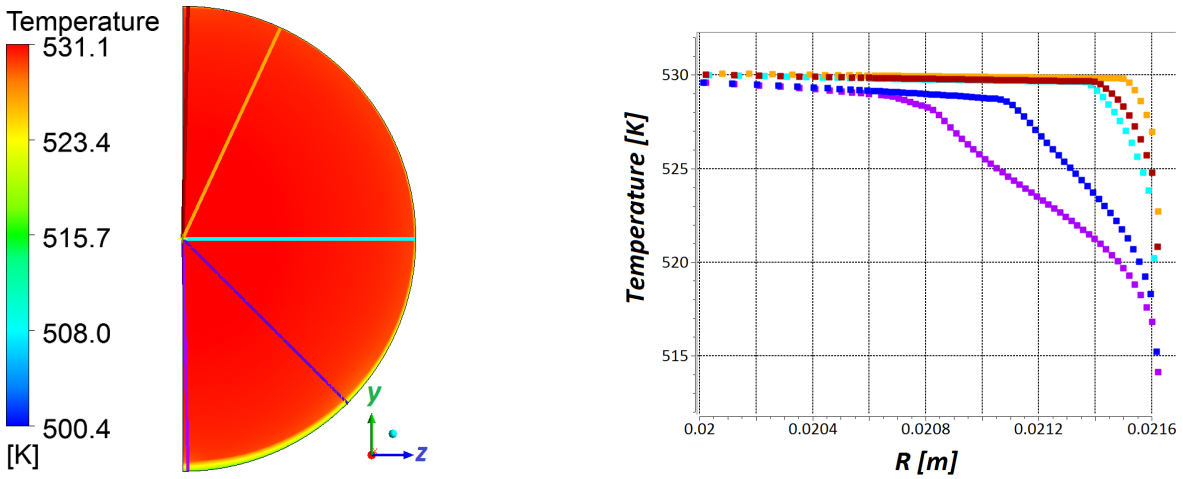

Figure 5.15: Temperature distribution in the cross section of the COSMEA condensation pipe and along five radial lines ($x = 1800$ mm) for the steady state simulation with the $C = 3$ condensation model

Figure 5.16 shows the temperature distribution for the five radial lines, which resulted from the steady state calculation with three condensation models. The relaxation factor in the Lee condensation model was $r = 6000$. The slight subcooling of the gas phase was observed in the interface region for $C = 1$ and $C = 4$, but it was not present for the $C = 3$ model. As the temperature distribution in the liquid film is linear, the temperature gradient is calculated correctly in the heat flux balance model, and it drives the interface to saturation conditions fast. The other two model obtained similar results and the condensation mass transfer rate was similarly predicted in the two approaches. The phase field theory calculated a lower steam temperature in the flume (0° and 45°), where a course part of the mesh is present in the interface region.

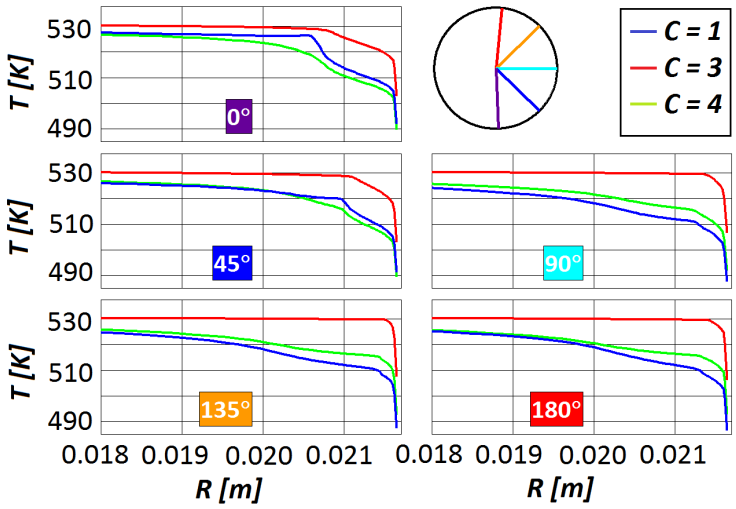

Figure 5.16: Results of the steady state calculation of the COSMEA facility: temperature distribution along five lines at $x = 1800$ mm for three condensation models

Condensation calculation - transient solver

The steady state results for the numerical iteration technique with $r = 6000$, for the heat flux balance and for the phase field models were used to calculate the transient phenomenon. The calculations started with a timestep of $\Delta t = 10^{-6}$ s, which was increased to $\Delta t = 10^{-5}$ s.

The heat flux balance model encountered convergence problems in the user defined scalar equation after 0.35 s, because the very thin liquid layer. The scalar equation had a zero flux boundary condition; thus, the thin liquid layer resulted in a non-zero mass flux in the wall adjacent cells, which caused the divergence of the solver. Consequently, the heat flux balance based model was not able to calculate the transient condensation process in the pipe.

The numerical iteration and the phase field models were numerically stable. The transient run for 23 s. The temperature field and the velocity field became constant after this period. The results were compared to the experiments. The phase field model obtained close results to the experimental data, whereas the numerical iteration technique under-predicted the condensation rate. The discussion on the comparison of the two models and the comparison to the RELAP5 calculation and the experiment is presented in Section 5.2.4. The detailed results are presented below for the phase field model.

Figure 5.17 shows the cross section of the pipe, with the five angular locations of the heat flux measurements. The five radial lines (L1-L5) indicated on the figure were used to analyze the temperature distribution.

Figure 5.18 shows the developed void fraction distribution for five locations along the pipe. The left side of the figures present the X-ray tomography images from the experiment, and the right sides are the results from the phase field model, where the red area indicates the

steam, and the blue the water phase. The white line on the tomography images define the stratified flow height in the experiments [101]. The values are reported in Table 5.8.

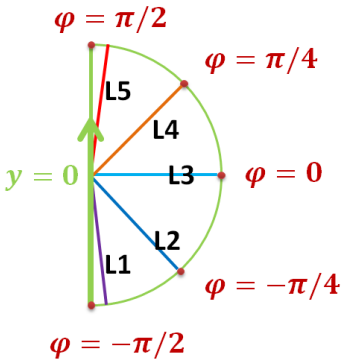

Figure 5.17: Measurement points at x = 1800 mm in the COSMEA condensation pipe and the location of the five radial lines for analyzing the temperature distribution

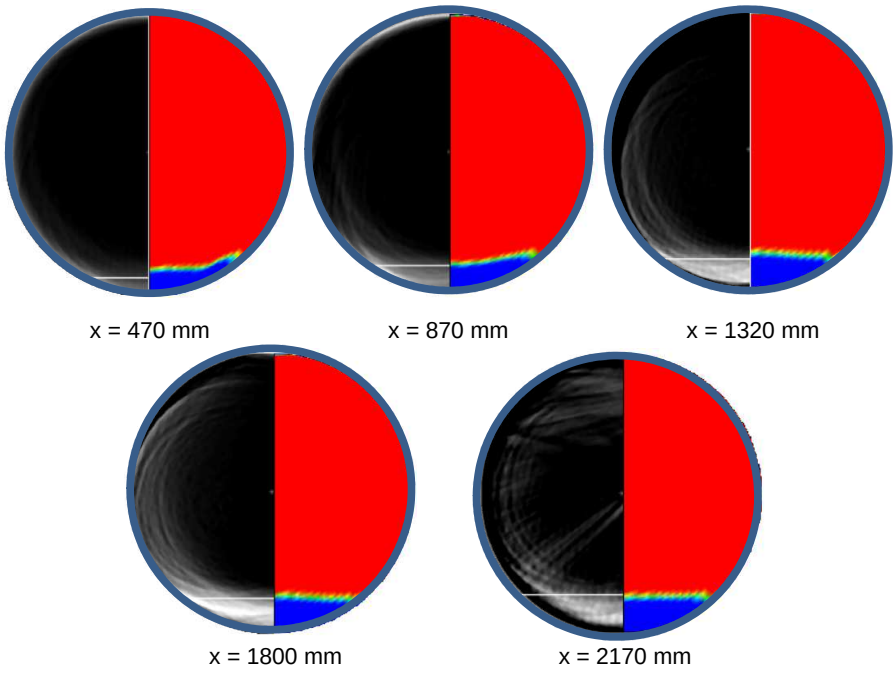

Figure 5.18: Comparison of the void fraction distribution between the X-ray tomography images and the CFD results at five cross sections along the COSMEA condensation pipe.

The tomography images averaged the void fraction distribution over a signal acquisition period of 3 minutes; therefore, waves were not detected. The visualization of the CFD results prove that no significant wave formation occurred in the pipe. The liquid film thickness in the CFD calculation was defined through the radial coordinate of the cell, where the gradient of the void fraction had a local maximum. The flume thickness in the experiment and the calculation showed good agreement.

Figure 5.19.a shows the projection of velocity vectors onto the plane of the pipe cross section at $x = 1800$ mm. Figure 5.19.b shows the distribution of the velocity magnitude. The bottom flow mainly had axial components, whereas the liquid film velocity had azimuthal components as well. The steam moved towards the pipe wall, where it condensed, causing a vortex in the gas phase. The liquid film drained into the axial bottom flow.

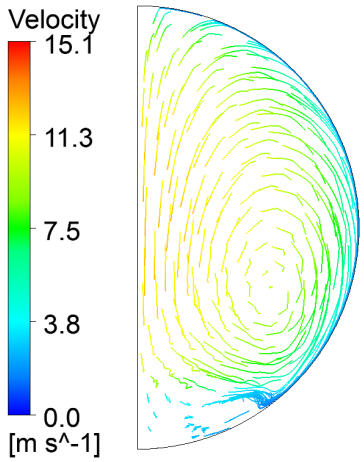

5.19.a

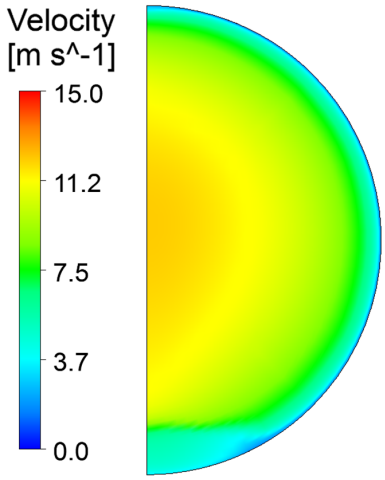

5.19.b

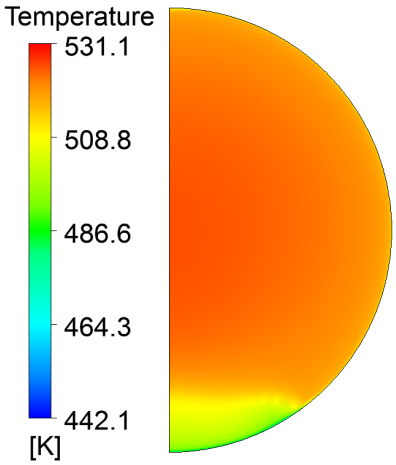

5.19.c

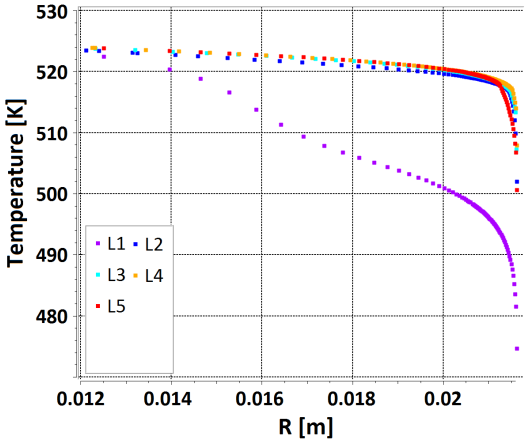

5.19.d

Figure 5.19: Streamline projection, velocity and temperature distribution for a cross section of the COSMEA condensation pipe at $x = 1800$ mm, for the transient calculation with $C = 4$

The Reynolds number of the steam phase was 560'000, the axial flow had a Reynolds number of 305'000, and the liquid film 200. The values were calculated from the average velocities, the hydraulic diameters of the flow cross section, and the material properties. The axial water flow and the steam were turbulent flows, the liquid film on the wall was laminar. This is in agreement with the assumptions of the MATLAB calculation for the heat transfer coefficient calculation (Chapter 2).

The temperature profiles on Fig. 5.19.c and d showed that the water cooled down to 486 K from the saturation value (531 K). The gas phase experienced a subcooling of 5 K on average,

which is unrealistic, and it was caused by the coarse mesh in the core of the pipe, where the axial flume located. Figure 5.19.d shows the temperature distribution close to the interface along the five radial lines (L1-L5). The temperature distribution in the liquid film (L2-L5) was linear, and a sudden change in the temperature was observed at the interface.

Figure 5.20 shows the measured and calculated wall heat flux for the x = 1800 mm cross section. The data are presented along the polar coordinate φ (see Fig. 5.17). The heat flux was negative, as the wall was colder than the flow in the pipe. The error bars show the measurement uncertainty of 8%, which is too large to draw conclusions. The CFD simulation showed the expected difference between the axial bottom flow and the laminar film flow. The heat flux has a local minimum at the top of the pipe cross section, and an absolute minimum at the boundary between the liquid film and the axial flume.

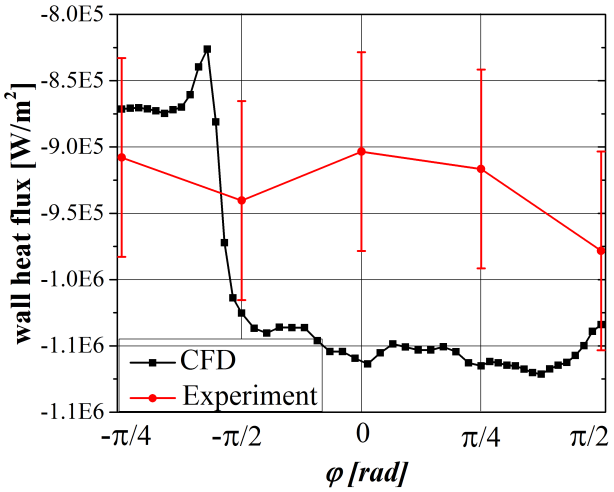

Figure 5.20: Measured and calculated heat flux distribution at x = 1800 mm of the COSMEA condensation pipe in the transient simulation with $C = 4$

The heat flux distribution reflects the variation of the thickness of the liquid film. Figure 5.21 shows the calculated liquid film thickness. At the top of the pipe, a local maximum was observed, and the average thickness of the liquid layer was 0.1 mm.

The MATLAB code (Chapter 2) was applied with the conditions from the COSMEA facility to determine the average heat transfer coefficient along the pipe wall. The aim was to test the mechanistic approach based on the introduction of the stratification angle by the comparison to CFD. The void fraction results at x = 1800 mm in the CFD calculation was used as an input parameter for the MATLAB calculation (Fig. 5.22). The calculated film thickness was 0.1 mm, which is equal to the results from the CFD calculation.

The MATLAB code was modified to calculate the distribution of the heat transfer coefficient along the circumference of the pipe (using Eq. 2.56). The results were compared to the CFD calculation (Fig. 5.23). The normalization of the heat flux was necessary, because the secondary side was not modeled; thus, the relative shapes of the heat flux distribution can be compared.

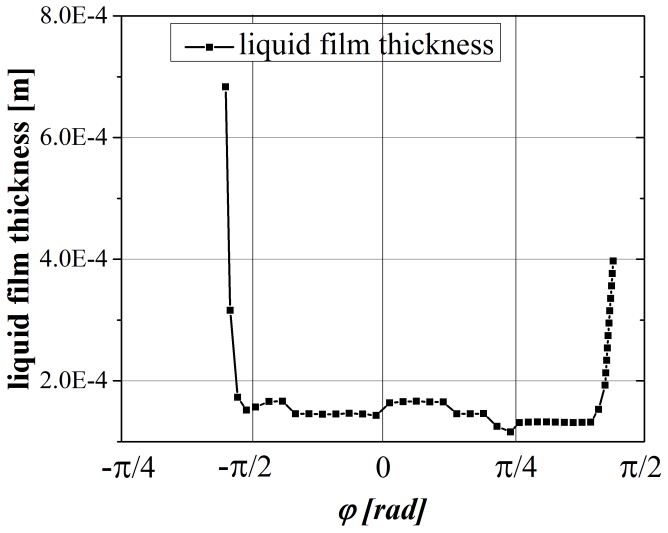

Figure 5.21: Calculated film thickness at $x = 1800$ mm of the COSMEA condensation pipe in the transient simulation with $C = 4$

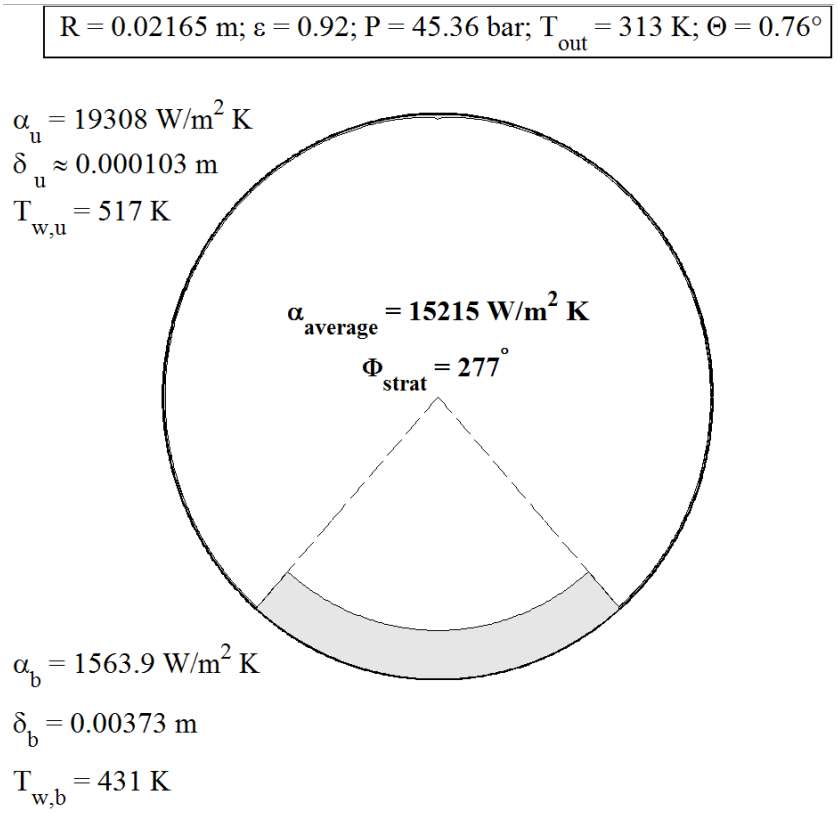

Figure 5.22: Results of the MATLAB calculation for the COSMEA 454 experiment at $x = 1800$ mm

The laminar flow model of Nusselt predicted a smooth distribution, with a local minimum at the top of the wall, where the liquid film has a local maximum. The CFD code, too, predicted a decrease of the heat transfer coefficient in this region. However, the difference was not as significant as in the MATLAB calculation. The calculation with the MATLAB code assumed a uniform film thickness at the bottom of the pipe; therefore, the transition of the heat transfer coefficient between the liquid film and the axial flow was not captured. The heat transfer coefficient in the CFD code had a minimum value, where the liquid film met the axial flow, and the vortexes formed in the gas phase.

The mechanistic model was able to predict the major qualitative features of the heat transfer coefficient in a horizontal pipe. The assumptions of the laminar film flow and turbulent axial flow were supported by the CFD simulations.

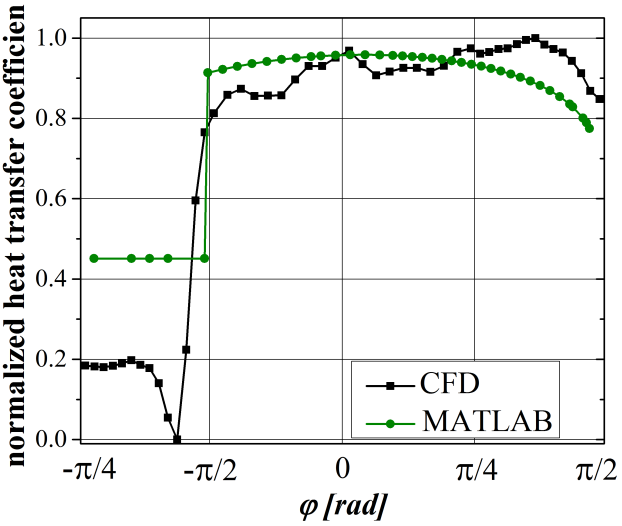

Figure 5.23: Normalized wall heat flux in the CFD calculation and the MATLAB calculation - COSMEA experiment at $x = 1800$ mm

5.2.4 Conclusions and comparison to the RELAP5 calculation

The COSMEA facility challenged the CFD calculation due to the high length to diameter ratio and the very thin condensate film on the pipe wall. The developed mesh had refined cells towards the pipe walls, but in the middle of the pipe, where the flume was located, the mesh was coarse. The calculation time was high due to the large dimensions of the flow domain.

The surface renewal theory did not provide high enough mass transfer rates, as the liquid film was laminar and a significant heat transfer enhancement by surface renewal takes only place if there is turbulence in the liquid phase. The heat flux balance method provided good initial conditions for the transient calculations; however, the transient calculation did not converge for the user defined scalar equation. Therefore, these two models were not able to calculate the COSMEA experiment.

The numerical iteration technique and the phase field model were numerically stable for both steady state and transient calculations. The calculation results for the flow field, the heat transfer coefficient, the film thickness were analyzed in detail for the phase field model. The results were used to test the assumptions of Chapter 2.

The numerical iteration technique under-predicted the condensation rate. Figure 5.24 demonstrates the void fraction distribution at x = 1800 mm for the numerical iteration technique and the phase field model, where the lower stratification height in the C = 1 calculation reflects the smaller condensation rate.

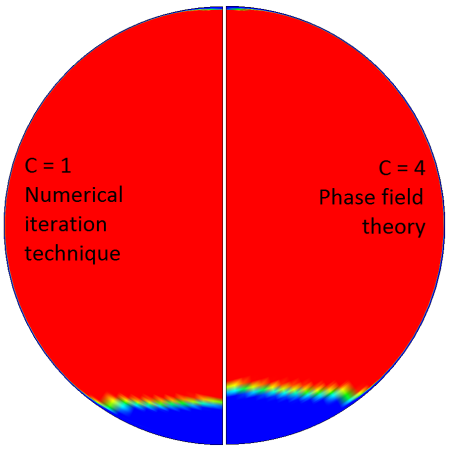

Figure 5.24: Comparison of the flow pattern for C = 1 and C = 4

The results suggest that the constant relaxation factor in the transient calculation and for the changing liquid film thickness could not achieve proper global condensation rate in the pipe. Varying the relaxation rate in the transient calculation was not possible, considering the long simulation time and the trial-and-error procedure to find the optimal value.

Table 5.8 shows the comparison between the experiment, the RELAP5 calculation (see Section 4.3) and the CFD calculations. The heat flux data are the average of the wall heat flux for the CFD calculations and the experiments at x = 1800 mm.

Table 5.8: Comparison of the experiment, the RELAP5, and the CFD calculations

	Experiment	RELAP5	CFD ($C = 4$)	CFD ($C = 1$)
$h(x = 470\text{mm})$ [mm]	2.5	5.1	4.0	3.8
$h(x = 870\text{mm})$ [mm]	4.0	5.5	4.4	4.3
$h(x = 1320\text{mm})$[mm]	4.5	6.1	5.5	4.4
$h(x = 1800\text{mm})$[mm]	5.5	6.8	6.0	4.5
$h(x = 2170\text{mm})$ [mm]	6.5	7.3	6.0	4.4
Heat flux [kW/m^2]	930	893	1005	1060
Condensation rate [kg/s]	0.175	0.169	0.088	0.032

The RELAP5 code over-predicted the stratification height, while the phase field model over-predicted it for the first three locations. However, considering the measurement uncertainty of 0.5 mm, both calculations followed well the distribution of the experimental results. The RELAP5 code under-predicted the heat flux by 4 %, while the phase field model over-predicted it by 8%. The experimental condensation rate had 16% uncertainty. The RELAP5 code estimated the condensation rate within the error bands. The phase field model, however, under-predicted the condensation rate by 50% because of the unrealistic subcooling of the gas phase. The numerical iteration technique under-predicted the condensation rate and the stratified height, whereas the heat flux was over-predicted by 18%.

The subcooling of the steam in the phase field approach was not completely avoided, mainly because the mesh was not refined at the stratified flow surface, but it was much less pronounced than the relaxation method.

6 Conclusions and Outlook

This thesis was dedicated to analyze condensation for the application in the emergency cooling system of a Gen-III+ boiling water reactor [1]. Two approaches were investigated, one-dimensional modeling with the RELAP5 system code, and three-dimensional modeling with the FLUENT computational fluid dynamics code. The conclusions concern the two approaches individually, and the comparison of them.

6.1 Conclusion on the thermal-hydraulic system code calculation

Although the RELAP5 code is a well established and efficient tool to simulate condensation processes, a deficiency was identified in a post-test analysis of the strongly transient, fast condensation experiments, called INVEP. In these experiments, the speed of the condensation process was driven to the extreme by a sudden pressurization with vapor of a nearly horizontal pipe resting in a basin with cold water. Although the condensation process in the emergency condenser of the KERENA reactor is much less dynamic, and RELAP5 was known to predict classical accident scenarios with a satisfying accuracy, it was concluded that the a best estimate code should be able to cover also borderline cases, such as the INVEP experiments, because this guarantees a high robustness of the thermal hydraulic simulations.

Sensitivity studies of the heat transfer in the RELAP5 calculations showed, that the dominating factor for the underestimation of the process dynamics was the condensation heat transfer model. Therefore, a mechanistic approach was developed to calculate the heat transfer coefficient in a cross section of the flow field, considering local parameters in the pipe.

The model assumed a stratified flow pattern, with steam phase in the core, axial turbulent flow at the bottom, and laminar film condensation on the upper part of the pipe. The local void fraction was used to calculate the stratification angle, which determines the stratified flow height and the heat transfer coefficient in a cross section of the pipe.

The model was investigated first on a single pipe cross section. The calculation showed that the bottom part heat transfer coefficient had a negligible contribution to the heat transfer; therefore, only the upper part heat transfer calculation was implemented into the RELAP5 code.

The modified RELAP5 code was validated against two experimental test cases representing different geometries. First of all, the same INVEP experiment [96], which revealed the deficiencies of the original RELAP5 version, was calculated with the modified RELAP5 code. The simulation predicted well the pressure, void fraction and temperature data for different initial conditions, and different locations in the condensation pipe during the transient condensation process. The mechanistic model was able to capture the heat transfer, when the void fraction altered fast in the computational node. Therefore, the modified RELAP5 achieved better agreement with the experimental results, and the condensation rate was predicted better than with the original code.

The second test facility used for the validation was the COSMEA experiment [101], which is a single tube experiment for flow morphology and heat transfer studies. The calculations were able to reproduce the experimental temperature and condensation rate results for different initial pressure and mass flow rates. The modified condensation model and the original RELAP5 calculation did not show a difference for the steady state condensation process. The Chato correlation, which is implemented in the RELAP5 code, obtains the heat transfer coefficient for an average stratification angle in the flow. Therefore, the modified model and the Chato correlation acquired the same heat transfer to the secondary side.

A geometrical heat transfer correlation was implemented for condensation with non-condensable gas. The model accounted for the specific flow pattern in the INVEP facility. The model assumed that the non-condensable gas and the steam did not mix in the pipe, and the non-condensable gas bubble stayed on the surface of the bottom liquid flow. Therefore, laminar film condensation of pure steam occurs at the upper part of the pipe wall. The calculation with the geometrical condensation model showed very good agreement with the experiments. The model performed better than the modified RELAP5 code without the account for the non-condensable gas core. The approach is specific for a scenario, when the air does not mix with the steam.

6.2 Conclusion on the computational fluid dynamics calculation

Computational fluid dynamics calculations were done using the volume of fluid multiphase method in the FLUENT code. The method is highly efficient in calculation of multiphase flows with well defined interfaces, although the FLUENT code does not provide phase transition model. To extend the possibilities of the software, four phase change models were developed and implemented.

The first technique, the so-called numerical iteration method introduced an arbitrary mass and energy transfer at the interface, if the temperature of the corresponding cell was different from the saturation value [78]. The mass transfer rate was a function of the relaxation factor, which determined the speed of convergence to the saturation temperature in the interface cells. The second approach was the surface renewal theory, which assumed that the eddies, forming on the liquid surface, are responsible for the transfer of the latent heat to the bulk liquid. The condensation rate depended on the turbulent velocity and length scale [67]. The third model solved the heat flux balance equation at the interface; therefore, the resolution of the thermal boundary layer was necessary. The fourth technique was derived from the phase field theory [84].

The developed models were implemented into the FLUENT code as user defined functions. Additional functions accounted for the specific boundary and initial conditions in the two geometries, which were used for code validation. An additional scalar field, a smearing of the mass flux through the interfacial region, was defined as well. The scalar field supported the solver to achieve convergence in the mass continuity equation.

The FLUENT code was used to simulate the LAOKOON and the COSMEA facilities. The LAOKOON facility [99] was built to analyze direct contact condensation in a horizontal duct, which featured two-dimensional, steady state flow field. The condensation occurred on the liquid-steam interface, and the water height was constant during the experiment.

A sensitivity study was conducted using the LAOKOON simulations to determine the limitations and possibilities of the four condensation models. Mesh independence study, the effect of the smeared mass flux and the relaxation factor in the numerical iteration technique was investigated in details.

The numerical technique and the surface renewal correlation were mesh independent. The phase field theory was independent for the resolution of the second mesh. The heat flux balance model was mesh dependent, and the better resolution of the interfacial region was not possible with the applied two-equation turbulence model.

The smearing of the mass flux through the interfacial region helped the convergence of the solver. Nonetheless, the effect of the diffusion coefficient, which determines the thickness of the smearing, was negligible for all models.

The optimal relaxation factor in the first model was independent from the mesh and the diffusion coefficient. Low values of the factor resulted in an unphysical subcooling of the gas phase, while high values caused divergence in the simulations, and the steady state condition was not established. The optimal relaxation factor has to be tuned for each experiments individually; therefore, the big computational domain or a transient nature of a process limits the applicability of the method.

The numerical iteration and the phase field models achieved the best agreement with the experimental results. The two calculations followed closely the experimental temperature

distribution along the thermocouple line in the water. The subcooling of the steam was not significant, and was concentrated to the interfacial cells. The phase field model requires a finer mesh than the numerical iteration technique.

The condensation mass transfer for the surface renewal model did not compensate the subcooling of the gas phase. The surface renewal model is not suggested with the VOF model, as it depends on the turbulent conditions at the interface, which is difficult to resolve with VOF.

The direct solution of the heat flux balance equation obtained close results to the experiment, but the subcooling of the gas phase in the interfacial region was observed. The calculation was mesh dependent. Higher resolution of the interfacial region was not possible with the applied turbulence model.

The conclusions were used to set up the simulation for the COSMEA facility. The condensation pipe had a length to diameter ratio close to ninety; therefore, about two million nodes were needed in the calculation domain. The initial conditions were achieved by steady state calculations, and transient simulations were used to establish the conditions in the pipe.

Similarly to the LAOKOON simulations, the smearing function was absolute necessary to achieve convergence, and to avoid the reversed flow at the outlet. The diffusion coefficient was set that the interfacial region occupied 6 cells.

The surface renewal theory did not provide high enough mass transfer rates, as the liquid film was laminar and a significant heat transfer enhancement by surface renewal takes only place if there is turbulence in the liquid phase. The heat flux balance method provided good initial conditions for the transient calculations; however, the transient calculation did not converge for the user defined scalar equation. Therefore, these two models were not able to calculate the COSMEA experiment.

The numerical iteration and the phase field models were numerically stable. The calculation results were compared to the experiment for the total condensation rate, the void fraction distribution and the heat flux measurements.

The phase field model could predict the void fraction distribution and the calculated average heat flux. A flume at the bottom of the pipe developed, which had mainly axial velocity components. The liquid film had an average thickness of 0.1 mm, and it had a local maximum thickness at the top of the pipe. The steam core moved towards the liquid film interface, where it condensed, and the liquid film flowed downwards to the axial flume. The wall heat flux distribution in the cross section reflected the results from the film thickness distribution.

The subcooling of the gas phase was observed in the CFD calculations due to the coarser mesh at the stratified flow surface. The gas cooled 5 K below the saturation value in the phase field model. Therefore, the total condensation rate was under-predicted compared to the experiment.

The numerical iteration failed to predict the condensation phenomenon. The condensation rate in the phase field model was two times higher than the condensation rate in the numerical iteration model. The results suggest that the constant relaxation factor in the transient calculation and for the changing liquid film thickness could not achieve proper global condensation rate in the pipe. Varying the relaxation rate in the transient calculation was not possible due to the long calculation time.

6.3 Comparison of the two approaches and outlook

The comparison was made between the experiment, the RELAP5 calculation and the CFD calculations, which showed that the best practice was adopted to calculate the phenomenon in the condensation pipe for one-dimensional system codes and for CFD codes. Nevertheless, both approaches have advantages and limitations. The RELAP5 code was able to reproduce the experimental data fast and reliably. However, a mechanistic prediction of the void fraction distribution in the pipe cross section was necessary to achieve good results.

The CFD calculations required about 1.5 million cells; therefore, the calculation time was significantly higher. However, it is not necessary to assume the initial distribution of the void fraction, as it is a result of the continuity equations. The CFD calculation provides more details about the flow field and more understanding of the process than the thermal-hydraulic system code. The developed condensation models are general, and, although they have limitations, the proper settings can be found for any engineering application with phase transition. The models have no limitation for the multiphase model, for the turbulent model, and for the solver settings. The only limitation is that they assume that the mass transfer is concentrated to the interface between the liquid and its vapor.

The numerical iteration technique is a powerful tool; however, the selection of the relaxation factor is a limiting factor. To establish such a procedure, series of experiments are needed. The experiments are feasible, if the flow field is steady state and two-dimensional; hence, the number of calculations is not limited by the calculation time. The experiments should account for different flow conditions, *e.g.* pressure or turbulence level, so the sensitivity study can be done for the optimal relaxation factor.

Whenever the flow is three-dimensional, the computational fluid dynamics code, with the implemented phase change models, provide a powerful tool to calculate condensation. The validation of the models should be done for other phase change processes as well, including boiling and transient direct contact condensation.

A Measurement results for the COSMEA facility

The measurement results for the COSMEA experiments [101] are presented, separately for the inlet conditions (Table A.1), the primary side (Table A.2), heat flux data (Table A.3), and secondary side (Table A.4). The following tables indicate if the parameter is for steam (*s*) or water (*w*), primary side (*pr*) or secondary side *sec*. The measurement points are in Table 1.7.

Table A.1: Measurement matrix of the COSMEA experiments

No.	P^{pr} (bar)	ϵ^{pr}	$\dot{m}_{total}(kg/s)$	$\dot{m}_s(kg/s)$	$\dot{m}_w(kg/s)$	$T^{sec}_{mean}(K)$	$\Delta T^{sec}(K)$
51	5	1	0.088	0.088	0	313	3
52	5	0.63	0.130	0.064	0.042	313	3
151	15	1	0.255	0.255	0	313	3
152	15	0.80	0.255	0.204	0.051	313	3
153	15	0.60	0.255	0.153	0.102	313	3
154	15	0.40	0.255	0.102	0.153	313	3
251	25	1	0.406	0.406	0	313	5
252	25	0.83	0.406	0.336	0.07	313	5
253	25	0.66	0.406	0.266	0.14	313	5
254	25	0.48	0.406	0.196	0.21	313	5
255	25	0.31	0.406	0.125	0.281	313	5
451	45	1	0.610	0.610	0	313	5
452	45	0.85	0.610	0.520	0.09	313	5
453	45	0.70	0.610	0.429	0.181	313	5
454	45	0.56	0.610	0.339	0.271	313	5
455	45	0.41	0.610	0.248	0.362	313	5
456	45	0.33	0.610	0.203	0.406	313	5
651	65	1	0.800	0.800	0	315	5
652	65	0.85	0.800	0.678	0.122	315	5
653	65	0.70	0.800	0.556	0.244	315	5
654	65	0.54	0.800	0.434	0.366	315	5
655	65	0.43	0.800	0.340	0.470	315	5
656	65	0.31	0.800	0.245	0.555	315	5

Table A.2: Measurement results - primary side

No. No.	P_{I1} (MPa)	$T_s[P_{I1}]$ (K)	$\dot{m}_s$ (kg/s)	T_s^{in} (K)	$\dot{m}_w$ (kg/s)	T_w^{in} (K)	h_{X1} (mm)	h_{X2} (mm)	h_{X3} (mm)	h_{X4} (mm)	h_{X5} (mm)	P_{out} (MPa)	$\dot{m}_{cond}$ (g/s)	P_{T4-O1} (kW)	v_s (m/s)	v_w (m/s)
51	0.506	425.35	0.087	425.2	-	–	ns	ns	2.5	3.5	4.0	0.500	62	57	21.93	0
52	0.504	425.25	0.064	425.1	0.041	424.7	ns	4.5	4.5	4.0	5.5	0.500	47	50.5	16.91	0.66
151	1.520	472.07	0.256	471.8	-	–	ns	ns	ns	ns	ns	1.500	129	99	22.75	0
152	1.514	471.88	0.206	471.7	0.050	467.4	ns	3.0	4.0	4.0	5.0	1.500	114	92.5	19.18	0.85
153	1.510	471.76	0.152	471.6	0.102	471.0	4.5	4.5	5.0	5.0	5.5	1.500	101	87	14.15	1.75
154	1.512	471.82	0.103	471.6	0.151	471.6	6.0	5.5	6.5	7.0	8.0	1.505	82	79	9.59	2.59
251	2.536	497.86	0.406	497.6	-	–	ns	ns	2.0	ns	ns	2.500	156	107	22.91	0
252	2.531	497.76	0.334	497.5	0.072	493.6	ns	1.5	2.5	4.5	5.0	2.501	148	103.5	18.85	1.28
253	2.523	497.59	0.270	497.4	0.138	496.8	3.0	4.0	5.0	5.0	5.5	2.500	132	98	15.23	2.45
254	2.517	497.46	0.195	497.3	0.209	497.2	5.0	5.0	5.5	6.5	7.0	2.502	112	90	11.00	3.72
255	2.519	497.50	0.124	497.4	0.272	497.8	5.5	6.5	7.5	8.5	9.5	2.508	87	83	6.99	4.84
451	4.545	531.19	0.605	530.9	-	–	ns	1.5	ns	1.5	ns	4.500	230	135.5	17.93	0
452	4.544	531.18	0.523	530.9	0.091	526.1	ns	2.0	2.5	3.5	4.0	4.503	211	130.5	16.24	1.72
453	4.536	531.07	0.428	530.8	0.180	529.6	2.5	3.0	3.5	4.5	5.5	4.505	191	127.5	13.29	3.40
454	4.536	531.07	0.342	530.8	0.266	530.6	2.5	4.0	4.5	5.5	6.5	4.513	175	121.5	10.62	5.02
455	4.546	531.21	0.250	531.0	0.356	531.5	5.5	5.5	6.5	8.0	9.5	4.530	142	112.5	7.76	6.73
456	4.538	531.10	0.202	530.9	0.398	531.7	4.5	6.0	7.0	7.5	9.5	4.523	116	106.5	6.27	7.52
651	6.565	554.67	0.801	554.4	-	–	ns	1.5	ns	2.5	1.5	6.503	292	157	16.06	0
652	6.548	554.49	0.684	554.3	0.117	549.9	1.5	2.0	3.0	4.0	4.0	6.494	268	153.5	14.37	2.32
653	6.544	554.45	0.568	554.2	0.238	552.7	2.5	3.5	4.0	4.5	5.0	6.504	249	151	11.93	4.73
654	6.516	554.17	0.434	554.0	0.360	553.8	3.5	3.5	5.0	6.5	7.5	6.484	226	145	9.11	7.15
655	6.535	554.36	0.343	554.1	0.462	554.5	5.0	5.0	6.5	7.5	9.5	6.508	185	137.5	7.20	9.18
656	6.574	554.76	0.247	554.5	0.559	555.1	6.0	8.0	10.0	12.0	13.5	6.549	130	126.5	5.18	11.11

Table A.3: Measurement results - heat flux data (Position T4)

No.	T^{in}_{180}	T^{in}_{135}	T^{in}_{90}	T^{in}_{45}	T^{in}_{0}	T^{out}_{180}	T^{out}_{135}	T^{out}_{90}	T^{out}_{45}	T^{out}_{0}	q_{180}	q_{135}	q_{90}	q_{45}	q_{0}
					(K)								(kW/m^2)		
51	416.25	415.45	414.55	405.95	395.35	333.75	337.95	338.05	330.05	329.65	437.4	428.3	406.3	424.4	365.9
52	416.15	412.25	413.85	396.05	387.85	334.55	337.75	338.85	328.75	327.85	432.8	410.5	398.2	374	332.4
151	466.75	458.55	462.15	455.75	451.95	334.65	337.85	338.85	332.05	334.25	716.1	679.5	669	708.3	672.9
152	463.65	455.45	458.65	450.45	441.45	334.45	337.75	338.55	331.85	333.05	699.4	661.9	650.3	677.4	616.7
153	460.35	452.25	454.45	442.75	432.55	334.15	337.15	338.15	331.05	331.75	682.1	645.7	628.5	635.2	570.6
154	455.85	449.65	452.45	418.85	420.65	335.15	338.25	339.75	328.25	330.05	651.6	625	609	509.4	509.9
251	494.85	487.15	490.75	485.25	483.45	347.15	352.35	353.25	343.95	347.45	814.7	772.4	759	822.6	792.9
252	493.45	484.55	488.45	482.15	475.05	346.55	351.45	352.35	343.25	345.45	809.8	761.7	750.3	807.5	752.3
253	490.85	481.95	485.55	477.65	467.85	346.55	351.65	352.45	343.35	344.55	794.2	745	732.9	779.4	712.9
254	486.25	477.45	479.45	465.15	462.35	345.85	350.95	350.95	342.05	343.55	771.1	721.6	705.2	710.3	685.1
255	480.85	475.15	477.35	447.95	451.45	345.95	352.15	352.95	339.35	341.95	739.6	701.8	683.1	621	628
451	528.15	519.95	524.35	517.85	517.55	348.55	353.65	355.05	344.15	348.95	1004.5	965.6	947.9	1024.8	996.3
452	527.15	517.95	522.65	515.55	511.25	348.25	353.55	354.65	343.85	347.85	999.7	954.5	939.6	1011.7	963.2
453	525.65	515.05	519.75	511.15	505.05	348.05	353.55	354.35	343.75	346.65	991.9	936	924.2	984.8	930.6
454	523.05	511.45	515.75	503.45	501.15	347.65	353.15	353.75	343.05	346.45	978.3	916.6	903.5	940.4	907.9
455	517.65	505.85	509.15	489.45	491.15	346.75	352.05	352.55	341.85	345.25	950.7	887.8	870.6	860.4	852.2
456	512.55	502.05	504.45	482.85	485.35	345.45	351.55	352.25	341.45	345.35	927.7	867.4	844.3	821.4	816.1
651	552.25	544.05	548.65	540.95	540.85	349.85	355.55	356.65	344.75	350.55	1142.6	1105.9	1085.4	1168.4	1135.9
652	550.75	541.95	546.95	538.35	533.65	349.55	355.15	355.85	344.15	349.35	1135.3	1094.6	1079.1	1155.3	1096.4
653	549.05	538.85	544.15	533.85	528.65	350.05	355.35	356.15	344.65	349.25	1122.3	1074	1060.6	1123.9	1065.1
654	546.55	533.45	538.45	526.35	525.05	349.15	354.45	355.05	344.05	348.75	1112.1	1045.7	1032.7	1079.1	1044.6
655	542.85	528.85	533.05	515.75	515.75	348.55	353.95	354.25	343.15	347.45	1092.7	1019.5	1004.3	1017.2	993.3
656	537.45	522.65	525.15	501.75	502.75	347.55	352.75	352.85	341.95	345.95	1065.5	987.6	964	936.2	920.5

Table A.4: Measurement results - Secondary side

No.	$P_{I2}(MPa)$	$\dot{m}_{I2}(kg/s)$	$T_{I2}(K)$	$T_4(K)$	$T_3(K)$	$T_2(K)$	$T_1(K)$	$T_{O2}(K)$
51	0.3	15.7	311.65	312.55	313.25	313.45	313.35	313.85
52	0.3	14.3	311.65	312.55	313.15	313.45	313.35	313.85
151	0.5	29.6	311.85	312.65	313.35	313.65	313.45	314.05
152	0.5	27.5	311.65	312.45	313.15	313.45	313.35	313.85
153	0.4	25.7	311.65	312.45	313.05	313.45	313.25	313.85
154	0.4	23.4	311.75	312.45	313.15	313.45	313.35	313.95
251	0.4	19.1	310.65	311.95	312.95	313.45	313.25	314.45
252	0.4	18.8	310.75	311.95	312.95	313.45	313.25	314.35
253	0.4	17.5	310.65	311.95	312.95	313.35	313.15	314.45
254	0.3	16.1	310.65	311.85	312.85	313.35	313.15	314.45
255	0.3	14.9	310.65	311.75	312.75	313.25	313.15	314.45
451	0.4	25.3	311.55	312.85	313.85	314.35	314.15	315.15
452	0.4	23.9	310.55	311.85	312.85	313.35	313.15	314.15
453	0.4	23.1	310.65	311.95	312.95	313.45	313.25	314.25
454	0.4	22.0	310.65	311.95	312.95	313.45	313.25	314.35
455	0.4	20.3	310.25	311.55	312.45	313.05	312.85	313.95
456	0.4	19.1	310.55	311.85	312.75	313.25	313.15	314.25
651	0.5	29.6	312.65	313.95	315.05	315.35	315.15	316.35
652	0.5	28.5	312.05	313.35	314.45	314.85	314.65	315.75
653	0.4	27.9	313.15	314.55	315.55	315.95	315.75	316.85
654	0.4	26.7	312.95	314.25	315.35	315.65	315.45	316.65
655	0.4	25.4	312.75	314.05	315.15	315.45	315.25	316.45
656	0.4	23.3	312.65	313.85	314.95	315.25	315.15	316.35

Bibliography

[1] Z. V. Stosic, W. Brettschuh, and U. Stoll. Boiling water reactor with innovative safety concept: The Generation III+ SWR-1000. *Nuclear Engineering and Design*, 238:1863–1901, 2008.

[2] A. M. Goldberg and R. Rosner. *Nuclear Reactors: Generation to Generation*. American Academy of Arts and Sciences, 2011. ISBN:978-0-9842760-0-4.

[3] T. J. Katona and S. Ratkai. Extension of operational life-time of WWER-440/213 type units at Paks nuclear power plant . *Nuclear Engineering and Design*, 40:269–276, 2008.

[4] IAEA. Final Report on U. C. Berkeley Single Tube Condensation Studies. Technical Report UCB-NE-4201, Helmholtz-Zentrum Dresden Rossendorf, August 1994.

[5] J. Kelly, T. Dujardin, and H. Paillére. GIF's role in developing the nuclear technologies of the future. Technical Report No. 31.2, NEA updates, NEA News, 2013.

[6] R Aymar, P Barabaschi, and Y Shimomura. The ITER design. *Plasma Physics and Controlled Fusion*, 44:519–565, 2002.

[7] S. Leyer and M. Wich. The Integral Test Facility Karlstein. *Science and Technology of Nuclear Installations*, 2012:1–12, 2012.

[8] A. Manera, H-M. Prasser, and S. Leyer. Analysis of the Performance of the KERENA Emergency Condenser. In *NURETH-14*, Toronto, Canada, September 2011. paper 471.

[9] H.-M. Praser. Integral pre-test Calculations of INKA Experiments, Comparison of Scenarios, Summary and Proposal of Test Specifications. Technical Report TM-42-13-14, Paul Scherrer Intitute, 2013.

[10] U.S. NRC. *RELAP5/mod3.3 Code Manual Vol. IV.: Models and Correlations*, 2001. NUREG/CR-5535/Rev-1.

[11] U. S. NRC. *TRACE V5.0p2: Theory Manual*, 2010.

[12] D. Bestion. The physical closure laws in the CATHARE code. *Nuclear Engineering and Design*, 124:229–245, 1990.

[13] *ATHLET Mod 3.0 Cycle A*, 2012.

[14] M. Hänninen and E. Ahtinen. Simulation of non-condensable gas flow in two-fluid model of APROS – Description of the model, validation and application. *Annals of Nuclear Energy*, 36:1588—-1596, 2009.

[15] U.S. NRC. *RELAP5/mod3.3 Code Manual Vol. I.: CODE STRUCTURE, SYSTEM MODELS, AND SOLUTION METHODS*, 2001. NUREG/CR-5535/Rev-1.

[16] J. G. Collier. *Convective boiling and condensation.* New York,, 1972.

[17] U.S. NRC. *RELAP5/mod3.3 Code Manual Vol. VIII.: Programmers Manual,* 2001. NUREG/CR-5535/Rev-1.

[18] G. Yadigaroglu. Computational Fluid Dynamics for nuclear applications: from CFD to multi-scale CMFD. *Nuclear Engineering and Design*, 235:153–164, 2005.

[19] F. H. Harlow and A. A. Amsden. Flow of interpenetrating material phases . *Journal of Computational Physics*, 18:440–464, 1975.

[20] F. W. Dittus and L. M. K. Boelter. Heat Transfer in Automobile Radiators of the Tubular Type. *Publications in Engineering*, 2:433–461, 1930.

[21] J. C. Chato. Laminar condensation inside horizontal tube. *ASHARE trans*, 4:52–60, 1962.

[22] M. M. Shah. An improved and extended general correlation for heat transfer during condensation in plain tubes. *HVAC and R Research*, 15:889–913, 2009.

[23] W. Nusselt. Die Oberflachenkondensation des Wasserdapfes. *Zeitschrift des Vereines Deutscher Ingenieure*, 60:541–575, 1916.

[24] A. P. Colburn and O. A. Hougen. Design of Cooler Condensers for Mixtures of Vapors with Noncondensing Gases. *Industrial and Engineering Chemistry*, 26:1178–1182, 1934.

[25] Y. A. Hassan and S. Banerjee. Implementation of a non-condensable model in RELAP5/mod3. *Nuclear Engineering and Design*, 162:281–300, 1996.

[26] S. Z. Kuhn, V. E. Schrock, and P. F. Peterson. Status and Trends of Nuclear Technologies. Technical Report IAEA-TECDOC-1622; ISBN 978–92–0–108709–6, International Atomic Energy Agency, September 2009.

[27] J. R. Sellars, M. Tribus, and J. S. Klein. Heat Transfer to Laminar Flows in a Round Tube or Flat Conduit: The Graetz Problem Extended. *Transactions, American Society of Mechanical Engineers*, 78:441, 1956.

[28] V. Gnielinski. New Equations Flow Regime Heat and Mass Transfer in Turbulent Pipe and Channel Flow. *Int. Chem. Eng.*, 16:359–368, 1976.

[29] S. Z. Kuhn, V. E. Schrock, and P. F Peterson. Final report on U. C. Berkley single tube condensation studies. Technical report, UCB-NE-4201, 1994.

[30] M. M. Shah. Heat transfer during film condensation in tubes and annuli: the review of the literature. *ASHARE trans*, 87:1086–1105, 1981.

[31] A.S. Dalkilic and S. Wongwises. Intensive literature review of condensation inside smooth and enhanced tubes. *International Journal of Heat and Mass Transfer*, 52:3409–3426, 2009.

[32] S. Lips and J.P. Meyer. Two-phase flow in inclined tubes with specific reference to condensation: a review. *Internal Journal of Multiphase Flow*, 37:845–859, 2011.

[33] A. Cavallini, G. Censi, D. Del Col, L. Doretti, G. A. Longo, L. Rossetto, and C. Zilio. Condensation inside and outside smooth and enhanced tubes: a review of recent research. *International Journal of Refrigeration*, 26:373–392, 2003.

[34] A. Schaffrath, E. F. Hicken, H. Jaegers, and H.-M. Prasser. Operation Conditions of the Emergency Condenser of the SWR1000. *Nuclear Engineering and Design*, 188:303–318, 1999.

[35] W. Li, E. F. Hicken, P. David, H.-M. Prasser, D. Baldauf, and J. Zschau. Messung der Kondensatfilmdicken in einem dampfstroemten horizontalen Rohr. *Jahrestagung Kerntechnik, Dresden, 15/17 Mai 2001, Tagungsbericht*, pages 103–106, 2001.

[36] H.M. Soliman. In the annular-to-wavy flow pattern transition during condensation inside horizontal tubes. *The Canadian Journal of Chemical Engineering*, 60:475–481, 1983.

[37] A. Schaffrath, A.K. Kruessenberg, A. Fjodorow, U. Gocht, and W. Lischke. Modeling condensation in horizontal tubes. *Nuclear Engineering and Design*, 204:251–265, 2001.

[38] M. S. Chitti and N. K. Anand. An analytical model for local heat transfer coefficients for forced convective condensation inside smooth horizontal tubes. *International Journal of Heat and Mass Transfer*, 38:615–627, 1995.

[39] J. T. Kwon, Y.C. Ahn, and M.H. Kim. A modeling of in-tube condensation heat transfer for a turbulent annular film flow with liquid entrainment. *Internal Journal of Multiphase Flow*, 27:911–928, 2001.

[40] J. C. Chato. *Laminar condensation inside horizontal and inclined tubes.* PhD thesis, MIT USA, 1960.

[41] M.K. Dobson and J.C. Chato. Condensation in Smooth Horizontal Tubes. *Journal of Heat Transfer - ASME*, 120:193–213, 1998.

[42] G.W. Breber, J.W. Palen, and J. Taborek. Prediction of horizontal tubeside condensation of pure components. *Transactions, American Society of Mechanical Engineers*, 102:471–476, 1980.

[43] H. Jaster and P.G. Kosky. Condensation heat transfer in a mixed flow regime. *International Journal of Heat and Mass Transfer*, 19:95–99, 1976.

[44] C.E. Rufer and S.P. Kezios. Analysis of two-phase, onecomponent stratified flow with condensation. *ASHARE trans*, 88:265, 1966.

[45] K.Y. Choi, H.J. Chung, and H.C. No. Direct-contact condensation heat transfer model in RELAP5/mod3.2 with/without noncondensable gases for horizontally stratified flow. *Nuclear Engineering and Design*, 211:139–151, 2002.

[46] K. Y. Choi, H. S. Park, S. J. Kim, H. C. No, and Y. S. Bang. Assessment and improvement of condensation models in RELAP5/mod3.2. *Nuclear Technology*, 124:103–117, 1998.

[47] E. Krepper, A. Schaffrath, and A. Aszodi. Numerical simulation of the emergency condenser of the SWR1000. *Kerntechnik*, 64:243–252, 1999.

[48] J. El Hajal, J. R. Thome, and A. Cavallini. Condensation in horizontal tubes, part 1: two-phase flow pattern map. *International Journal of Heat and Mass Transfer*, 46:3349–3363, 2003.

[49] J. R. Thome, J. El Hajal, and A. Cavallini. Condensation in horizontal tubes, part 2: new heat transfer model based on flow regimes. *International Journal of Heat and Mass Transfer*, 46:3365–3387, 2011.

[50] P. K. Sarma, C. V. N. Sastry, V. D. Rao, S. Kakac, and H. Liu. Convective condensation heat transfer in a horizontal condenser tube. *International Journal of Thermal Science*, 41:295–301, 2001.

[51] V. Stevanovic and M. Studovic. A simple model for vertical annular and horizontal stratified two-phase flows with liquid entrainment and phase transition: one-dimensional steady state conditions. *Nuclear Engineering and Design*, 154:357–379, 1995.

[52] S. Lips and J.P. Meyer. Stratified flow model for convective condensation in an inclined tube. *International Journal of Heat and Mass Transfer*, 36:83–91, 2012.

[53] G. P. Fieg and W. Roetzel. Calculation of laminar film condensation in/on inclined elliptical tubes. *International Journal of Heat and Mass Transfer*, 37:619–624, 1994.

[54] ANSYS, Inc. *ANSYS FLUENT 14.5: Theory Guide*, 2012.

[55] ANSYS, Inc. *ANSYS FLUENT 14.5: User's Guide*, 2012.

[56] D. C. Wilcox. Re-assessment of the scale-determining equation for advanced turbulence models. *AIAA Journal*, 26:1299–1310, 1988.

[57] C. W. Hirt and B. D. Nichols. Volume of Fluid (VOF) method for the dynamics of free boundaries. *Journal of Computational Physics*, 39:201–225, 1981.

[58] Y. Bartosiewicz, J.-M. Seynhaeve, C. Vallée, T. Höhne, and J.-M. Laviéville. Modeling free surface flows relevant to a PTS scenario: Comparison between experimental data and three RANS based CFD codes. Comments on the CFD-experiment integration and best practice guidline. *Nuclear Engineering and Design*, 240:2375–2381, 2010.

[59] H. Lan, M. Friedrich, B. F. Armaly, and J. A. Drallmeier. Simulation and Measurement of 3D Shear-driven Thin Liquid Film Flow in a Duct. *International Journal of Heat and Fluid Flow*, 29:449–459, 2008.

[60] A. Alizadehdakhel, M. Rahimi, J. Sanjari, and A. A. Alsairafi. CFD and Artificial Neural Network Modeling of Two-phase Flow Pressure Drop. *International Communications in Heat and Mass Transfer*, 36:850–856, 2009.

[61] A. A. Mouza, S. V. Paras, and A. J. Karabelas. CFD Code Application to wavy stratified gas-liquid flow. *Trans IChemE*, 79:561–568, 2001.

[62] W. Wróblewski, S. Dykas, and A. Gepert. Steam Condensing Flow Modeling in Turbine Channels. *Internal Journal of Multiphase Flow*, 35:498–506, 2009.

[63] S. Dykas and W. Wróblewski. Single- and Two-fluid Models for Steam Condensing Flow Modeling. *Internal Journal of Multiphase Flow*, 37:1245–1253, 2011.

[64] A. Dehbi, F. Janasz, and B. Bell. Prediction of Steam Condensation in the Presence of Noncondensable Gases Using a CFD-based Approach. *Nuclear Engineering and Design*, 258:199–210, 2013.

[65] A. Dehbi. On the Adequacy of Wall Functions to Predict Condensation Rates from Steam-Noncondensable Gas Mixtures. *Nuclear Engineering and Design*, 265:25–34, 2013.

[66] L. Štrubelj, Gy. Ézsöl, and I. Tiselj. Direct Contact Condensation Induced Transition from Stratified to Slug Flow. *Nuclear Engineering and Design*, 240:266–274, 2010.

[67] E. D. Hughes and R. B. Duffey. Direct Contact Condensation and Momentum Transfer in Turbulent Separated Flows. *Internal Journal of Multiphase Flow*, 17:599–619, 1991.

[68] S. Banerjee. A Surface Renewal Model for Interfacial Heat and Mass Transfer in Transient Two-phase Flow. *Internal Journal of Multiphase Flow*, 4:571–573, 1978.

[69] Y. Egorov. Validation of CFD codes woth PTS relevant test cases. Technical Report EVOL-ECORA-D07, Ansys, Germany, 2004.

[70] D. Lucas. Review of the existing data basis for the validation of models for PTS. Technical Report NURESIM-SP2-TY; D2.1.2, FZR, 2005.

[71] M. Scheuerer. Numerical Simulation of The LAOKOON Test Cases - Free Surface Flow with Heat and Mass Transfer. Technical Report NURESIM-SP2-TH, D.2.1.4.1, GRS, Germany, 2006.

[72] S. C. Ceuca and Macián-Juan R. CFD Simulation of Direct contact Condensation with ANSYS CFX using Locally defined Heat Transfer Coefficient. In *ICONE-20*, Anaheim, California, USA, August 2012. No. 54347.

[73] D. Lakehal, M. Fulgosi, and G. Yadigaroglu. Direct Numerical Simulation of Condensing Stratified Flow. *Journal of Heat Transfer - ASME*, 130:021501–02150110, 2008.

[74] S. Sussman, P. Smereka, and S. Osher. A level set approach for computing incompressible two-phase flow. *Journal of Computational Physics*, 114:146–161, 1994.

[75] D. Lakehal and M. Labois. A New Modeling Strategy for Phase-change Heat transfer in Turbulent Interfacial Two-phase Flows. *Internal Journal of Multiphase Flow*, 37:627–639, 2011.

[76] Y. Zhaohui, Z. Xiwen, and W. Xuefang. Numerical Simulation of Condensation-induced Water-hammer. *Tsinghua Science and Technology*, 2:599–602, 1997.

[77] Z. Liu, B. Sunden, and J. Yuan. VOF Modeling and Analysis of Filmwise Condensation Between Vertical Parallel Plates. *Heat Transfer Research*, 43:47–68, 2012.

[78] W. H. Lee. A Pressure Iteration Scheme for Two-Phase Flow Modeling. *In: Multiphase Transport: Fundamentals, Reactor Safety, Applications*, pages 407–432, 1980.

[79] S. W. J. Welch and J. Wilson. A Volume of Fluid Based Method for Fluid Flows with Phase Change. *Journal of Computational Physics*, 160:662–682, 2000.

[80] Y. Sato and B. Ničeno. A sharp-interface phase change model for a mass-conservative interface tracking method. *Journal of COmputational Physics*, 249:127–161, 2013.

[81] B. A. Nichita. *AN Improved CFD tool to Simulate Adiabatic and Diabatic Two Phase Flows*. PhD thesis, EPFL, Switzerland, 2010.

[82] H. Ganapathy, A. Shooshtari, K. Choo, S. Dessiatoun, M. Alshehhi, and M. Ohadi. Volume of Fluid-based Numerical Modeling of Condensation Heat Transfer and Fluid Flow Characteristics in Microchannels. *International Journal of Heat and Mass Transfer*, 65:62–72, 2013.

[83] D.-L. Sun, J.-L. Xu, and L. Wang. Development of a Vapor-Liquid Phase Change Model for Volume-of-Fluid Method in FLUENT. *International Communications in Heat and Mass Transfer*, 39:1101–1106, 2012.

[84] Arnoldo Badillo. Quantitative phase-field modeling for boiling phenomena. *Physical Review E*, 86:041603, Oct 2012.

[85] A. Badillo. Phase Field simulations of bubble growth under convective conditions. In *Proceedings of ASME 2013 International Mechanical Engineering Congress and Exposition*, San Diego, USA, November 2013. IMECE2013-65925.

[86] V. Tanskanen, A. Jordan, M. Puustinen, and R. Kyrki-Rajamaki. CFD simulation and pattern recognition analysis of the chugging condensation regime. *Annals of Nuclear Energy*, 66:133–143, 2014.

[87] C. Kunkelmann and P. Stephan. CFD Simulation of Boiling Flows Using the Volume-of-Fluid Method within OpenFOAM. *Numerical Heat Transfer*, 56:631–646, 2009.

[88] S. Hardt and F. Wondra. Evaporation model for interfacial flows based on a continuum-field representation of the source terms. *Journal of Computational Physics*, 227:5871–5895, 2008.

[89] Mirco Magnini. *CFD Modeling of Two-Phase Boiling Flows in the Slug Flow Regime with an Interface Capturing Technique*. PhD thesis, University of Bologna, Italy, 2012.

[90] E. Da Riva and D. Del Col. Numerical Simulation of Laminar Liquid Film Condensation in a Horizontal Circular Minichannel. *Journal of Heat Transfer - ASME*, 134:051019, 2012.

[91] S. C. K. De Schepper, Heynderickx G. J., and G. B. Marin. Modeling the evaporation of a hydrocarbon feedstock in the convection section of a steam cracker. *Computers and Chemical Engineering*, 33:122–132, 2009.

[92] A. Alizadehdakhel, M. Rahimi, and A. A. Alsairafi. CFD modeling of flow and heat transfer in a thermosyphon. *International Communications in Heat and Mass Transfer*, 37:312–318, 2010.

[93] C. Aghanajafi and K. Hesampour. Heat Transfer Analysis of a Condensate Flow by VOF Method. *Journal of Fusion Energy*, 25:219–223, 2006.

[94] C. Kunkelmann. *Numerical Modeling and Investigation of Boiling Phenomena*. PhD thesis, Technical University Darmstadt, Germany, 2011.

[95] S. Herbert, S. Fischer, T. Gambaryan-Roisman, and P. Stephan. Local heat transfer and phase change phenomena during single drop impingement on a hot surface. *International Journal of Heat and Mass Transfer*, 61:605–614, 2013.

[96] A. Böttger, T. Gocht, H-M. Prasser, and J. Zschau. Transiente Kondensationversuche an einem Notkondensator / Einzelrohr (INVEP) . Technical Report ISSN 1437-322X, Forschungzentrum Rossendorf, 2003.

[97] A. R. Edwards and T. P. O'Brien. Studies of Phenomena connected with Depressurization of Water Reactors. *Journal of the British Nuclear Energy Society*, 9:125–135, 1970.

[98] H.-M. Prasser, A. Böttger, J. Zschau, and T. Gocht. Needle shaped conductivity probes with integrated micro-thermocouple and their application in rapid condensation experiments with non-condensable gases. *Kerntechnik*, 3:114–120, 2003.

[99] M. Goldbrunner, J. Karl, and D. Hein. Experimental Investigation of Heat Transfer Phenomena During Direct Contact Condensation in the Presence of Noncondensable gas by means of Linear Raman Spectroscopy. In *10th Int. Symp. on Laser Techniques Applied to Fluid Mechanics*, Lisbon, July 2000.

[100] P. Griffith. Screening reactor steam/water piping systems for water hammer. Technical Report NUREG/CR-6519, U.S. Nuclear Regulatory Commission, 1996.

[101] T. Geißler, M. Beyer, U. Hampel, C. Vallée, and H. Pietruske. Single effect studies of steam condensation and heat transfer in a declined pipe. Technical Report Final Report, Helmholtz-Zentrum Dresden Rossendorf, 2012.

[102] http://eng-calculations.com/Saturated Steam.aspx/Saturated Steam.aspx.

[103] D. Biberg. An explicit approximation for the wetted angle in two-phase stratified pipe flow. *The Canadian Journal of Chemical Engineering*, 77:1221–1224, 1999.

[104] Van P. Carey. *Liquid–Vapor Phase–Change Phenomena, 2nd. ed.* Taylor and Francis Group, LLC, New York, USA, 2008. ISBN-987-1-59169-035-1.

[105] A. Faghri, Y. Zhang, and J. Howell. *Advanced Heat and Mass Transfer.* Global DIgital Press, 2010. ISBN:0-87724-090-6.

[106] J. R. Thome. *Heat Transfer Engineering Databook III.* Wolverine Tube, 2010.

[107] P. Lambert. *Surface Tension in Microsystems.* Springer-Verlag, Berlin, 2013. ISBN:978-3-642-37552-1.

[108] P.-G. de Gennes, F. Brochard-Wyart, and D Quéré. *Capillary and Wetting Phenomena—Drops, Bubbles, Pearls, Waves.* Springer, 2004. ISBN 978-0-387-21656-0.

[109] J. W. Cahn and J. E. Hilliard. Free energy of a nonuniform system. III.Nucleation in a two-component incompressible fluid. *Journal of Chemical Physics*, 31:688–699, 1959.

[110] D. K. Walters and N. M. Wolgemuth. A new interface-capturing discretization scheme for numerical solution of the volume fraction equation in two-phase flows. *International Journal for Numerical Methods in Fluids*, 60:893—-918, 2009.

[111] ANSYS, Inc. *ANSYS FLUENT 14.5: UDF Manual*, 2012.

[112] *Flow of fluids through valves, fittings, and pipe; CRANE valves*, 1999. Technical paper No. 410m.

[113] D. L. Youngs. Time-dependent multi-material flow with large fluid distortion. *Numerical Methods for Fluid Dynamics*, Academic Press:273–285, 1981.

Rita Szijártó

born 21.10.1987 · Hungarian · szijarto.ri@gmail.com

Education

09.2011 - 02.2015	**Swiss Federal Institute of Technology Zurich (ETH)**, Switzerland *PhD Student in Mechanical Engineering*
09.2009 - 06.2011	**Budapest University of Technology and Economics**, Hungary *MSc in Physics.* Qualification: excellent with highest honors.
10.2009 - 02.2010	**Vienna University of Technology**, Austria *Scholarship in Technical Physics.*
09.2006 - 06.2009	**Budapest University of Technology and Economics**, Hungary *BSc in Physics.* Qualification: excellent.

Academic Experience

09.2011 - 02.2015	**Paul Scherrer Institute (PSI)**, Villigen, Switzerland *Scientist (PhD Student)*
02.2009 - 08.2011	**Budapest University of Technology and Economics**, Hungary *Teaching assistant*
07.2010 - 10.2010	**Paul Scherrer Institute**, Villigen, Switzerland *Internship*

Awards

2012 and 2014	**1^{st} award on the PSI NES PhD day** Paul Scherrer Institute, Nuclear Safety Department, Villigen *Conference of the PhD students of the Nuclear Safety Department*

Language and IT skills

Hungarian:	Native language
English:	Fluent writing, reading and communication skills
German:	Satisfactory writing, good reading and communication skills
Operation systems:	Windows, Linux
Applications:	Windows Office (Word, Excel, PowerPoint), LaTeX, Origin Pro, Igraph
Programming languages:	MATLAB, C, C++, Python, R
Fluid dynamics software:	ANSYS Fluent, CFX, ICEM CFD, RELAP5, SNAP

Conference papers

R. Szijártó, B. Yamaji, A. Aszódi: *Study of Natural Convection Around a Vertical Heated Rod Using PIV/LIF Technique* CFD4NRS-3, OECD/IAEA Workshop, 14-16 Sept 2010, Washington D.C., USA

B. Yamaji, R. Szijártó, A. Aszódi: *Study of Thermal Stratification and Mixing Using PIV*, CFD4NRS-3, OECD/IAEA Workshop, 14-16 Sept 2010, Washington D.C., USA

R. Szijártó, B. Yamaji, A. Aszódi: *PIV/LIF Measurement of the Natural Circulation Around a Vertical Heated Rod* The 8th International Topical Meeting on Nuclear Thermal-Hydraulics, Operation and Safety (NUTHOS-8), 10-14 Oct 2010, Shanghai, China

R. Szijártó, B. Yamaji, A. Aszódi: *New Studies of Natural Convection Around a Fuel Rod of the BME Training Reactor with PIV/LIF Technique* 21st Symposium of AER on VVER Reactor Physics and Reactor Safety, 19-22 Sept 2011, Dresden, Germany

R. Kapulla, P. Hoang, R. Szijártó J. Fokken: *Parameter Sensitivity of Optical Flow Applied to PIV Images* Lasermethoden in der Stroemungsmesstechnik, 6- 8 Sept 2011, Ilmenau, Germany

R. Szijártó, J. Freixa, H.-M. Prasser, *Performance of Heat Transfer Models of Thermal-Hydraulic System Codes on the Invert Edwards Pipe Experiment* NUTHOS-9, Kaochiung, Taiwan, September 9-13, 2012

R. Szijártó, J. Freixa, H.-M. Prasser, *Implementation and Validation of a condensation heat transfer model for slightly inclined horizontal pipes for RELAP5* NURETH-15, Pisa, Italy, May 12-15, 2013

Publications

R. Szijártó, J. Freixa, H.-M. Prasser, Simulation of condensation in a closed, slightly inclined horizontal pipe with a modified RELAP5 code, *Nuclear Engineering and Design* 273 (2014) 288–297

Dissertations

R. Szijártó, *Study of thermal stratification with PIV/LIF technique*, BSc dissertation, Budapest University of Technology and Economics, 2009 (Hungarian)

R. Szijártó, *Study of the natural convection around a model of the fuel rod of the BME training reactor with PIV/LIF*, MSc dissertation, Budapest University of Technology and Economics, 2011 (Hungarian)

R. Szijártó, *Study of natural convection around a vertical heated rod using PIV/LIF technique*, Dissertation for the Scientific Student Conference of the Budapest University of Technology and Economics, 2009 (Hungarian)

R. Szijártó, *Development and Application of New Optical Flow Technique for Evaluation of Particle Image Velocimetry (PIV) Images*, Dissertation for the Scientific Student Conference of the Budapest University of Technology and Economics, 2010 (English)

R. Szijártó, *Condensation of steam in horizontal pipes - model development and validation*, PhD Thesis, ETHZ, 2015 (English)